ADVANCEMENTS IN COMPOSITE SOLID PROPELLANT TESTING AND EVALUATION FOR FORMULATIONS CONTAINING NOVEL NANO-ADDITIVES

A Dissertation

by

ANDREW ROBERT DEMKO

Submitted to the Office of Graduate and Professional Studies of
Texas A&M University
in partial fulfillment of the requirements for the degree of

DOCTOR OF PHILOSOPHY

Chair of Committee,	Eric L. Petersen
Committee Members,	Timothy Jacobs
	David Staack
	Chad Mashuga
Head of Department,	Andreas Polycarpou

May 2017

Major Subject: Mechanical Engineering

ABSTRACT

Composite solid propellants are typically used in rocket propulsion systems due to their simplicity and relatively low cost. They are mixtures of the fuel, oxidizer, and various catalysts. Oftentimes, bonding agents and plasticizers are added to improve the mixture and propellant qualities. The advent of the nano-particle synthesis revolution allows for customized particle synthesis. This dissertation outlines two innovative experiments developed at Texas A&M University to study the combustion efficiency and the ignition properties of composite propellants with and without advanced nano-additives.

This study first presents new insight and possible advantages unique only to closed-bomb strand burners for the testing of composite solid propellants. However, little information on the combustion efficiency has been reported with strand burner testing. The advantages of a closed-bomb burner is revealed in the present work for the first time by relating the observed pressure rise to a quantitative measure of combustion efficiency through the use of temperature change approximations. The pressure rise is an indication of the flame temperature from the propellant combustion products that mix with the inert gas (argon) in the chamber. Baseline propellants of diverse ammonium perchlorate (AP) particle size distributions were tested at 80% AP and 20% HTPB by weight. Then, using the highest-performing AP, propellants of 85% mono- and bi-modal AP distributions were tested, resulting in a clear comparison of their relative effects on the propellant burning efficiency. The pressure rise study concluded with comparing combustion efficiencies of the synthesis methods of metal oxide catalysts in both

aluminized and non-aluminized AP and hydroxyl–terminated polybutadiene (HTPB) propellants. Plotting a normalized pressure rise compared and the mean test pressure indicated that the propellants with narrow AP particle size distributions burn more efficiently. Using simplified models, changes in flame temperature were calculated, and corresponding changes in the relative combustion efficiency were found. Chemical c* efficiency changes were approximated using the constant-volume strand burner for different AP particle sizes and titania synthesis methods.

The second focus is on developing a method to evaluate the ignition delay times of similar propellant formulations. Ignition delay time measurements on solid energetic materials lead to better fundamental understanding of the ignition process and provide benchmark data for improving models of the ignition process. This study focused on the validation of ignition delay times of AP/HTPB-based solid propellants with and without aluminum and compared various metal-oxide nanoparticle catalysts. A CO_2 laser with a wavelength of 10.6 μm was operated to obtain a quantifiable and reliable ignition event over a power range of 30 to 100 W. This study developed a method to measure the ignition delay time for AP/HTPB propellants at elevated pressures. The ignition delay time results were compared to literature values for similar conditions. Additional studies to examine the effects of *in-situ* titania nanoparticles on the ignition delay times demonstrated that the nano-additives only appeared to alter the ignition behavior of the aluminized APCP. From the results of these ignition experiments, it can be concluded that additives, which aid in the low-temperature decomposition of AP, such as Fe_2O_3, are believed to impact the ignition delay times the most.

ACKNOWLEDGMENTS

I would like to thank my research advisor and thesis committee chair, Dr. Eric Petersen for his time, guidance, dedication, and patience in my development as an engineer and scientific researcher. His dedication to both his research and his students serves as a model that I desire to emulate. The opportunity to work in his lab for the past six years has been a very educational and rewarding experience that I would do all over again. I would also like to offer my thanks to Dr. Timothy Jacobs, Dr. David Staack and Dr. Chad Mashuga for serving on my dissertation committee and providing valuable insight on my research.

I would like to thank my fellow researchers and friends at the Texas A&M Turbomachinery Laboratory: Thomas Sammet, Catherine Dillier, Jacob Stahl, Chris Thomas and Gordon Morrow. The materials science expertise of Dr. David Reid of Helicon Chemical Co. and Dr. Sudipta Seal of the Advanced Materials Processing and Analysis Center (AMPAC) at the University of Central Florida was critical for the initiation of this work.

Additionally, I would like to thank my family, particularly my parents Jonathan and Carol Demko, for their continued support and for instilling values of hard work and the desire to push myself further; also, my brothers Jonathan and Zachary Demko for always pushing me to be better at anything I do in life; and, lastly my grandmother Blythe for allowing me to stay with her as I finished my research. I would not be where I am today without my family.

CONTRIBUTORS AND FUNDING SOURCES

Contributors

This work was supervised by a thesis committee consisting of Professors Eric L. Petersen, Timothy Jacobs, and David Staack of the Department of Mechanical Engineering and Professor Chad Mashuga of the Department of Chemical Engineering.

All work for the thesis was completed by the student, under the advisement of Dr. Eric L. Petersen of the Department of Mechanical Engineering.

Funding Sources

This work was funded in part by the TEES Turbomachinery Laboratory of Texas A&M University.

NOMENCLATURE

a	burning rate constant (also called temperature coefficient)
AMPAC	advanced materials processing and analysis center
AP	ammonium perchlorate
APCP	ammonium perchlorate composite propellants
c^*	effective exhaust velocity
$C_{p,p}$	specific heat of propellant gas
$C_{v,ar}$	specific heat of argon
HTPB	hydroxyl–terminated polybutadiene
HTD	high-temperature decomposition
I_o	laser intensity
IPDI	isophorone diisocyanate
LTD	low-temperature decomposition
n	pressure coefficient in burning rate relation
$m_{p,p}$	mass of propellant gas
$m_{v,ar}$	mass of argon
$\dot{m}_{CO}$	mass flow rate of carbon monoxide
P	pressure
$\dot{q}_{flux}$	laser flux
r	radial direction
R	ideal gas constant

R45-M	specific blend of hydroxyl–terminated polybutadiene
r_b	burning rate
T	temperature
V	volume of the strand burner
z	axial direction
α	thermal diffusivity of the propellant
α_{rad}	absorption coefficient
γ	specific heat ratio
σ	characteristic radius

TABLE OF CONTENTS

Page

LIST OF FIGURES

Page

LIST OF TABLES

Page

CHAPTER I

INTRODUCTION

Composite solid propellants are typically used in rocket propulsion systems since they require simple and cheaper motor systems to propel the payload. Solid propellants come either as homogeneous mixtures, such as in the cases of double base propellants, or as heterogeneous mixtures of both fuel and oxidizer. Both propellant types can be easily cast into desired propellant geometries for mission-specific motors. Applications for these propellants span from the use of propulsion for space flight where the mission is limited by the payload weight to missiles which need to be simple and inexpensive because they are not being reused. Solid propellant are also being used as gas generators for airbags due to the simplicity in design and that they are cost effective. Over the last century, the focus of research has been to identify methods to tailor the burning rate for precision ballistics. Optimization of propellant formulations requires detailed modeling of the propellant's combustion characteristics such as ignition delay times, burning rate dependence on pressure, and combustion efficiency. Propellants are commonly tailored using various additives for both burning ballistics and mechanical properties. Mechanical properties testing has been done to evaluate the propellant strength for samples manufactured at Texas A&M University [1]. Current test methods provide the required information, but the available data are limited.

Experiments have been performed to provide the ballistic data required to compile propellant databases and models. Combustion efficiency testing is typically

done using full-size motors placed on thrust stands. In the context of rocket motor applications, the combustion efficiency is commonly determined by comparing the measured chamber pressure and mass flow rate (put in terms of the c* parameter) to the theoretical c* value assuming complete combustion as determined from a chemical equilibrium calculation. However, safely testing a full-scale or even small-scale motor can be very time consuming and costly. Strand burners are common for quickly evaluating the pressure dependence of the burning rate for solid propellant formulations. These tests are typically done on small, laboratory-sized samples, only a few grams at most, making them easy to evaluate quickly and relatively inexpensively. Although not currently derived from strand burner tests, a direct or even relative measurement of combustion efficiency would be extremely beneficial when assessing the performance attributes of various propellant formulations. Combustion efficiency measurements in a strand burner would not require costly thrust measurements to back out the specific impulse and c* efficiency. For example, small-scale testing could evaluate additives or aluminum consumption in a less-expensive and less time-consuming assessment.

In addition to propellant burning rate and performance, information on the ignition energy is also needed as an input to combustion models. Experiments evaluating the ignition delay time provide information on the ignition energy and can be used to study decomposition mechanisms. Many propellants have different decomposition pathways that can explain increased or decreased ignition delay times. Most ignition delay time experiments are performed in low-pressure strand burners due to optical constraints. Pressure effects on ignition delay times are not well understood, and there

are limited data available in the literature. Hence, there is a great need for high-pressure ignition experiments. By developing a method to measure the relative combustion efficiency and improving the techniques to measure the ignition delay time of a propellant sample, additive synthesis procedures can quickly be evaluated. Of interest to the present thesis study, an evaluation of the ignition delay time and combustion efficiency for a novel additive synthesis method, such as *in-situ* titania, can be rapidly performed and the results easily compared to the standard dry powder additive.

The focus of this dissertation is to first provide a literature survey of the established experimental techniques for strand burners and on ignition characteristics. The next chapter describes the strand burner facility at Texas A&M University and outlines the modifications for the new experiments. Chapters IV and V describe the first order models used to validate the experimental data collected. Chapter VII presents the data collected for the pressure-rise model and provides some discussion on the combustion efficiency. Measurement uncertainty analysis was also performed and is presented. Chapter VII provides the ignition data collected, comparing the results to literature values, and a discussion on the ignition mechanism. The final chapter gives a summary of the dissertation and concluding theories derived from this study.

CHAPTER II

BACKGROUND ON CONSTANT-VOLUME STRAND BURNERS

Strand burners are the most common methods of quickly collecting burning rate data for solid propellants. Requiring only small sample sizes, propellant strands, on the order of one inch, are burned over wide pressure ranges for typical motor operating conditions. Typically, strand burners are used to quickly evaluate the burning rate of a propellant formulation. This dissertation investigates new test techniques to better evaluate the performance of propellants. Both combustion efficiency and ignition delay times are of importance to better understand the propellant performance. By investigating the pressure rise in a constant-volume strand burner, details on the completeness of combustion are inferred. Similarly, the ignition delay times for propellants can be evaluated using a time-controlled CO_2 laser system to ignite a sample in a strand burner. This study examines propellants composed of ammonium perchlorate (AP) and hydroxyl terminated polybutadiene (HTPB). Provided in this chapter are background details on strand burners and measurements therein that relate to this dissertation.

2.1 Burning Rate Evaluation and Tailoring

Propellant burning rates are the metric commonly chosen to quantify the performance of a propellant formulation using a strand burner. In relation to the aerospace industry, solid propellants are burned in a laboratory setting at given pressures reminiscent of those seen in solid rocket motors, and the resulting burning rates are

plotted as a function of simulated pressure. Stand burners are found to produce burning rates which are very close to but approximately 5-10% below the burning rates in motors, due to the lack of high-temperature, convective environment in an actual the motor. According to Sutton and Biblarz, a power function, or "power law," which is also known as "St. Robert's Law or Vielle's Law", relates pressure and burning rate (Equation 1) [2].

$$r = aP^n \tag{1}$$

For Equation 1, r is the burning rate, a is an experimentally determined constant known as the temperature coefficient if evaluating the temperature sensitivity, P is the test pressure, and n is the burning rate exponent or pressure index. When burning rate is plotted as a function of pressure on a log-log scale, a typical propellant formulation displays a linear relationship fitted by Equation 1. The pressure index determines the sensitivity to pressure, which can easily be seen as a slope change.

One way to increase the burning rate in a AP-based composite propellant is with the reduction of AP particle size. AP particle size reduction allows for better dispersion throughout the propellant and an increased reactivity with the binder. This reduction in AP particle size causes combustion behavior between the AP and HTPB reactants to approach that of a premixed regime in which the reaction takes place faster, and the flame burns hotter resulting in an increased burning rate. Jeppson et al. provided an illustration of the effect of AP particle size on burning rate showing how decreasing particle size changes the combustion regimes [3]. Conversely, larger AP particle sizes tend to burn as an AP monopropellant flame (Figure 1).

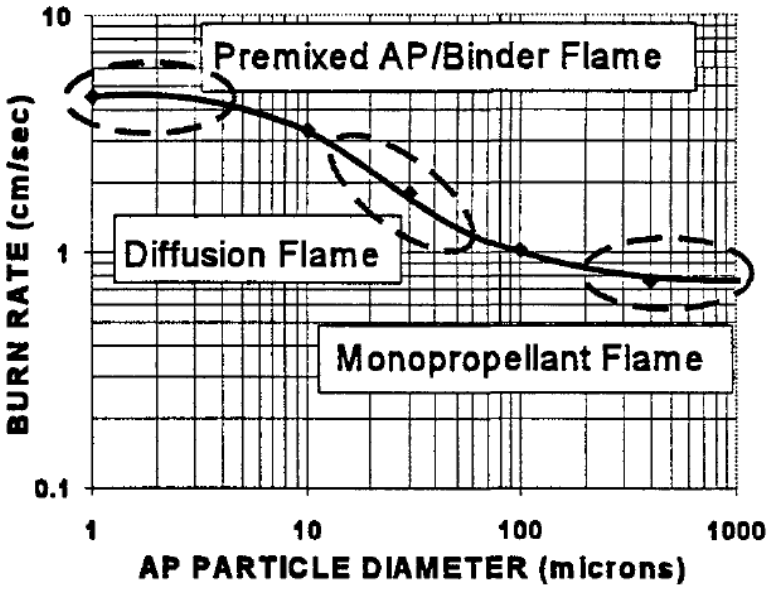

Figure 1 Effect of particle size on the burning rate of an AP/HTPB propellant and the flame behavior; plot is copied directly from [3].

A second impact on burning rate caused by the oxidizer is based on the "mode" of the propellant formulation. That is, a "monomodal" propellant consists of one oxidizer particle size ("size" referring to the particle's diameter). Likewise, a "bimodal" propellant has peak distributions of oxidizer crystals of two sizes. By extension, a "multimodal" propellant contains at least two oxidizer particle sizes, but it is more likely to refer to formulations of three or more crystal sizes. Increasing the modality of the formulation allows for additional oxidizer particles to be dispersed in the propellant in areas in between larger particle sizes that would otherwise be empty, thus increasing the oxidizer particle packing efficiency of the composite propellant. This increased packing is often done to increase the solids loading in the propellant. The increased surface area

contact between the AP and HTPB allows for greater reactivity and hence greater burning rate due to the increase in reaction sites.

Tailoring the performance of composite solid propellants relies on the use of various additives and additive sizes. While solid propellants are formed using a majority of binder, fuel, oxidizer, and curative by mass, other materials are often introduced, in relatively small quantities, to augment distinct parameters of the propellant. Different additives improve individual aspects of the propellant such as shelf life, elasticity, and combustion performance to meet desired mission objectives [2, 4]. The use of nano-scale particles can have completely different surface chemistry, often better than their micron-sized counterparts [5-9]. By altering the crystalline structure, many oxides can be made more catalytic [10, 11]. Studies on the decomposition of AP are important for the optimization of the burning of AP/HTPB propellants. Understanding where an additive participates in the reaction can improve the combustion process. Iron oxide, copper oxide, and titania are the most commonly studied catalysts for AP/HTPB propellants. Iron oxide and Copper (II) oxide are believed to aid in the Low Temperature Decomposition (LTD) of AP [12, 13]. Other studies have shown that the use of titania reduces the temperature for high-temperature decomposition (HTD) [9, 14-16]. Burning rates of a more-catalytic additive would be higher from the combustion being nearer to completion. Typical combustion evaluations are done through the use of differential scanning calorimetry (DSC) and Thermogravimetric analysis (TGA). All of these data can be used to improve the burning rate and possibly even the combustion efficiency of AP/HTPB propellants.

Recently a new method for synthesizing TiO_2 (titania) directly in the binder of an ammonium perchlorate composite propellant (APCP) has been developed in the author's laboratory [17]. This process, termed nano-assembly or *in-situ* synthesis, has been shown to increase the efficiency of titania as a burning rate catalyst in APCPs, as described in more detail below. This novel method presents three main benefits compared to traditional nanoparticle additives. First, by minimizing particle/agglomerate diameter, the surface area-to-mass ratio is increased. High surface area-to-mass ratio nanoparticle additives have been shown to increase catalytic activity during ammonium perchlorate decomposition and APCP combustion [18, 19]. Second, by assembling the particles, and in the limiting case composite mixtures, from the bottom up, surface chemistry, dispersion, and particle topography can be controlled in such a way as to tailor the burning rate of the propellant without resorting to extreme oxidizer particle size changes. Finally, by synthesizing the particles directly in the propellant binder, safety and health risks associated with the handling of "dry" nanoparticles are mitigated [20].

Additives dispersed with the pre-mixing method exhibited better dispersion properties and increased performance compared to standard dry mixing [20]. Nano-assembly (i.e., *in-situ*) is the latest and most effective generation of these nanoparticle synthesis techniques. By synthesizing the particles *in-situ* with the HTPB binder, agglomeration is minimized, and a high-quality nanoparticle dispersion, without settling or segregation, is achieved. The *in-situ* method has been seen to consistently produce nanoparticles with diameters ranging from 5 to 25 nm [17, 21]. An example SEM of the

particle dispersion using the *in-situ* synthesis benefits can be found in Figure 2, taken from work by Demko et al. [21]. The dispersion is best seen using electron dissipating spectroscopy (EDS), since the elements can be individually highlighted.

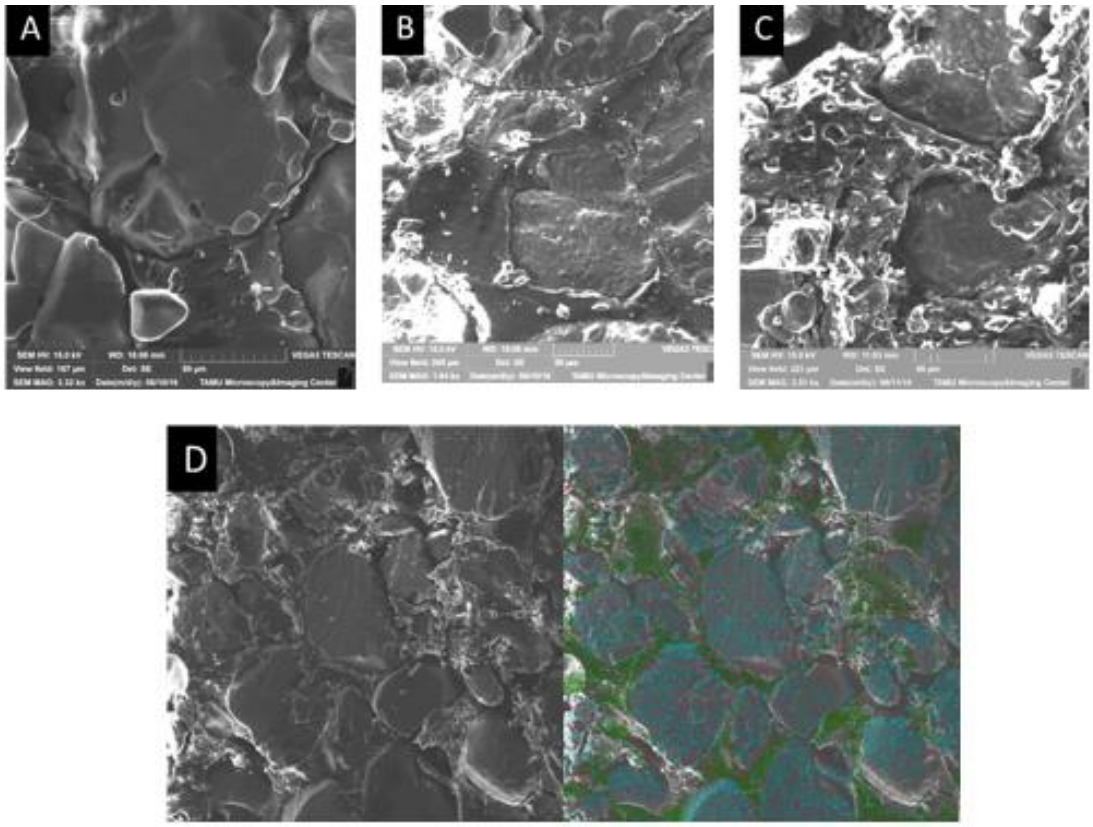

Figure 2 SEM image of 80% baseline (A), 0.4% dry-powder iron oxide (B), and 0.4% *in-situ* iron oxide (C) propellant surfaces. Note that the iron oxide particles were observed as small, bright dots of the dry powder indicating larger agglomerates. EDS image (D) shows the location of the iron oxide on the surface of the *in-situ* propellant. The color mapping has iron oxide in red, carbon in green, and oxygen in blue [21].

2.2 Pressure Rise Measurement and Evaluation

Crawford strand burners are commonly used to test the burning rate of solid propellants. Burning rate is collected under rapidly changing pressures, often using high-speed photography break wires imbedded in the propellant [22]. Typically, the pressure vessel is pressurized using an inert gas, nitrogen being the most popular, and the propellant is ignited. The burning surface is visually (or otherwise) monitored, and the burning rate is calculated using the change in distance divided by the time taken from the camera or wires embedded in the propellant [23-26]. Closed-bomb pressure vessels agree well with full-scale testing, but smaller vessels tend to be susceptible to heat loss. Typically, vessels which are greater than 700 cc are not significantly impacted by heat loss [27]. The pressure vessel used in this study and all studies at Texas A&M University is approximately 1.5 L (1500 cc), thus heat loss effects are minimized. Experimental error on surface observation in the video is between 2- to 5%, but knowing the heat loss and the equation of state for the gasses, the pressure time history can be used as an accurate alternative to a video measurement [28, 29]. It is believed that there is information hidden in the pressure rise that is missed by only analyzing the video. Since the pressure rise is generated from the combustion gases, then the pressure rise has a dependency on the flame temperature of the propellant. As is shown in the following and in later chapters, is it precisely this measured pressure rise in the vessel that occurs during a sample burning experiment that holds the necessary information from which one can infer a corresponding combustion efficiency in addition to gleaning just burning rate from a given experiment.

To better understand the pressure data collected from constant-volume strand burners, first principle models of the burner can be created, and some attempts can be found in the literature. It was first proposed that the pressure rise in a constant-volume strand burner could be calculated by multiplying the internal energy by a function of propellant mass and available volume. Applying the Nobel-Abel equation of state for gases, the state function is multiplied by an expression for energy, and the pressure rise could be predicted [30, 31]. Another model calculates the burning rate based on the results from the pressure versus time using ideal mixing laws. By manipulating the conservation equations for a closed system and the ideal equation of state, the burning rate could be retrieved. Assuming the mixture follows Dalton's mixture model, partial pressures could be used to calculate the pressure at any instant in time. A relationship for pressure and mixture properties was used to predict the final pressure in the chamber after combustion [27, 32].

This first model however lacked the inclusion of heat transfer out of the vessel. Modifications were made to incorporate heat losses to more accurately model the pressure rise in the constant-volume burner. Heat loss is dependent on the flow field generated by the burning propellant strand. Research by Glick et al. used flow field analysis to account for heat losses on testing larger 2×4 inch motors. Average burning rates were calculated using the initial length of the strand and obtaining the burn time from the pressure trace [33, 34].

Additional research into accurately modeling the pressure rise in a constant-volume strand burner was supported by Sandia National Laboratory. Improvements were

made by incorporating the burning rate with heat loss as described by Glick, and adding more detailed information on species and condensation. Using NASA CEA to determine the mixture composition of the propellant exhaust gasses, the amount of water was determined and applied to the condensation calculation [35-38]. The results indicated a good prediction of the final pressure, but left room for improvement. Further developments were made in a study by Frazier to more accurately model the condensation by treating the strand burner as a quasi-open system allowing the propellant gasses to enter the control volume. Figure 3 summarizes the approach used to model the vessel [16, 39]. Improvements to the model by Frazier were made in the current study and are applied to the propellant analysis (see Chapter 3.10).

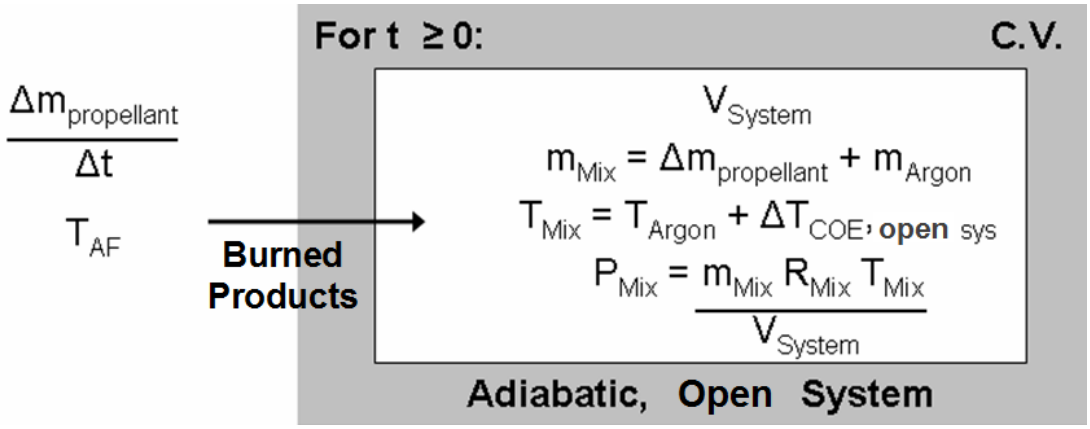

Figure 3 Frazier strand burner modeling concept to determine changes in pressure and temperature; figure taken directly from [16].

One of the key combustion limitations is the imperfect mixing of the fuel and oxidizer. Wide AP distributions in composite propellants can produce anomalous behavior due to inadequate mixing. This study was performed to show how anomalous behavior of a plateau propellant and the consumption of aluminum could be observed in the pressure rise of a constant-volume strand burner; if the wide-distribution propellants limit the AP from reacting, then the resulting heat of combustion would be lower. Similarly, micron Al is often used in large mass percentages as a fuel (up to about 15% or more) and is difficult to fully combust. The concept of measuring combustion efficiency can also be extended to the effectiveness of catalytic additives. If an additive contributes to the combustion process generating more energy from combustion, it would be thought to increase the combustion efficiency of the propellant. The catalyst would be seen as a more effective additive if it catalyzed the burning rate while also contributing to an increased combustion efficiency. This thesis examined the synthesis techniques of titania and compared the catalytic activity of dry-powder, pre-mixed, and the *in-situ* synthesis techniques, as is detailed in later chapters.

2.3 Ignition Delay Time Measurements

Ignition studies on solid energetic materials have been a large focus of research to obtain fundamental understanding of the ignition process and for benchmark data for improving ignition-prediction capabilities. Many studies have examined the use of a high-power laser as the source for ignition. Laser ignition provides a transient, multidimensional ignition behavior due to the Gaussian nature and the short time of laser

heating. Modeling has produced accurate simulations for the ignition delay times of various solid propellants by utilizing the conservation equations. After applying the conservation equations to the various surface phases of the propellant during combustion, ignition modeling is able to incorporate combustion using phase change and burning rate information. Predictive laser ignition models have been developed for a wide range of solid energetic materials [40, 41]. Granier et al. [40] modeled the ignition of thermites by examining the phase change and burning rate of the propellant formulation, while Meredith et al. [41] developed a similar model for HMX propellant.

Experimental procedures for collecting ignition delay time measurements have been established in strand burners. Cain and Brewster determined that the radiant ignition of AP and HTPB propellants by laser radiation is strongly influenced by the ability to absorb the 10.6-μm wavelength photons from a CO_2 laser. The effect of adding metal oxides were found to be minimal for the ignition delay timing due to the lower absorption at the 10.6-μm wavelength [42]. Metal oxides are typically added in small quantities, which would minimize the changes in the thermal properties. Zanotti and Giuliani first applied a laser to heat up the surface of a solid propellant to its ignition temperature using a 70-W, continuous wave CO_2 laser [43]. Aiming the beam down the top of the test apparatus through a zinc selenide (ZnSe) window, the beam ignited the propellant. The ZnSe window was used since it allows the 10.6-μm beam to be optically transmitted through the material. Since previous tests were run at low pressures, the low fracture strength and the corrosion of the ZnSe window were not issues. First light and first gasification are the two main criterion for quantifying the time of ignition. Ignition

time was determined based on a go/no-go burning criterion which was stated to be the time when combustion was sustained upon interruption of the radiation flux, and not at first light [44].

As seen in later chapters, the present study required a control mechanism to limit the beam delivery and monitor the time that the laser radiation acted on the propellant surface. An electro-mechanical shutter was used to control the delivery of the beam to the propellant surface with a clock speed of 20 to 60 ms, thus limiting energy and providing the time of delivery to the propellant surface. The laser power was varied from 60 to 400 W/cm^2 and was aimed on the top of the propellant surface [45].

Methods of altering the ignition properties are another area for research. Arkhipov and Korotkikh expanded further with the improvement of the ignition of the solid propellants with a catalytic additive by studying the effect of the size of aluminum powder on the ignition of propellants. They concluded that the addition of ultrafine aluminum powder reduced the ignition delay time using their 100-W laser when compared to the results obtained using the larger-sized aluminum. It was found that the greatest effect on the ignition time was by changing the course-to-fine ratio of the AP [45]. Aside from varying the ingredients, an effective way to decrease the ignition time, unsurprisingly, was found to be increasing the power output from the laser [42, 46, 47]. Many studies are being performed for new ignition methods for energetic nano-materials (nEM). New optical methods are being developed to ignite different materials using a high-intensity light. For example, when single-walled carbon nano-tubes are exposed to

a flash of focused light that was generated using a camera flash, the carbon nanotubes ignited the nEM [48].

This thesis focused on the development of an ignition timing measurement for APCPs and the effects of different catalysts. After validating the ignition measurement system on baseline propellants, novel catalytic-additives were examined. APCPs are widely used in research for solid propellants. Previous research by the author has shown that the inclusion of nano-additives manufactured using novel techniques, such as titania and cerium oxide, will increase the burning rate of AP/HTPB composite propellants. Metal oxides can be synthesized using various techniques by changing their morphology to tailor their catalytic behavior [9, 15, 18, 42, 49].

Most studies used a CO_2 laser with a wavelength of 10.6 μm; the present study used the same CO_2 laser wavelength at a power ranging from 30 to 100 W. AP and HTPB propellants have been shown to have high absorption and low reflection at this 10.6-μm wavelength. Fine AP particles and carbon black can be added to the propellant to aid in ignition by increasing the opacity of the propellant, allowing more energy to be absorbed [42, 50]. Properties of nano-additives vary as the synthesis method is changed, and they can affect the ignition behavior. Although literature investigates propellant formulations that are different from those herein, they are similar enough for at least a qualitative comparison [42, 47].

Identifying how the catalyst decomposes the AP would be indicated in the ignition delay time. Current theories state that titania aids in the high-temperature decomposition of the AP, and iron oxide has been shown to aid in low-temperature AP

decomposition [16, 39, 51, 52]. The propellants burned by Brewster and coworkers were an APCP that used only fine AP (2 μm) at 76% by weight of the propellant. Smaller AP particles were shown to lower the ignition delay time. Using small AP sizes in combination with testing at a lower pressure (0.1 MPa as opposed to 4 MPa) prevents a direct comparison, but the results serve as a good indication of the expected time scales.

CHAPTER III

TAMU CONSTANT-VOLUME STRAND BOMB

3.1 Apparatus Description and Modification

Testing at Texas A&M University was performed in a constant-volume strand burner designed in house to sustain high-pressure testing. More information on the design of the strand burner is provided by other studies [53, 54]. The strand burner is rated at 55.2 MPa (8000 psi), and the propellants were tested at pressures up to 27.6 MPa (4000 psi). During every experiment, pressure, light intensity, ignition timing, and spectral data are recorded. The pressure and light data are recorded using a data acquisition board from Gage Applied Sciences that was used to establish the burning time. From the data collected, the pressure rise is recorded as a function of time, and the ignition and burn out times are determined therefrom. From the change in time, the average burning rate is calculated from the initial length divided by time for each propellant strand.

Previously, the solid propellants were always ignited by a high-energy wire to initiate the deflagration of the propellant. Typically, high current is passed through a very thin metal wire that is placed over the propellant surface. The wire must be pressed against the propellant surface, and then a high current is run through the wire which then gets red hot and subsequently initiates combustion. One drawback of using the wire-ignition method is that the precise time between applying the energy to the wire and the

time of actual ignition of the propellant is difficult to quantify accurately enough to measure ignition delay times.

A new method to ignite the propellants without the use of a wire has recently been implemented at Texas A&M University to perform burning tests of solid rocket propellants. This method uses a 100-Watt CO_2 laser directed onto the top of the propellant surface. There are several advantages to using a laser, one of which is the ability to determine the precise time at which the ignition source is applied to the propellant, allowing of accurate determination of an ignition delay time. The laser is the 100-Watt Synrad firestar f100 model laser, which produces a high-purity beam of 2.5 mm diameter at a wavelength of 10.6 μm.

Using the laser to ignite the propellants eliminates the need to imbed the ignition wire into the propellant, reducing the risk of damaging the propellant surface. In addition to precise timing of the event, the laser allows for a more-uniform heating of the propellant surface rather than just the thin surface area of the nickel-chromium (nichrome) wire that is wrapped over the propellant for testing. Ignition with high-intensity lasers has become common to igniting solid propellants, as described in the previous chapter. Applications include the ignition of thermite powders with the ability to measure the energy input to the propellant [55] as well as determining the ignition delay times for propellants with various additives [56]. The work in this thesis is based on the work by Demko et al. for how the ignition delay times are changed using common catalysts [57].

To ensure that the strength requirements were met for the present high-pressure study, zinc selenide (ZnSe), zinc sulfide (ZnS), and germanium (Ge) window materials were evaluated using the criteria for high strength and optical transmission. The strength was evaluated using Eq. 2 to estimate the thickness required for a given diameter and maximum test pressure [58].

$$t_W = 0.5 A_W \left[K_W f_s \frac{\Delta P_W}{S_F} \right]^{1/2} \qquad (2)$$

where t_W is the thickness based on the unsupported aperture diameter A_W, subject to the pressure differential ΔPw. K_w is 1.25 for being unclamped, and the factor of safety is given by f_s and the fracture strength by S_F. While ZnSe had the best transmission properties, its fracture strength was too low and would require too thick of a window. To pass the beam into the high-pressure strand bomb, a ZnS window was used for its combination of higher fracture strength and optical transmissivity. The ZnS window was mounted in a stainless steel insert to replace the existing acrylic window. Figure 4 illustrates the new window insert for the ignition system; the complete Solidworks drawing can be found in the appendix.

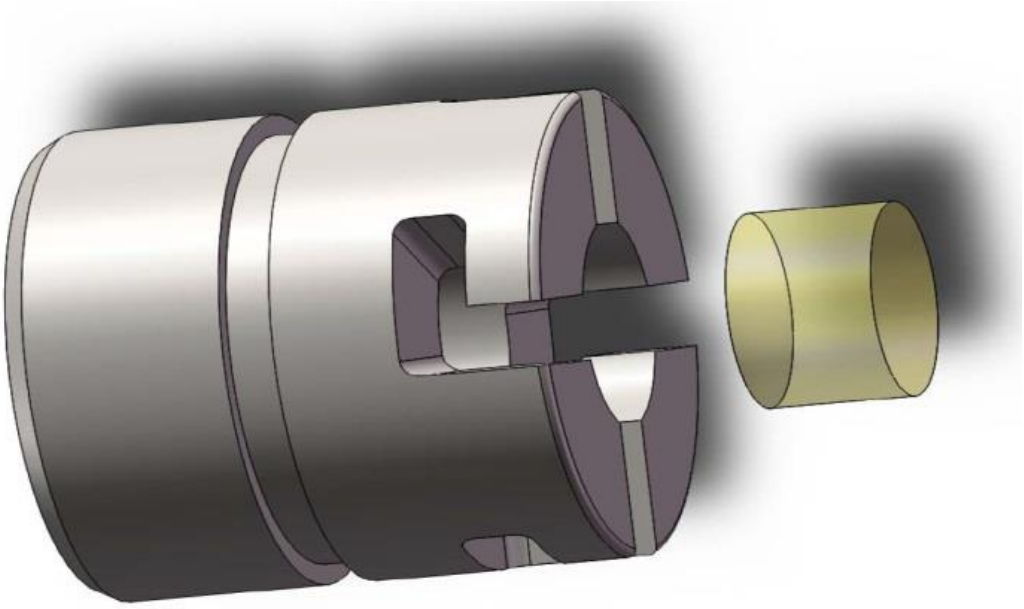

Figure 4 Designed window insert for the laser transmission.

3.2 Experimental Procedure and Data Analysis

Determining the ignition time requires an accurate determination of a time zero, i.e., the time the ignition source is first applied to the sample. In the present experiment, such timing of the event was recorded by using a second light (blue LED) at a different wavelength passing through the same shutter as the ignition laser. When the shutter is closed, both the CO_2 laser and the second, blue light through the shutter are both blocked simultaneously. Figure 5 is a schematic of the test facility, and Figure 6 is a timing diagram showing the ignition delay time for a baseline propellant. To ignite the propellant, the shutter is opened and the blue light hits a photodiode producing an output signal while the main CO_2 laser strikes the surface of the propellant. Using a simple

control system, the shutter is set to close once light is emitted from the combustion process. This signal from the second, blue laser indicates the duration which the shutter is open (i.e., when the laser is providing energy to the propellant surface); the time between the shutter closing and the first appearance of the light from the combustion process provides the time required to ignite the propellant, i.e. the ignition delay time. Figure 6a plots over the entire test time and figure 6b is a magnified view of the shutter timing and how the ignition delay time was recorded. The shutter line opens activating the camera, then the shutter closes when the light and pressure sharply rise, and sustained combustion is established.

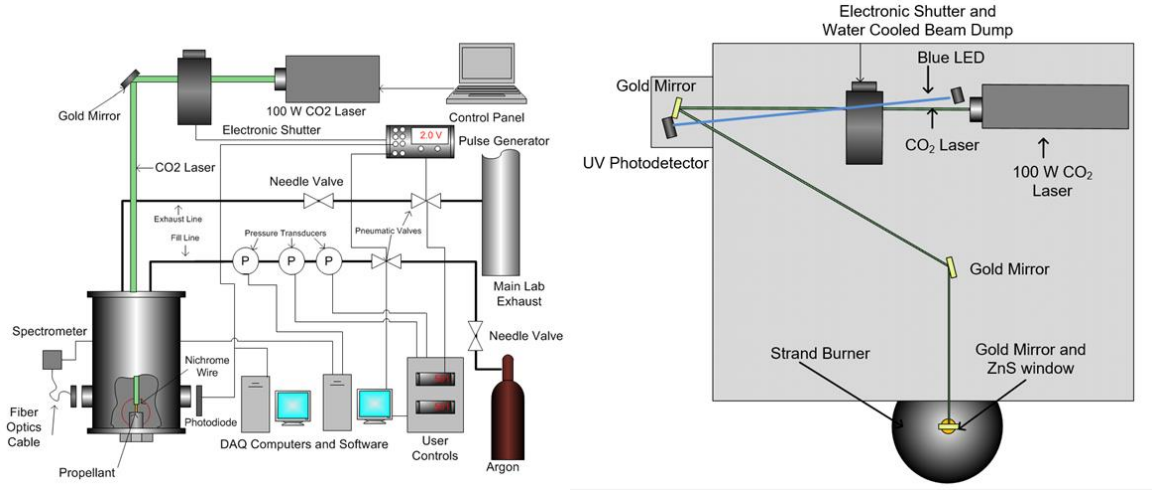

Figure 5 Detailed schematic of the strand burner utilizing the CO_2 laser ignition system. The schematic illustrates how the three pressure transducers and the photodiode are used for data collection and calibration. The right-hand schematic details the optical setup, showing the primary and secondary light source, the shutter, and the secondary-light photodetector.

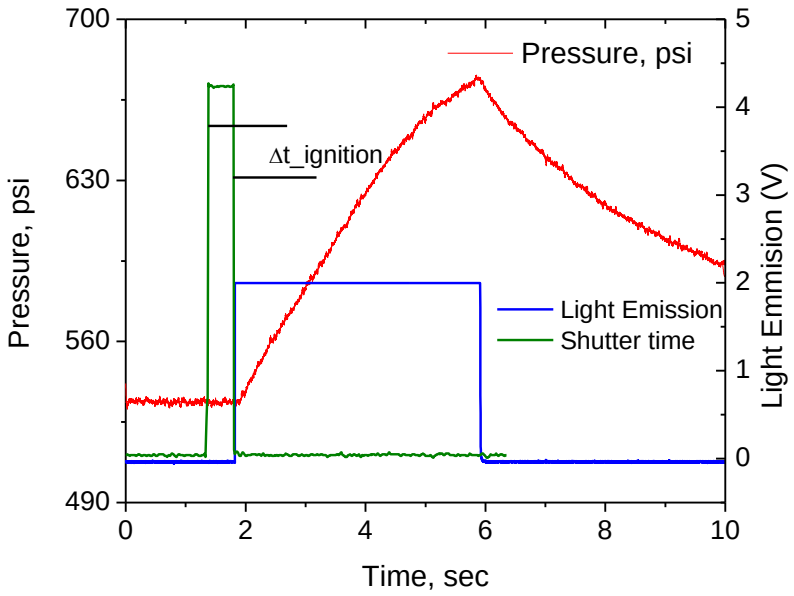

(a) Pressure and light trace over full test time.

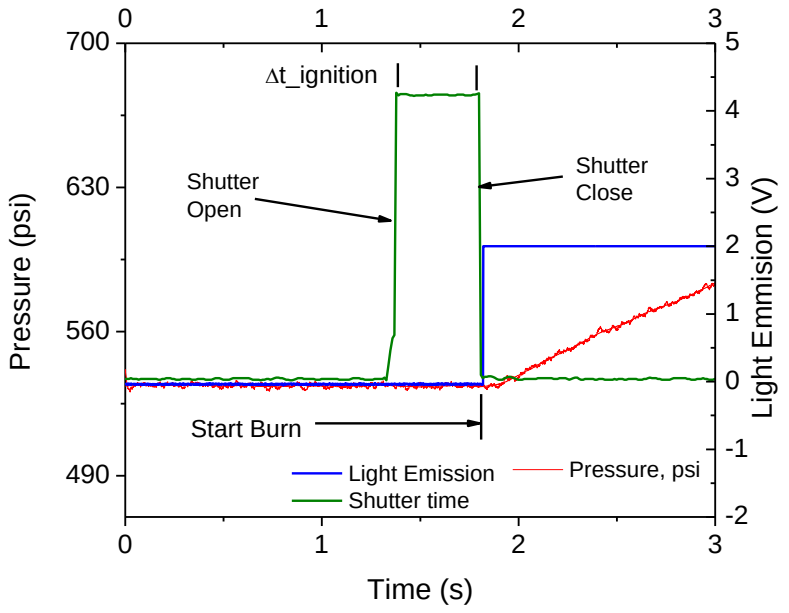

(b) Magnified trace to highlight the shutter timing.

Figure 6 Sample pressure and light trace for a baseline test. The green line was used to determine the ignition delay time, and the blue line confirmed the pressure-based burning time.

The present thesis is concerned with ignition testing of AP/HTPB propellants with different nano-sized particles and catalytic additives (such as *in-situ* titania particles). Testing was performed at elevated pressures in the range of 3.5 to 15.5 MPa (500-2250 psi), and ignition delay times were recorded as a function of the varying pressure. To accurately measure the ignition delay time over the pressure range, a repeatable power output of the laser must be known. The laser power will set the time scale required for the operation of the ignition detection system. To know the amount of energy striking the surface of the propellant, a Peltier tile was placed in the burner in place of the propellant strand. One side of the tile was blackened with graphite, and a heat sink was mounted to the other side. Measuring the voltage from the Peltier tile provided a power output calibration curve. The laser was then turned on, and the power delivered to the propellant strand was recorded over a range of power settings; the results can be seen in

Figure 7. The power was obtained by integrating the power under the curve from the diameter of the propellant strand. Then, the power was divided by the surface area of the propellant strand. This measurement process was used before and after testing each series of samples to verify that no significant change had taken place from test to test, such as misalignment of the laser, dirty windows, etc.

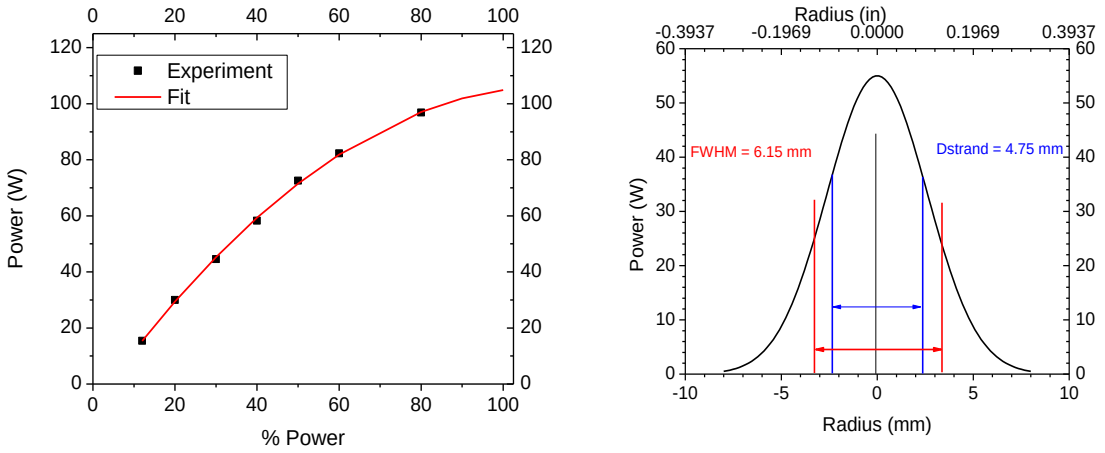

Figure 7 The power setting on the laser as compared to the power measured using the Peltier tile. Calibration was performed using a 30-W heater (left). Gaussian profile of the CO_2 laser beam calculated at the surface of the propellant, relative to the diameter of a typical propellant sample (in blue).

To verify the calculation, an optical iris was placed in front of the Peltier tile with the opening set to the diameter of the propellant strand. Using the optical iris, the extra energy from the beam divergence was blocked, and the resulting power measured by the tile would be the power striking the propellant surface. Calibration of the measurement was done by moving the iris until the power output on the tile was maximized, indicating centering of the beam. The power was then measured and corrected for the power flux impact on ignition delay time. Figure 8 shows the experimental setup for measuring the power of the laser impacting the propellant strand.

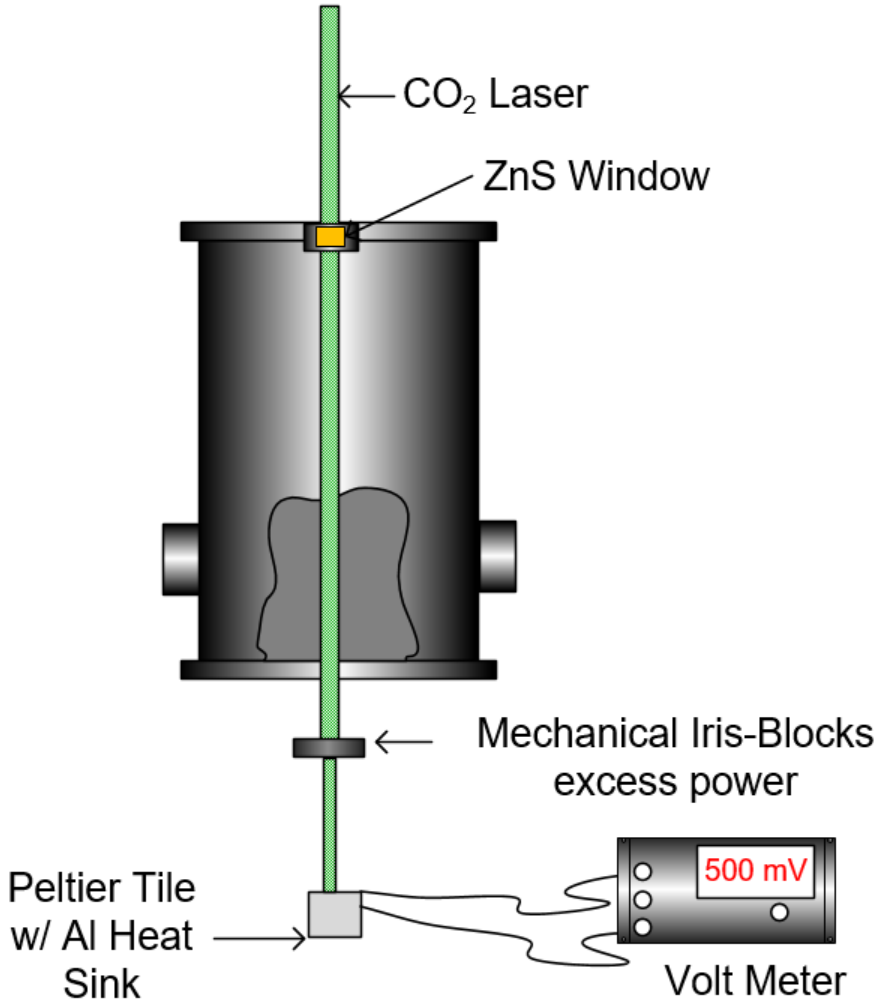

Figure 8 Power measurement system using the optical iris to block energy of the diverging beam greater than the propellant diameter.

A power setting of approximately 80 W was first tested resulting in inadequate resolution for time. To estimate the power flux, the beam diameter was measured using an IR detection card and was approximated to be about 6.6 mm. Then the radius was confirmed by applying a Gaussian beam profile to the given laser specifications, but the power and power flux were calculated by integrating under the power curve for the

propellant diameter. A full width half maximum (FWHM) was calculated to be 6.15 mm. The power level was lowered to approximately 55 W (roughly 60 W/cm^2). Ignition delay times could then be reproducibly and accurately collected at this lower power setting.

Uncertainty in the system arises from several contributing factors. One of main contributions is from the opening (40 ms) and closing (29 ms) times of the shutter. Another important factor is the accumulation of soot on the optical window above the propellant. As the propellant burns, the combustion products are expelled in the direction of the window through which the laser passes. The laser power is reduced if any soot is left on the window because the soot absorbs a portion of the energy supplied. Soot can also cause wear on the optics surface, which can in turn also alter the optical properties.

3.3 Change in Pressure

Propellant testing at Texas A&M University occurs in a constant-volume strand burner, mentioned briefly above. A propellant sample of approximately 1 g is inserted into the strand burner and ignited. The propellant burns at a temperature near 3400 ^{o}F, producing combustion gases at such temperatures which heat the pressurizing gas in the strand burner. Since the volume remains the same, the pressure increases during each test, as mentioned in Chapter 2. Figure 9 plots a typical pressure trace produced during a test.

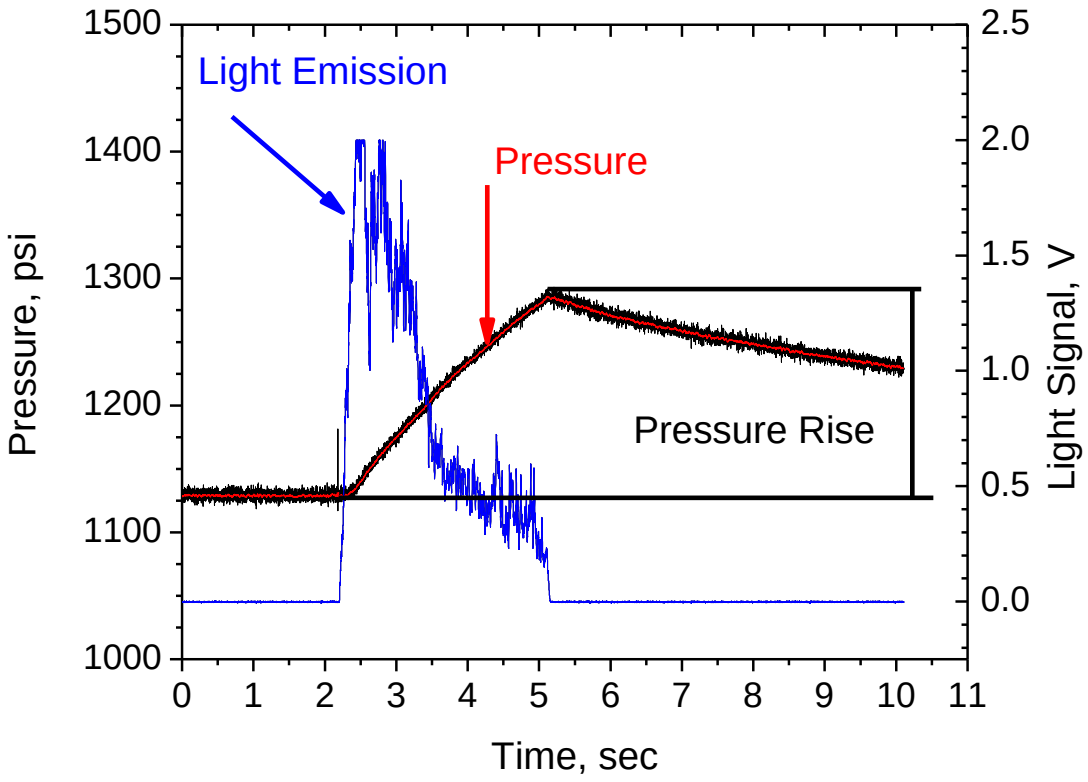

Figure 9 Pressure trace from a typical propellant burn.

The capability to analyze the pressure rise provides unique benefits to constant-volume strand burners, such as analyzing the pressure rise. The pressure rise generated is known to be related to the amount of heat released during combustion. By examining the pressure rise, more information on the propellant's combustion efficiency can be identified. If two identical formulations are compared, the pressure rise should be the same. In the case of AP sizes, the propellants with a smaller average AP size are thought to burn more completely due to reducing the diffusion limitations. Hence, one would then expect the pressure rise for a propellant made up of smaller AP particles to be larger

than the pressure rise of a propellant comprised of larger AP particles, all other things the same (same weight percentages, etc.). This concept can be stretched to the evaluation of the synthesis process of a catalyst, such as titania, where is a given additive provides a higher pressure increase than a comparable baseline, then it would be contributing to an increased combustion efficiency in addition to catalyzing the burning rate.

When performing experiments over the past decade at TAMU, the author and his collaborators have noticed that the observed pressure rise from test to test is also dependent on the average pressure of the experiment. Such a pressure rise dependence on test pressure is plotted in Figure 10. This correlation between peak pressure increase and the average test pressure is explored in detail in Chapter 4.

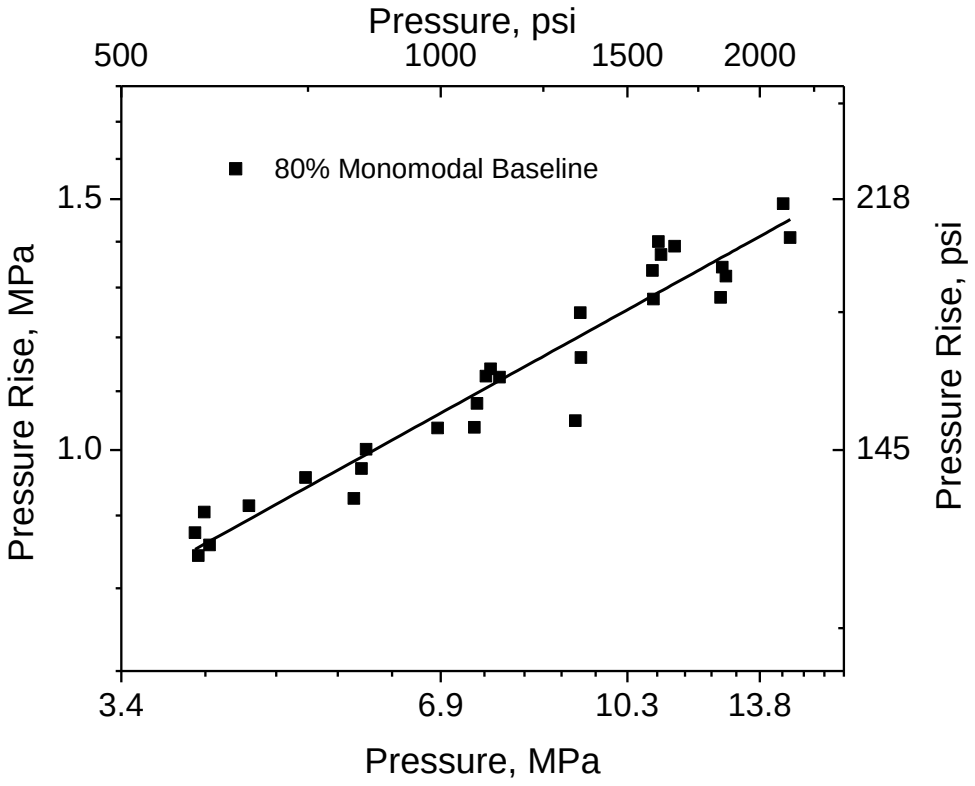

Figure 10 Pressure rise of an 80% monomodal baseline using 200-μm AP particles.

3.4 Ignition Delay Time

Typically, propellant samples are ignited using a hot wire or electronic match. This ignition process is done by flowing a large current and voltage through a small wire, typically made of nickel-chromium (nichrome). In the author's laboratory, the voltage is set to 18 volts and the current is set to 6 amps, thus the power can easily be calculated, but the difficulty arises from the contact area. Each test requires the wire be folded over the top surface of the propellant and does not always have the same number of contact points. Calculating the area of the wire in contact of the propellant

becomes too complicated and highly non-repeatable. shows how the wire can lift off the propellant surface and ignite on opposite ends of the propellant. While the wire method is reliable for most tests, when one is concerned with precise timing of the ignition event it is insufficient.

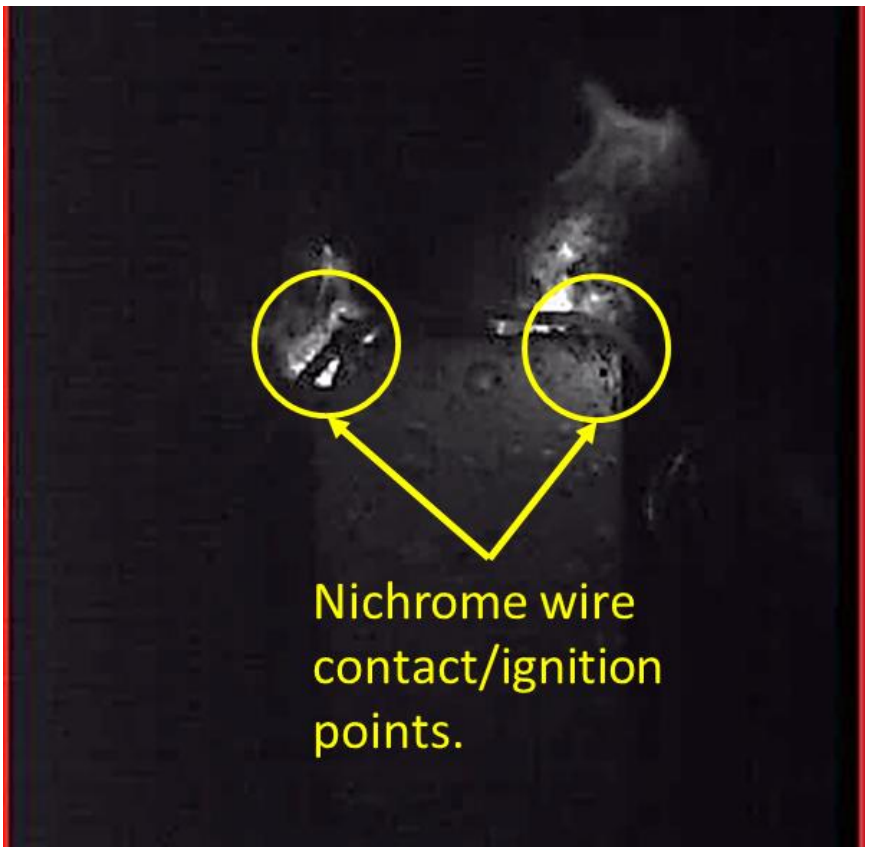

Figure 11 Ignition image using nichrome wire.

Using the CO_2 laser, the energy input into the propellant strand is easier to calculate. By applying basic Gaussian optics, the beam size and power distribution can be calculated, and the power is maintained using the laser's control pad. Ignition energy was simply calculated and was found to be highly repeatable from test to test. Figure 12 shows the point of ignition for a single propellant strand, and is representative of every test completed. Typically, ignition is always the approximately the same size and in the same location on the propellant strand. The only variation seen were to the presence of metal particles ejecting from the surface in the metalized propellant strands or if the propellant strand shifted during the purge and pressurizing process.

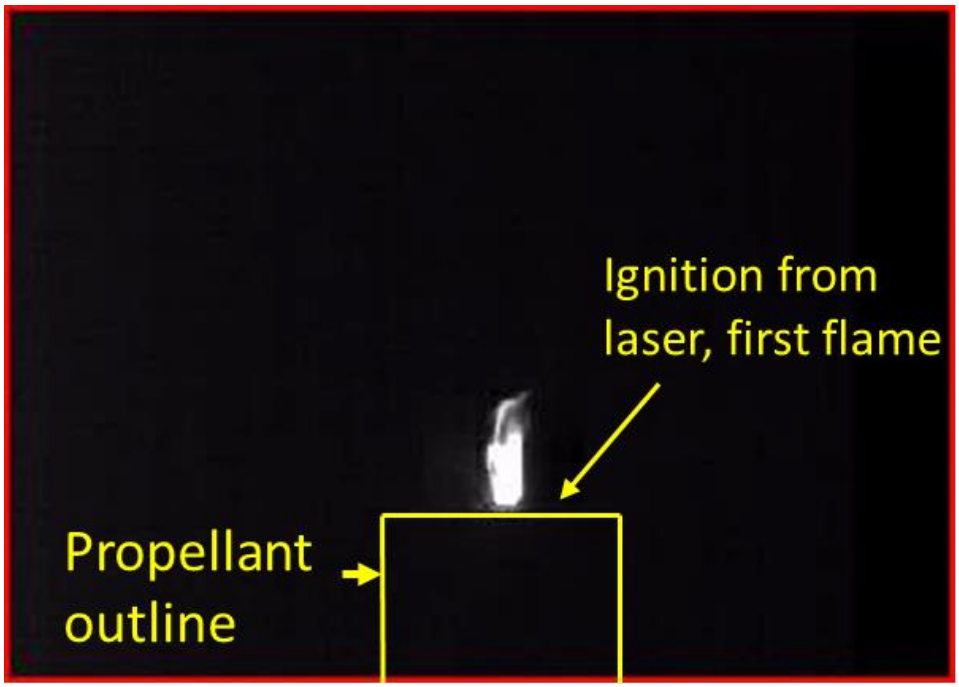

Figure 12 Ignition event using the CO_2 laser.

The reason for collecting the ignition delay time data was to identify the ignition energy for the propellant strand. This thesis establishes an experiment that was then applied to propellants containing novel catalysts developed during a collaboration between the University of Central Florida and Texas A&M University. Data collected could then be used in propellant models to simulate their combustion in a full-scale rocket motor.

CHAPTER IV

COMBUSTION MODEL VALIDATION

As a first step in the development of the new experiment techniques herein, simple models based on fundamental principles were created to check the validity of the measurements and to better understand the nature of the phenomena observed in the experiment. Literature shows little if any research on using the pressure rise as an estimate of chemical c* efficiency, but a few have studied the pressure rise that occurs during a constant-volume strand burner experiment. A first step was to calculate the theoretical propellant performance of the mixtures studied, then use the performance parameters as inputs into thermodynamic relationships for calculating pressure and temperature. It should be noted though that the model developed in this thesis is not intended to exactly predict the resulting pressure rise and capture all of the physics, but rather to verify whether there is merit to the interpretation of the experimental results—that is, using the measured pressure rise and differences therein to infer difference in combustion efficiency from propellant to propellant.

4.1 Propellant Performance Evaluation

Currently, there are several methods to evaluate the chemical equilibrium properties of propellants. Most codes output the adiabatic flame temperature, mixture specific heats and gas constants, specific impulse, characteristic velocity (c*), and several other desired properties. The program used at Texas A&M University is the free

code ProPEP. This software allows the user to add uncommon ingredients to the chemical databases.

4.1.1 Program (ProPEP)

ProPEP is a thermo-chemical program used to evaluate the theoretical performance of solid and liquid propellants, allowing the user to see the equilibrium conditions of the combustion process. Any user can alter the ratios of the propellant ingredients and calculate combustion conditions to achieve desired equilibrium gas properties. ProPEP provides the inputs that the strand burner model is able to utilize, such as speciation, species concentration, gas mixture molecular weight, and adiabatic flame temperature as inputs.

ProPEP determines chemical equilibrium by guessing at the equilibrium composition iteratively. The basis for this method of finding chemical equilibrium is a combination of Villars' method and a method obtained from H. N. Browne. In this setup, Villars' method of a linearization and Taylor series expansions are employed with improved computational methods to find the chemical composition, and Browne's method is used to optimize the baseline (the predetermined subset of molecular species formed by chemicals present in the reaction, according to Browne et al., 1960) and speed up convergence [59, 60]. The significance of Browne's method is that it introduces the concept of the "optimized" basis, in which the system components are present in the greatest possible molar amounts [61].

Enthalpy balance iteration technique is used to find the final temperature of the products and thereby the remaining thermodynamic properties of the system at

equilibrium. Both Newton's Method for interpolation and a Bisection Method (referred to in Cruise as Interval-Halving) were employed to determine the adiabatic flame temperature. The iterative processes determines the adiabatic flame temperature (T_{AF}) via comparison of heats of the reactants to the heats of the products based on guessed temperatures reminiscent of combustion science problem solving [62, 63]. Since the heats are a function of temperature, the temperature that provides total product enthalpy equal to the total reactant enthalpy is the adiabatic flame temperature (Equation 3).

$$\sum H_{Reactants\ @T=T_{initial}} = \sum H_{Products\ @T=T_{AF}} \tag{3}$$

To calculate the necessary chamber conditions, ProPEP makes the following assumptions regarding the combustion process, assuming the process is occurring in a rocket combustion chamber, which is the primary application of the code: [61]

1. Kinetics occur fast enough such that equilibrium is reached within the chamber prior to the combustion products leaving the chamber and entering the nozzle of the rocket motor (nozzle consideration is for exhaust flow calculations not applicable to this study).
2. The process is adiabatic, and no heat is transferred beyond system boundaries. The enthalpy of the reactants is therefore conserved in the enthalpy of the products, as in Eq. 3.

3. All gas species in the products follow the Ideal Gas Law and also obey Dalton's law for partial pressure calculations.

Additional considerations include: constant pressure throughout the combustion process in the chamber and that the gram weights entered are correct.

To test the accuracy of ProPEP, Frazier compared the results to kinetic based models using 77% AP /23% HTPB and 84% AP/16% HTPB at nearly 1 psi. Comparing the adiabatic flame temperature from each model was of particular interest[16]. These constituents, their amounts, and the pressure were chosen to be in line with flame temperature analysis conducted using (1) a kinetics model for premixed combustion of fine AP/HTPB composite propellant, and (2) a model used to determine flame structure and kinetics based on solving differential equations. The Jeppson model is specifically geared toward premixed combustion of monomodal, fine AP/HTPB propellants and takes into consideration combustion in three phases: solid phase, condensed phase region of mixed liquid and gas, and a premixed gas phase flame [3]. The second model, which will be called the –Korobeinichev Model, solves a set of differential equations which describe flow of a reacting, multi-component gas. This solution was done by taking thermal conductivity and diffusion into account, and also the kinetic mechanism containing 58 elementary reactions and 35 components obtained from previous research between the authors that studied kinetics in AP and HTPB composites [64].

Frazier provided a table of data generated by the PEP model which showed agreement with the data produced by two other models, but there are some potential discrepancies that should be clarified [16]. The ProPEP data show the flame temperature

being hotter than the other two models. This is most likely because the ProPEP runs were made using the R45M, or military-grade variant, of HTPB, which would result in a slightly higher temperature due to the increased amount of carbon and hydrogen in the chemical composition. Also, the flame temperatures did not match because of the extremely low pressure of the analysis (1 psi). Small changes in pressure for a propellant formulation tend to have little impact on the adiabatic flame temperature, but extreme pressure regimes can significantly enhance or reduce the flame temperature approximated by the ProPEP program due to pressure-dependent effects such as dissociation. At more-common pressures seen in our laboratory, for example 1000 psi, ProPEP calculates flame temperatures of 2731 K (for 84% AP) and 1998 K (for 77% AP).

4.1.2 Chemical Equilibrium Analysis (CEA) Code

ProPEP provides the total enthalpy and the mixture specific heat ratio, however what is needed is the sensible enthalpy corresponding to the energy being added to the system due to the difference in adiabatic flame temperature and the reference temperature of the combustion products and gas mixture. The mixture specific heat is calculated using the specific heat ratio and the ideal gas constant. Chemical equilibrium analysis (CEA) code utilizes NASA thermobuild to provide tables of thermodynamic properties for a user-supplied temperature schedule for each species. Using Equations 4–7, gas mixture approximations of the enthalpy and specific heat are found at all temperatures. Currently, NASA Glenn Research Center CEA code is implemented into

model predictions via an online tool located at: https://cearun.grc.nasa.gov/ [37]. However, the equations utilized by this online tool are capable of being built into any model structure if a thermochemical database of thousands of species is developed.

The specific heat value for each gas species of the burned propellant is found using a basic polynomial fit:

$$\frac{C_p^o}{R} = a_1\, T^{-2} + a_2\, T^{-1} + a_3 + a_4\, T + a_5 T^2 + a_6 T^3 + a_7 T^4 \qquad (4)$$

where R is the universal gas constant, and T is the temperature of the product species. Values for the coefficients, a_i, in Equation 4 are obtained from McBride et al., 2001.

To determine an overall gas mixture C_p using Equation 5, the specific heat of Argon (the inert, pressurization gas in the strand burner) must be known. According to Kee et al., 1990, Argon is an exception such that the polynomial reduces to a constant, a_1, which has a value of 2.50 for all temperatures up to 5000 K (because Argon is a monatomic gas) [65]. The specific heat for Argon is effectively treated as:

$$\frac{C_p}{R} = \frac{\gamma}{(\gamma - 1)} \qquad (5)$$

with a specific heat ratio of 1.67. Enthalpy is obtained by integrating $C_p°(T)$ and $C_p°(T)/T$ with respect to T and provides Equations 5 and 6.

$$\frac{H^o(T)}{RT} - \; -a_1 T^{-2} + a_2 \frac{Ln(T)}{T} + a_3 + a_4 \frac{T}{2} + a_5 \frac{T^2}{3} + a_6 \frac{T^3}{4} + a_7 \frac{T^4}{5} + \frac{b_1}{T} \qquad (6)$$

$$H^o(T) = \Delta H^o(298.15) + [H^o(T) - H^p(298.15)] \qquad (7)$$

Where the term *[H°(T) – H°(298.15)]* is the sensible enthalpy needed to be input into the model to assess how much energy the overall gas mixture is gaining due to the high temperature of the propellant combustion products.

According to McBride et al., most of the values of the coefficients used in Equations 6 and 7 were determined by a Least-Squares Fit. For gases, the temperature ranges for these fits are split into three fixed intervals: 200 to 1000 K (298.15 to 1000 K for ions), 1000 to 6000 K, and for some simple molecules, 6000 to 20,000 K [66]. The comparison of the properties evaluated using ProPEP values to the NASA CEA values for the R45M are provided in Table 1 for an 85% AP 15% HTPB propellant.

Table 1 Comparison of NASA CEA output to ProPEP propellant combustion code.

Propellant	Isp (s)	MW (g/mol)	Tad (K)	C*	γ
Baseline NASA	244	24.30	2810	4961	1.19
Baseline ProPEP	244	24.70	2831	4943	1.22

The values obtained from ProPEP are close to the values obtained with the NASA values. Noticeable differences come from the calculation of the molecular weight. ProPEP offers a wide range of HTPB variants and NASA only provides their HTPB properties. This is a rudimentary check, but it confirms that ProPEP is a sufficiently accurate application for the estimation of thermodynamics properties at equilibrium.

4.1.3 Combustion Efficiency From Pressure Rise

Combustion efficiency can be evaluated using thermodynamic properties of the constant-volume strand burner or closed bomb based on thermodynamic assumptions [67]. The burner is first assumed a quasi-closed system reducing the thermodynamic analysis to 2 states. State 1 is the pressure, temperature, and mass of the strand burner containing only the inert argon properties, then state 2 incorporates the changes in pressure, temperature, and mass of the system by adding the mass and temperature of the combustion products from the burned propellant. By assuming the combustion products reach thermal equilibrium with the argon gas (but with a frozen chemical composition), the final state can be readily calculated. Figure 13 illustrates how the control volume analysis was performed.

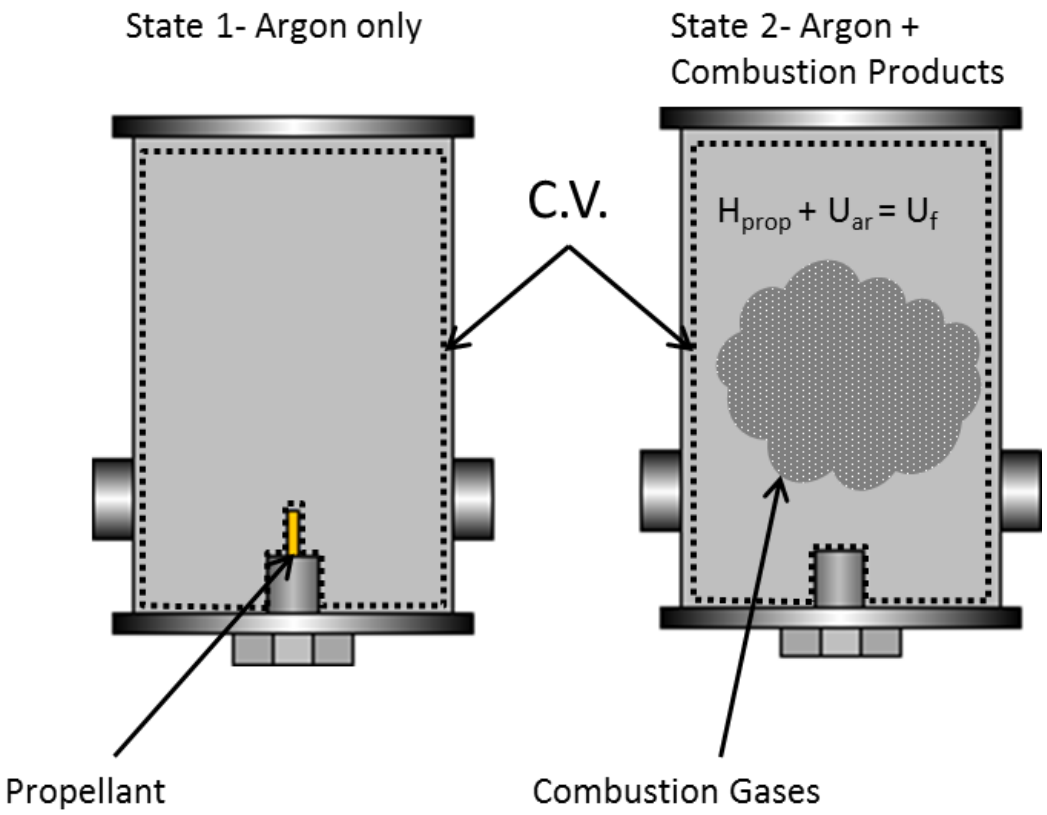

Figure 13 States for the thermodynamic equilibrium calculation assuming a single zone, where state 1 excludes the propellant and state 2 includes the products of combustion in the total mass of the system. The volume remains constant, but pressure and temperature change with the inclusion of the combustion products.

The mass of the propellant is recorded for every test and by determining the burning rate of the propellant using the pressure rise, the changes in pressure and mass of the system are known as a function of time. By starting with the closed-system energy conservation, a simple model for the burner can be established. No work was done on or by the system as the propellant flows into the control volume, but nothing leaves the vessel. By keeping the burning time of the propellant strand short enough, then the

pressure rise profile will be nearly linear with time. A linear pressure rise indicates that the losses due to heat transfer did not significantly impact the burning of the propellant or the temperature of the chamber gas mixture. Neglecting heat losses from the strand burner, the final, peak vessel temperature can be calculated using the relation in Equation (8).

$$T_f = \frac{C_{v,Ar} m_{Ar} T_{Ar} + C_{p,Prop} m_{Prop} T_{Prop}}{C_{v,mix}(m_{Ar} + m_{Prop})} \quad (8)$$

Using chemical equilibrium software such as PROPEP (Propellant Performance Evaluation Program), the adiabatic flame temperature and the mixture specific heat can be calculated. Calculating the mixture temperature leads to the final pressure using the ideal gas relation. Using the final, measured pressure of the gas mixture in the combustion chamber, a theoretical pressure rise P_f can be calculated (Eq. 9) and compared to this measured value.

$$P_f = \frac{(m_{Prop} + m_{Ar}) T R_{mix}}{V} \quad (9)$$

Modeling the pressure rise has presented difficulty in combustion vessels. For example, laminar flame speeds are studied using spherical bombs, often held at constant volume. Flame speed models incorporate pressure rise modeling to account for how the pressure alters the shape of the spherical flame inducing turbulence. The flame expands fast enough to push the unburnt gasses to the wall. The key issue reported is when the spherical flame touches the wall, the pressure drops rapidly. This phenomenon has been reported to rapid heat losses to the vessel wall. Immediately after the flame touches the

wall, the heat is transferred from the vessel resulting in rapid cooling of the flame and burnt gasses in the vessel [68-70].

At the elevated pressures of interest herein, real as effects could be important. Evaluation of the compressibility factor for the gas prior to combustion was performed to determine if ideal gas can be assumed. The compressibility was calculated at test pressures and room temperature for argon. Figure 14 shows the values for the compressibility factor for the main gas component, argon, over the pressure range tested. As seen in Fig. 14, the differences between real and ideal gases is less than 1%. Therefore, ideal gas was assumed for the calculations herein.

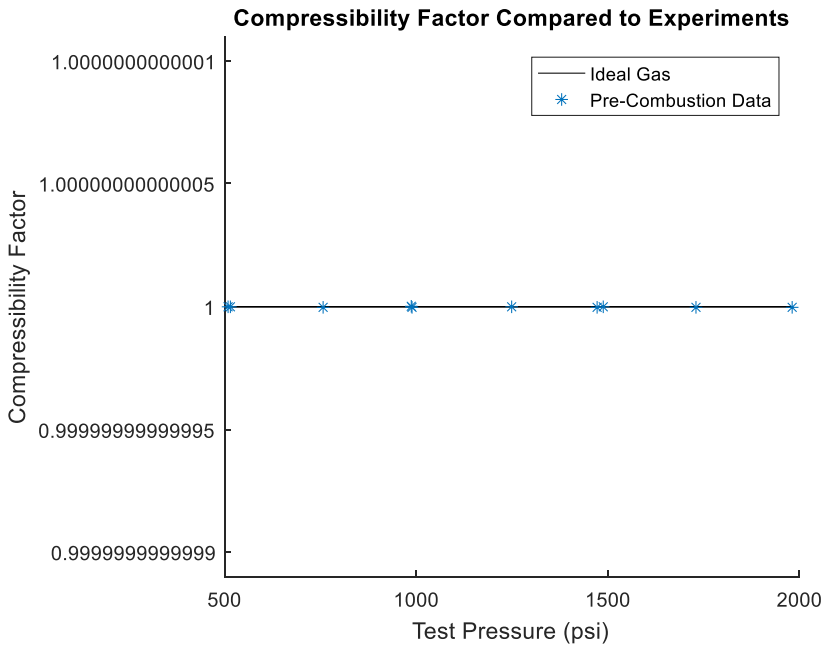

Figure 14 Compressibility factor in the strand burner prior to combustion.

A representative plot of the model compared to the data normalized by dividing by the mass of the propellant can be found in Figure 15, which gives a graph of peak pressure rise versus average chamber pressure. Each point on the plot represents an individual burn of that particular propellant mixture at that average pressure of that burn. The pressure rise data show a near-linear trend with increasing chamber pressure. However, in stark difference, the model predicts a higher pressure rise and nearly no pressure dependence. A problem therefore arises with such a model based on ideal mixing. The model was evaluated over the entire pressure range tested and the slope did not match the pressure rise from the baseline, as seen in Fig. 15. It was then identified that the adiabatic flame temperature of the propellant grain will not vary much with pressure. This trend implies that ideal mixing within a single zone does not capture all of the physics in the strand burner, particularly the pressure dependence.

Adiabatic flame temperatures for AP-based composite propellants are dependent primarily on the oxidizer-to-fuel ratio. For three sample oxidizer weight percentages (100, 85, and 80), the corresponding adiabatic flame temperatures are plotted as a function of test pressure in Figure 16. As seen in the figure, the flame temperature for a given AP percentage has very little variation with pressure. However, the absolute flame temperature varies significantly amongst the range in %AP shown, being about 1200 K for 100% AP and 2800 K for 85% AP. (The nonlinear effect of AP percentage seen in Fig. 16 is due to the stoichiometric level of AP being near 89%.) More importantly, when compared with the pressure-rise results in Fig. 15, the adiabatic flame temperature has a similar, flat slope as the mixture model prediction of the pressure rise, indicating

the dominant input in the single-zone mixture model was the adiabatic flame temperature for the propellant.

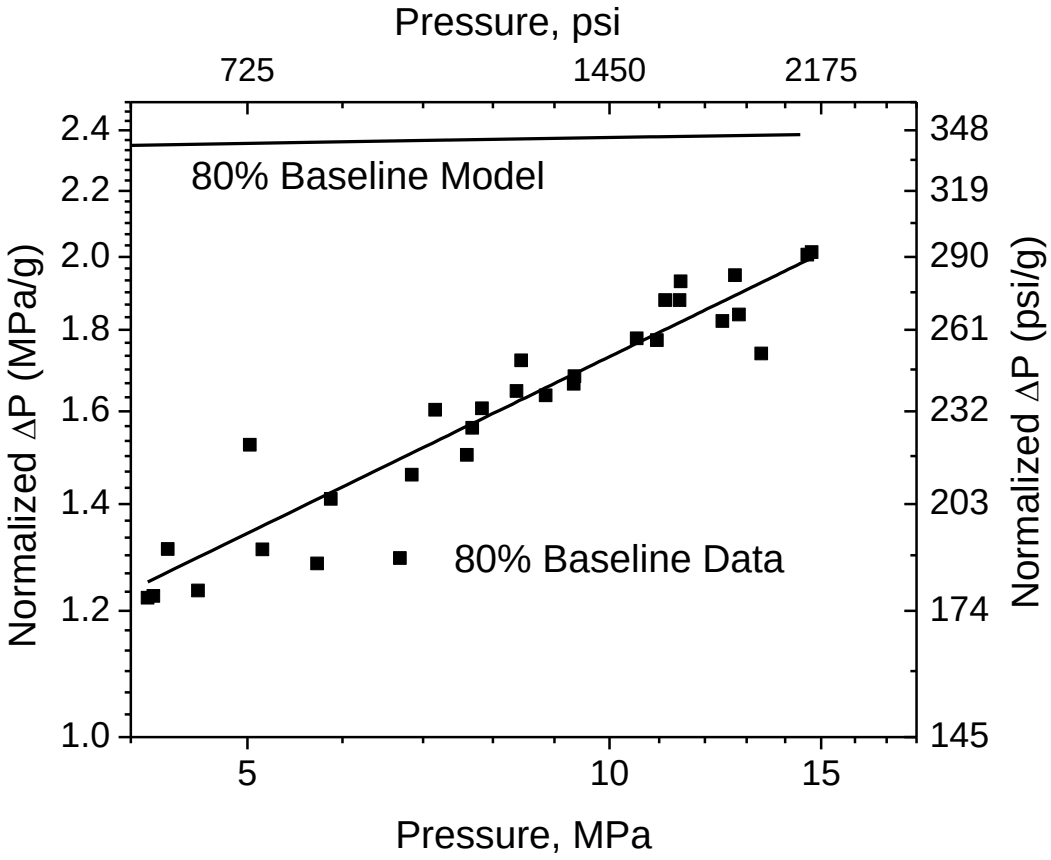

Figure 15 Mixture model compared to pressure rise over the entire test pressure range for a typical propellant.

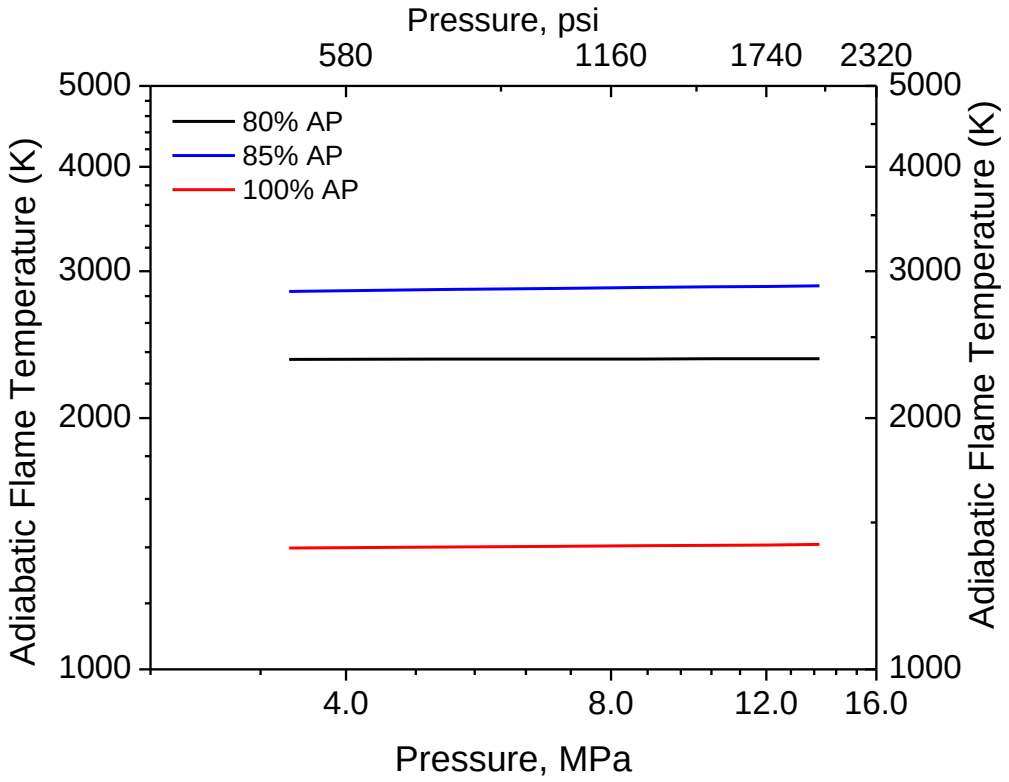

Figure 16 Adiabatic flame temperature change compared to test pressure for various mixtures of AP in HTPB.

The pressure resulting from a perfectly mixed system over predicted the pressure rise at low pressure and under predicted it at high pressures. While one would expect the ideal model to always over predict the pressure rise because it assume 100% combustion efficiency, the incorrect pressure dependence indicates that something is missing in the basic model. The opposite extreme of a 1-zone, perfectly mixed model is the scenario with no mixing between the product gases and the inert, pressurizing gas. This scenario is equivalent to the assumption that the propellant burns quickly enough so that the combustion gases push on the argon (i.e., the inert, pressurizing gas) with no mixing. The result would then be a two-volume model where the combustion gases have pushed

on the argon and compressed the argon like a piston. The propellant volume is then at adiabatic flame temperatures but at the same pressure as the argon-filled volume. To separate the volumes, an imaginary piston is held in place keeping the argon at room temperature and the initial test pressure. Then, to equilibrate, the piston is allowed to move and the propellant gas expands, compressing the argon. Work from the piston moving causes the internal energy of the argon to increase and the propellant gas to decrease. This boundary work reduces the final temperature or the propellant gas, but increases the temperature of the argon. The final pressure is found when the volumes equilibrate at the same pressure. A control volume schematic is shown in Figure 17. State 1 has combustion gasses at very high pressure at adiabatic flame temperatures and argon at room temperature. To equilibrate, the piston is allow to move and compress the argon. State 2 is the final pressure of the Argon.

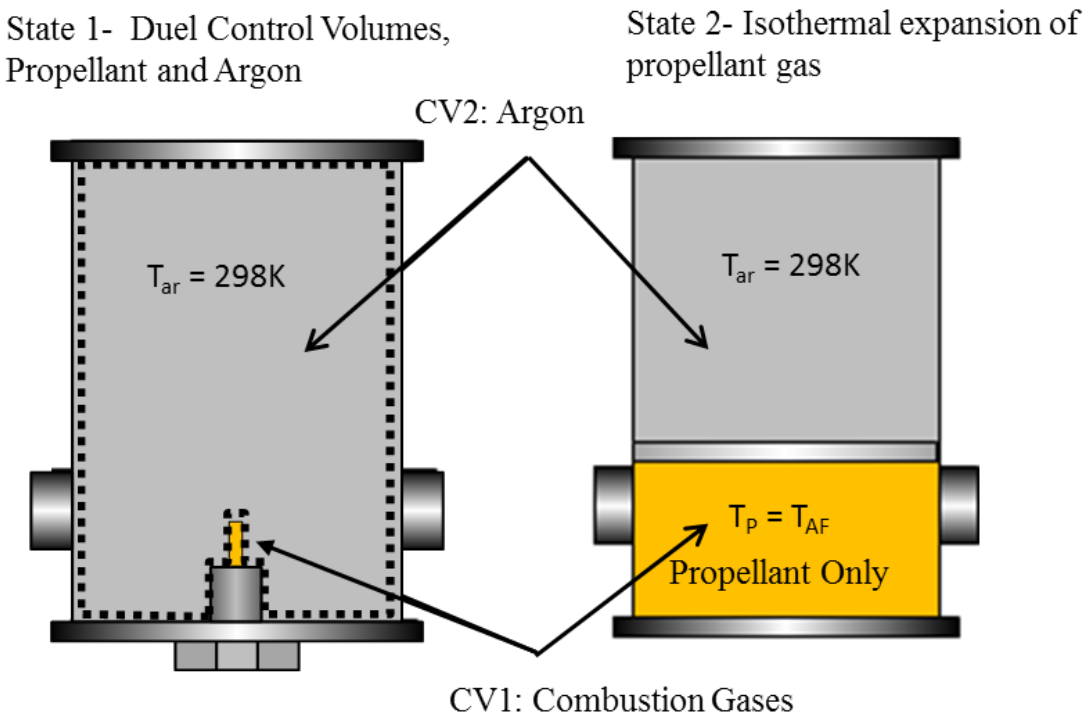

Figure 17 2-volume states for the thermodynamic equilibrium calculation from state 1 to state 2.

By using a moving piston system, there is a smaller volume of hot gases. Equilibrating the pressure of the two volumes without heat loss captures the pressure dependence on the pressure rise that did not exist with the perfectly mixed, single-zone model. The change if volume is calculated using the ideal gas equation for both sides of the piston at an equilibrated pressure, resulting in equation 10.

$$\Delta V = \frac{V_{Ar,i} \cdot \mu - V_{p,i}}{\mu + 1} \tag{10a}$$

where the value for μ is calculated by,

$$\mu = \frac{(mTR)_p}{(mTR)_{Ar}} \tag{10b}$$

A comparison of how the two volumes change over the pressure range can be found in Figure 18. Note that the propellant gases are only a small portion of the overall volume. The results from the 2-volume model improved on the slope of the pressure rise per gram of propellant to better match the measured data. Figure 19 plots a comparison of the two different models for the same typical propellant mixture used above for the 1-zone model predictions. From this plot, the 2-volume model is now able to capture how the change in peak pressure varies with the average chamber pressure. This improved result is in contrast to the rather flat prediction of the 1-volume model. In fact, the level of peak pressure and the slope from the 2-volume model are rather close to, but not perfectly, the measured values. By solving the conservation of energy equation, additional heating was supplied by boundary work of the expanding volume. Further differences between the improved model and the experimental data could be due to effects of heat transfer and inter-volume mixing, which are not present in the simple model.

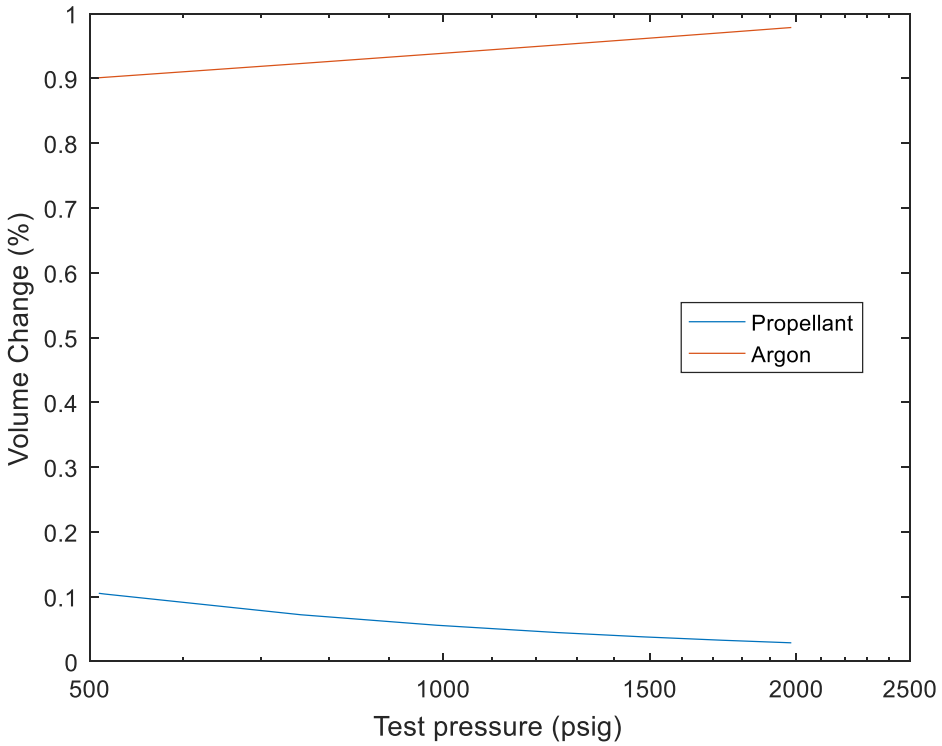

Figure 18 Volume percentage of the argon and propellant gases over the test pressure range.

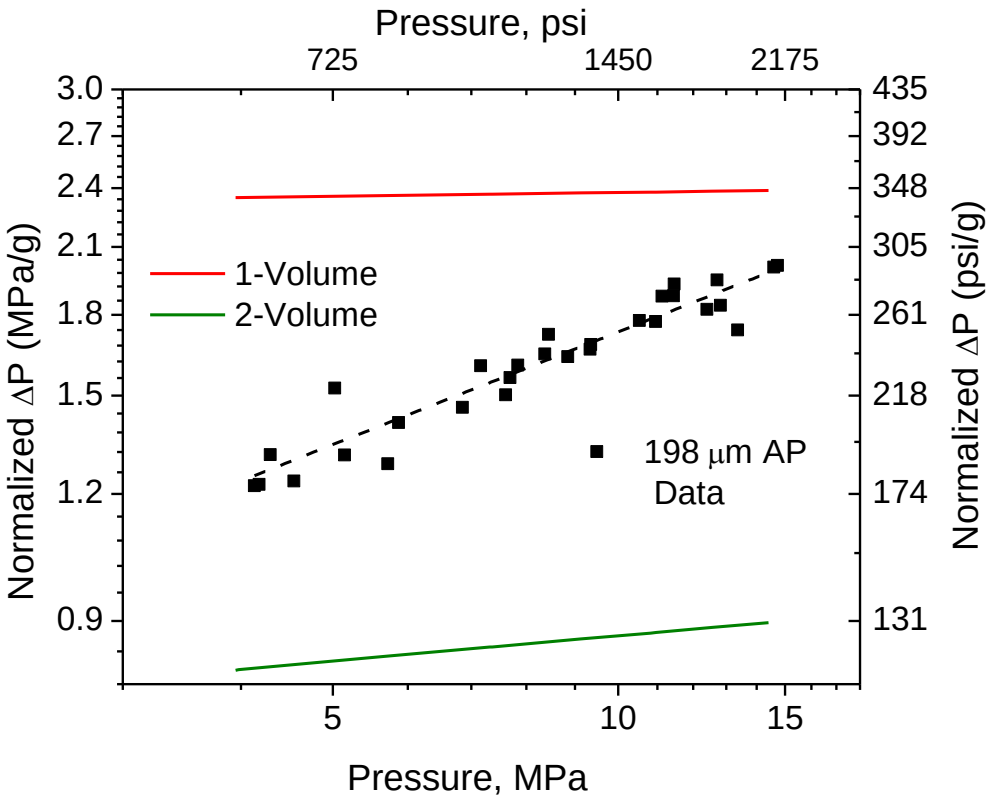

Figure 19 Comparison of the 1-volume mixture model (as used by Frazier [16, 39]) and the new 2-Volume model to the data for a typical AP/HTPB propellant with 80% AP.

A normalized pressure rise can be used to indicate the completeness of combustion; a larger pressure rise would indicate higher combustion temperatures or more solid mass converted to gas. Pressure rise was normalized using propellant mass; normalizing by mass provides information on the pressure rise per gram of propellant, which should even out any sample-to-sample variations in mass. Propellant strands utilized herein are all at the same diameter of 0.48 cm (0.1875 in); subsequently, the mass is proportional to the length of each strand. As mentioned above, closed-bomb

burners are widely used and modeled for the testing of composite solid propellants [33, 38]. The pressure increases due to the temperature increase from combustion and can be used an indicator of increased chemical c*. The effective exhaust velocity of the propellant is altered by the specific heat ratio, γ, gas temperature, T, and molecular weight of the mixture [2]. The thought is that the increased pressure rise is an indication of increased chemical efficiency. A higher pressure rise in the strand burner experiment should therefore indicate a higher combustion temperature. The influence of the product gas temperature on the overall chamber pressure is reflected to first order by the thermodynamic model described in the preceding paragraphs. By utilizing the ideal gas relation of the product gas mixture, changes in c* can be inferred from the measured pressure increase (due to the increased product gas temperature) as in Eq. (11).

$$c^* = \frac{\sqrt{\gamma R T_{ad}}}{\gamma \sqrt{\left[\frac{2}{\gamma+1}\right]^{\frac{\gamma+1}{\gamma-1}}}} \tag{11}$$

Knowing the impact on the c* value for different propellant additives provides information on the gain in performance of the propellant as defined in the specific impulse (I_{sp}). Strand burner experiments are inexpensive compared to motor testing, and using the pressure rise as a performance indicator is valuable when evaluating an additive's effect on the propellant combustion efficiency in addition to the commonly measured burning rate. This connection between measured pressure rise and c* efficiency is further explored later in this chapter.

4.2 Combustion Model Alterations due to Mixing and Temperature Change

Adding mixing to the model could further correct the slope on a pressure rise-versus-average pressure plot, to obtain better agreement between the model predictions and the empirical data. Incorporating mixing into the 2-volume model was done by taking a portion of the initial argon and allowing it to cross the boundary. Then the product mixture composition would be calculated using ideal mixing equations, similar to the Frazier model. By mixing the argon with the combustion gases in this manner, the initial 2-volume temperature and pressure would be reduced. This approach solves the conservation of energy equation in tandem with the ideal gas equation in the mixture volume. A diagram of the mixing can be found in Figure 20. State 1 allows a mass fraction argon (symbolized as Y) to mix with the propellant combustion gasses at very high pressure and temperatures. The remaining argon is at room temperature and test pressure. State 2 is the final equilibrated pressure of the Argon. Similar results were calculated if the propellant mass crosses the boundary and mixes with the argon. Values of the final mixing would require higher percentages of the propellant gas to mix with the argon.

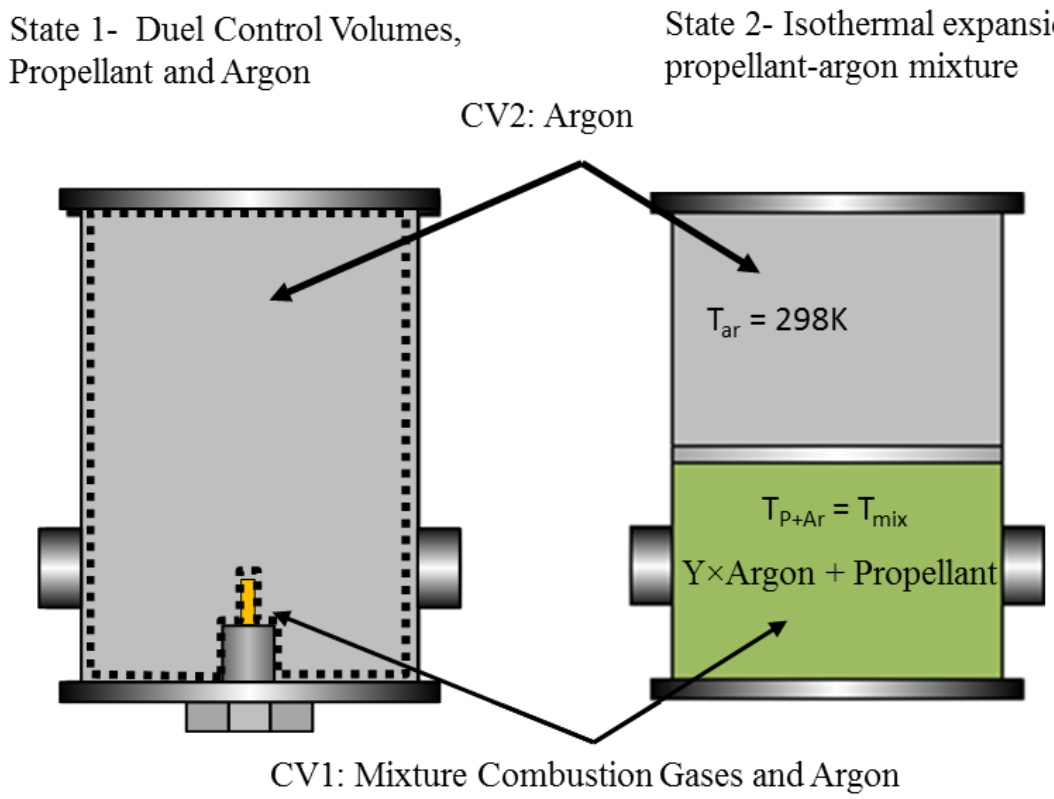

Figure 20 2-volume states for the thermodynamic equilibrium calculation with the inclusion of mixing for both state 1 and 2.

In an effort to estimate the levels of mixing in the chamber, simple Fickian diffusion was used to determine the flame height. To determine the appropriate molecules for diffusion, the composition of the exhaust gases was examined. Table 2 shows the composition of the exhaust as determined by ProPEP software.

Table 2 Product species for an 80% baseline propellant at 500 psi.

Species	Moles	Mole Fraction (%)	Mass (g)	Mass Fraction (%)
CO	8.56×10^{-3}	26.4	2.40×10^{-1}	38.6
N2	2.47×10^{-3}	7.6	6.92×10^{-2}	11.1
HO	5.73×10^{-6}	0.0	9.74×10^{-5}	0.0
CHO	5.06×10^{-8}	0.0	1.47×10^{-6}	0.0
O	1.63×10^{-8}	0.0	2.61×10^{-7}	0.0
H2O	7.71×10^{-3}	23.8	1.39×10^{-1}	22.4
CO2	1.62×10^{-3}	5.0	7.13×10^{-2}	11.5
NH3	4.16×10^{-7}	0.0	7.07×10^{-6}	0.0
Cl2	4.67×10^{-8}	0.0	1.59×10^{-6}	0.0
CNHO	9.03×10^{-9}	0.0	3.88×10^{-7}	0.0
H2	7.15×10^{-3}	22.1	1.43×10^{-2}	2.3
H	3.06×10^{-5}	0.1	3.06×10^{-5}	0.0
NO	1.88×10^{-7}	0.0	5.64×10^{-6}	0.0
CH2O	4.04×10^{-8}	0.0	1.21×10^{-6}	0.0
O2	7.34×10^{-9}	0.0	2.35×10^{-7}	0.0
HCl	4.82×10^{-3}	14.9	8.68×10^{-6}	14.0
Cl	1.47×10^{-5}	0.0	2.50×10^{-4}	0.0
CNH	6.15×10^{-8}	0.0	1.66×10^{-6}	0.0
COCl	3.41×10^{-8}	0.	1.53×10^{-6}	0.0

CO_2 diffusion was chosen because of the relatively high mass percentage of it in the products and the simpler calculation. A one-film diffusion of CO_2 into N_2 model was used to estimate the diffusion coefficient for the two gases. The CO_2 was assumed to be at adiabatic flame temperature and the N_2 at room temperature. Using the test pressure for an 80% monomodal baseline test, the number of moles of CO_2 and N_2 are known. Using the molar ratio information, the mass flow rate of the CO_2 was calculated based on the diffusion coefficients [63, 71]. The diffusion penetration distance was calculated using Eq. 12 and is found in Figure 21.

$$L = \frac{\dot{m}_{co_2} t}{\rho \pi r_s} \tag{12}$$

where ρ is the mixture density, t is the burning time, r_s is the radius of the propellant sample, and m_{co2} is the mass flow rate to of the CO_2.

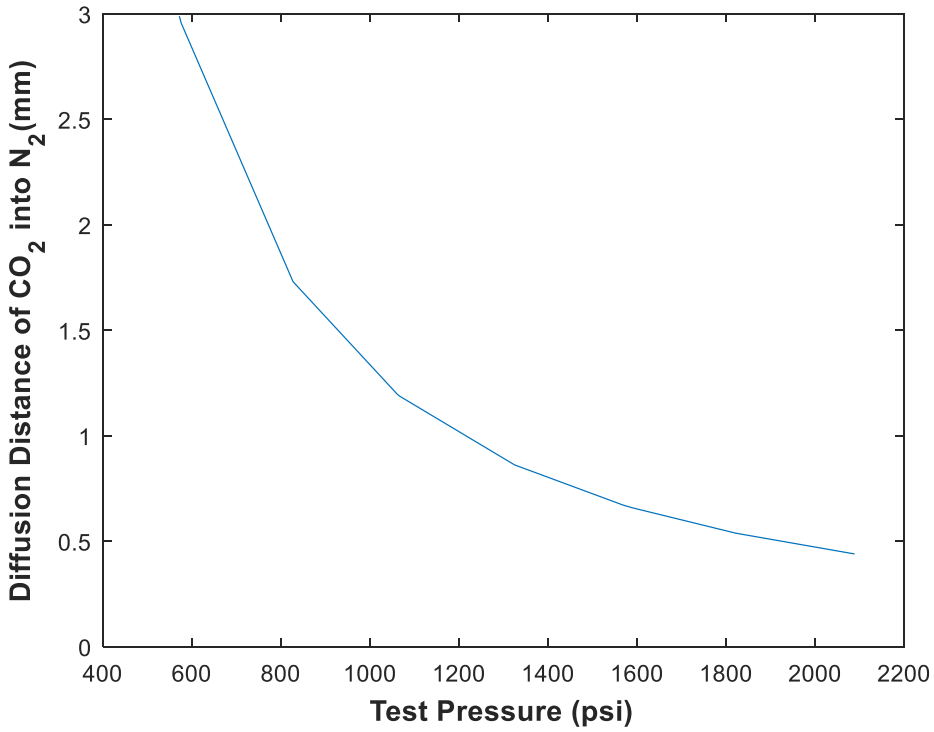

Figure 21 CO_2 diffusion depth into N_2 over the test pressure range based on the production of CO_2 from an 80% monomodal AP baseline propellant.

The penetration distance of CO_2 was calculated to go from 8 cm at 600 psi to approximately 4.5 cm at 2100 psi. Mixing length was found to decrease with pressure, meaning that the flame is pushed closer to the propellant surface at higher pressures. This result is consistent with literature findings [44, 72, 73].

Incorporating mixing was done by evaluating several mixture ratios, starting from no mixing and increasing up to complete mixing. The 100% mixing case should look just like the model developed by Frazier, i.e. the 1-volume model. Slope matching was done to match the mixture ratio that best simulated the slope produced by the experiments. It was found that 30% argon mixing (or 90% of the propellant mixing in the all of the argon) produced the magnitude, which exactly matched the magnitude in the data at higher pressures. The diffusion height was used to determine if the mixing was viable. Diffusion estimated that the propellant would travel only a small portion of the vessel, which could allow for small amounts of mixing. Model predictions for mixing 30% argon in the piston volume or 90% of the propellant mass mixing with the argon is plotted in Figure 22.

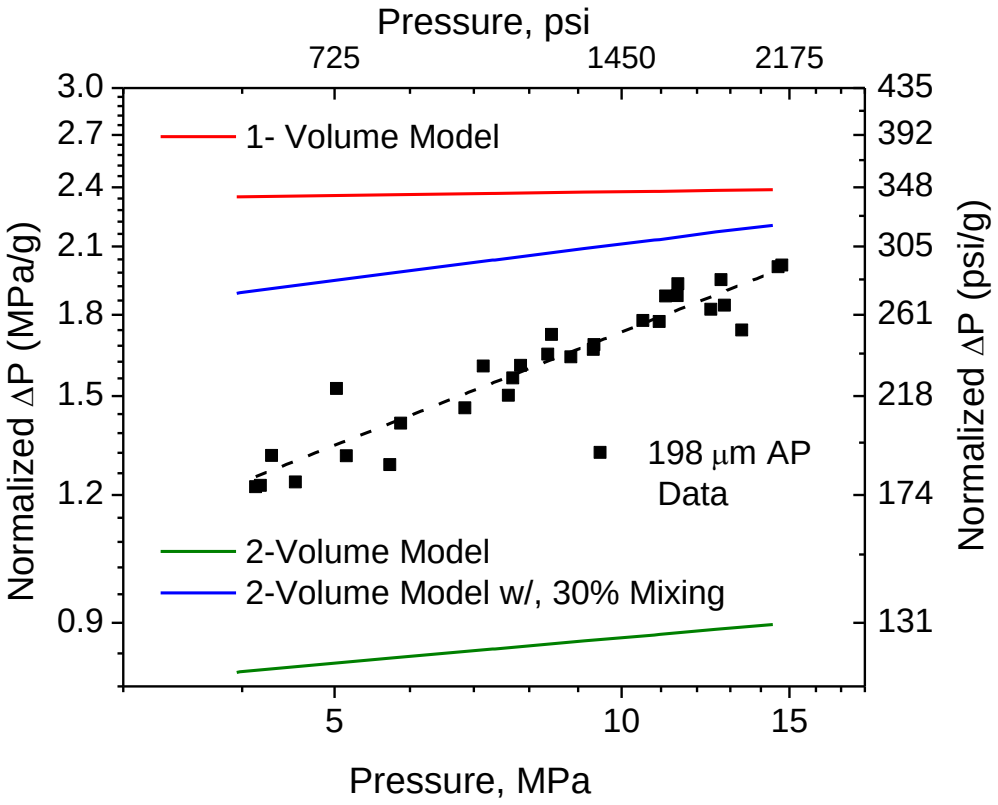

Figure 22 Model corrections incorporating a single amount of mixing from a diffusion calculation.

Incorporating mixing caused the model to increase the normalized pressure rise. This increase can be attributed to the increased volume of higher temperature, which pushes the magnitude of the pressure increase. A simple heat transfer calculation did not lower the temperature enough to push the model onto the data. It is thought that there are kinetic parameters that were not captured in the simple model. Since the goal of this study was not to produce a fully functional model, but to use simple thermodynamic relationships to estimate the pressure rise, a correction factor was added to account for the variable mixing parameters. A few of the parameters not modeled include kinetic

models, phase change, phase interactions, diffusion of solids and liquids, and other unknown physics. The correction varies the mixing ratio of the argon from 10% to 30% with the propellant (50% to 90% of the propellant mixing with the argon) and the results can be found in Figure 23. Note that the corrected model now has the same trend as seen in the data, and that it also has a higher pressure rise than the data. This latter observation is due to the fact that the simple model assumes that the product gas temperature is at the theoretical maximum level, i.e. the value from 100% combustion efficiency. The experimental data shown with the AP particle size near 200 microns takes into account the incomplete combustion that is due to the larger particle sizes. One would expect that smaller particle sizes to approach the results of a premixed system propellant system as assume in the theoretical adiabatic flame temperature calculation.

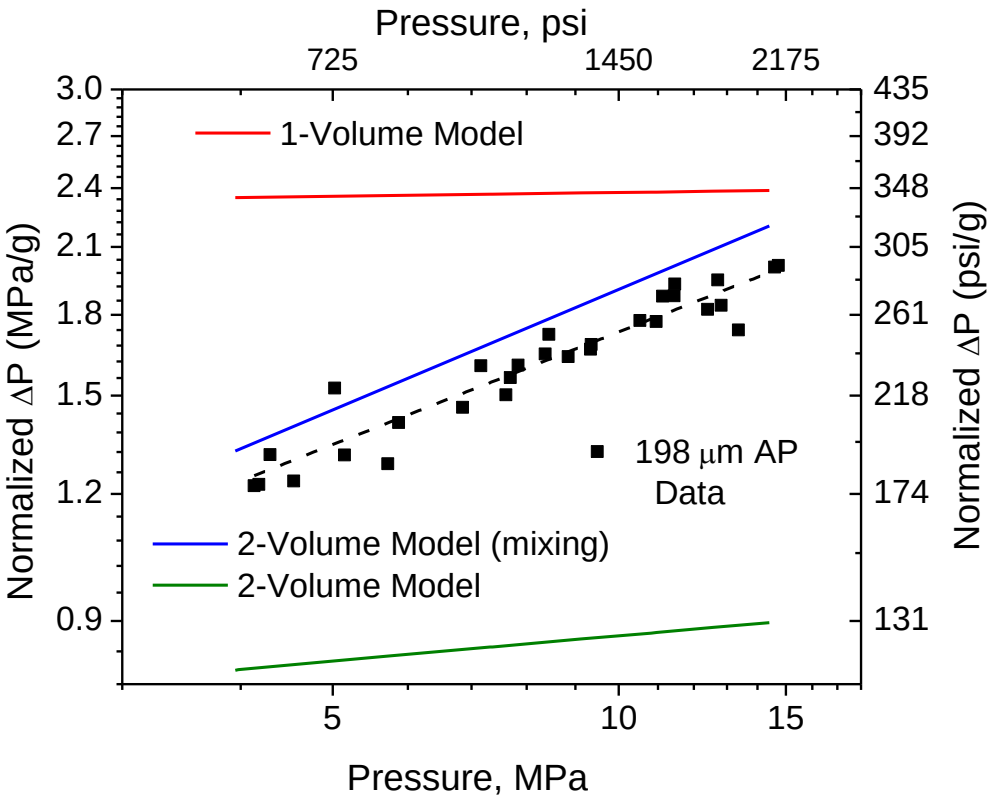

Figure 23 Model after applying the variable mixing correction to the pressure rise.

4.3 Efficiency Assessment Using the Model

Using the previously described model with the correction coefficient, the flame temperature in the propellant volume was changed to evaluate whether a temperature change would have a noticeable impact on the chamber pressure rise; if so, what kinds of temperature differences (i.e., c* changes) correspond to the typical pressure increases seen in the experiment. In other words, by changing the flame temperature, the model could be used to indicate the approximate change in the c* efficiency between similar propellant formulations. Changes to the propellant flame temperature in the propellant

volume simulate the reduced flame temperature for non-ideal combustion. Figure 24 shows the results of increasing the adiabatic flame temperature by 200 K and decreasing the adiabatic flame temperature of the propellant by 50 K and 200 K. The values for the temperature decrease were chosen based on how they matched with the data discussed in Chapter VI.

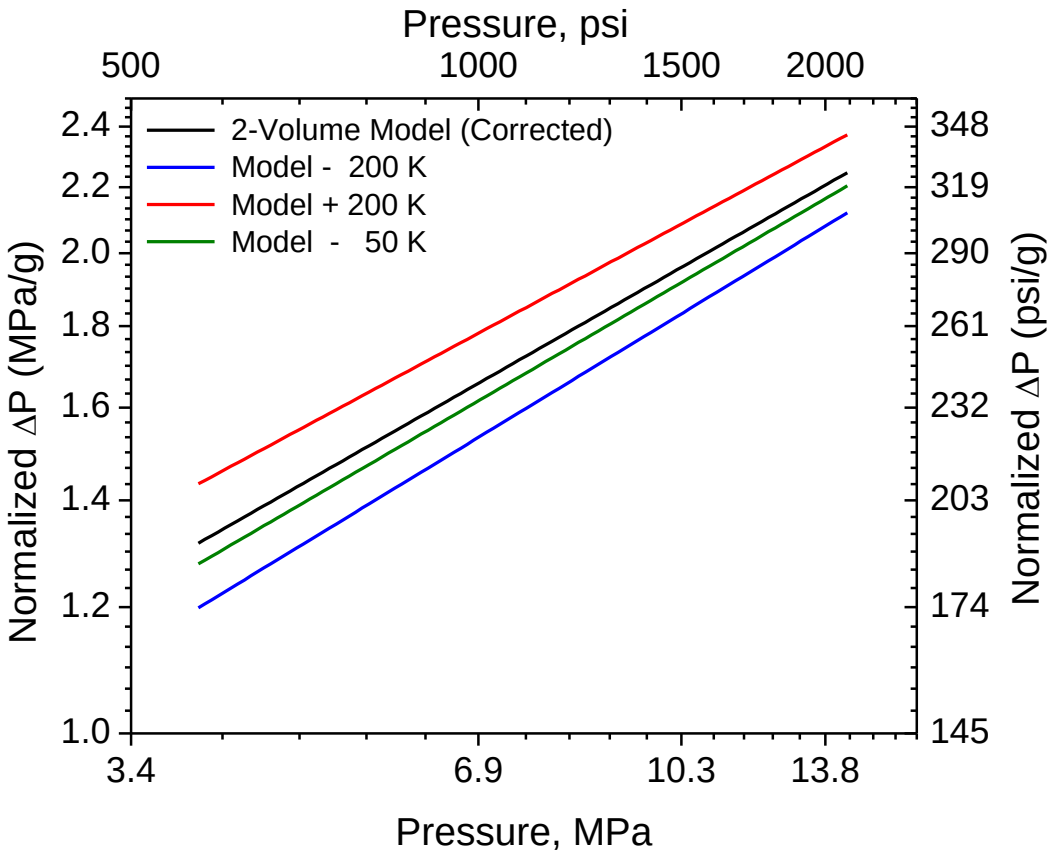

Figure 24 Model with set temperature changes to test what temperatures produce a noticeable difference in pressure increase, based on a AP/HTPB propellant with 80% AP by mass.

Using the model to alter the flame temperature until the model match with the data collected for the 200 μm AP size. Then additional raising or lowering the flame temperature in the model output was used to evaluated the temperature changes for other AP sizes. Changes in the flame temperature in the model are used to calculate the normalized pressure rise and compared to data. Comparing the modeled pressure rise change of the same propellant with various AP sizes revealed that there is noticeable temperature changes. Using the temperature changes, a relative c* can be calculated for the each AP size. Typically solid propellant will have a c* efficiencies between 85 to 95% depending on the quantity of aluminum in the propellant [74]. While the temperature change can be approximated, there could be other reasons for the increased pressure. A major change could be from an increased conversion of solid to gas. Combustion would be more efficient because of the reduced soot production. The main goal of this thesis was to establish a method to evaluate the combustion efficiency of similar propellants using a constant-pressure strand burner. More evaluation will be discussed in Chapter 6 with the direct comparison to the data.

CHAPTER V

IGNITION MODEL VALIDATION

Numerous models have been developed for the prediction of ignition delay times of premixed gas-phase propellants using chemical kinetic mechanisms. Modeling of solid propellant ignition is considerably more complicated and must take into account several physical phenomena ranging from heat transfer and phase changes to heterogeneous chemical kinetics. A simple model to determine the ignition of a solid propellant strand via laser irradiation was created herein using a 2D transient conduction model. Applying a radiation heat flux boundary condition on the top surface of a cylinder, the temperature profile in the cylinder was calculated for different time intervals. The ignition time was determined when the sample reaches the ignition temperature of the propellant mixture; to more accurately obtain the ignition temperature, a node below the top surface was monitored [40]. For this study, the node taken was at a depth of 20 micrometers, or about one-fifth of an average AP particle size.

The intent of the simple model was to determine if the experimental results collected were consistent with the physics of heat transfer and to verify the laser power calculations. In this way, any observed ignition time trends from a given set of tests that deviate from the trend predicted from the simple conduction model could then be attributed to gas-phase chemical kinetic or catalytic effects. The details of the first-order ignition model are provided in this chapter.

5.1 Thermal Properties

Properties of the propellant mixture were calculated using values developed for kinetics models from several groups for AP, HTPB, and Al. The mixture values were then calculated by summing the contributions of each ingredient on a percent mass basis. However, the thermodynamic properties were taken at an average temperature and are assumed to be constant as the sample was heated, and the model does not incorporate any phase change. Thermodynamic properties for AP as found in Jeppson's model are identical to those used by Jing, and HTPB properties used herein were taken from the Jeppson model (as seen in Tables 3 and 4 [3, 75]).

Table 3 HTPB properties used in the Jeppson [3] AP/HTPB model.

Chemical Structure	$(C_4H_6)_{40}(OH)_2$		
$\Delta H\_f,298$, [76], [kcal/mol]	-170		
Molecular Weight [77], [g/mol]	1212		
Phase	Solid(< 523K)	Liquid (> 523K)	
Density [78], [g/cm^3]	0.88	0.88	
ΔH_{tr}, [kcal/mol]	-	2	
Heat capacity [79], [cal/g/K]	$C_p(T[K]) = 0.25 + 0.85\times10^{-3}\,T$		(T < 523)
	$C_p(T[K]) = 0.19 + 0.62\times10^{-3}\,T$		(T > 523)
Thermal conductivity [78], [cal/cm/K/s]	$\lambda(T[K]) = 4.4\times10^{-4} + 1.3\times10^{-7}\,T$		

Table 4 AP properties used in the Jing [75] AP model.

Chemical Structure	NH_4ClO_4		
$\Delta H\_f,298,[76]$, [kcal/mol]	-70.7		
Molecular Weight [77], [g/mol]	117.5		
Phase	Orthorhombic	Cubic	Liquid (> 523K)
Density [78], [g/cm^3]	-	-	1.76
ΔH_{tr}, [kcal/mol]	-	2.5	7.0
Heat capacity [78], [cal/g/K]	$C_p(T[K]) = 0.14 + 0.41\times10^{-3}\,T$		$(T < 523)$
	$C_p(T[K]) = 0.16 + 0.41\times10^{-3}\,T$		$(513 < T < 815)$
	$C_p(T[K]) = 0.49$		$(T > 815)$
Thermal conductivity [78], [cal/cm/K/s]	$\lambda(T[K]) = 9.95\times10^{-4} + 3.75\times10^{-7}\,T$		

Thermal properties were also determined by using a mass ratio of the individual ingredients, and the resulting values were used in the simulations. The properties of aluminum are introduced here because transient ignition predictions for an AP/HTPB/Al propellant are included in the presented results of the current work, in Chapter 7. Aluminum being a significant fraction of the mass resulted in a large increase in thermal conductivity of the propellant. Thus, the thermal properties for aluminum were important to model the heat transfer, and they are found in Table 5.

Table 5 Aluminum properties used by Tanner [80] and the current AP/HTPB model.

Chemical Structure	Al		
$\Delta H_{f,298}$, [kcal/mol]	0		
Molecular Weight [g/mol]	26.98		
Phase	Solid(< 523K)	Liquid (> 523K)	
Density [g/cm^3]	2.7745	2.5546	
ΔH_{tr}, [kcal/mol]	-	2.5583	
Heat capacity, [cal/g/K]	$C_p(T[K]) = 0.144 + 1.58\times10^{-4}\,T$		(T < 933)
	$C_p(T[K]) = 0.281$		(T >933)
Thermal conductivity , [cal/cm/K/s]	$\lambda(T[K]) = 0.651 - 1.62\times10^{-4}\,T$		

The model calculation for the addition of titania and iron oxide were calculated using the mass ratio approach. It was determined that the thermal properties were not altered significantly by the presence of the rather small levels of such additives (typically < 1% by mass), and there was no variation for either additive. The calculated values can be found in Table 6.

Table 6 Thermal properties calculated using the mass ratio for 80% monomodal and aluminized propellants.

Thermal Properties	ρ_prop (g/cm^3)	c_p (J/kg-K) $\times 10^6$	α (m^2/s) $\times 10^{-10}$	k (W/m-K)
Baseline 1	1.63	1.36	1.85	0.41
Propellant w/ TiO_2	1.63	1.36	1.85	0.43
Propellant w/ Fe_2O_3	1.63	1.36	1.85	0.43
Aluminized Baseline	1.67	1.27	2.22	47.12
Aluminized w/ TiO_2	1.67	1.27	2.22	47.14
Aluminized w/ Fe_2O_3	1.67	1.27	2.22	47.14

5.2 Modeling Conduction With a Heat Flux Boundary Condition

To validate the results obtained from experiments, a simple heat conduction model was formulated. Modeling was performed on the well-known, transient 2D conduction model of a semi-infinite cylinder. The boundary condition at the top was given as radiative heating using a prescribed heat flux, while the sides are insulated. At the bottom of the cylindrical strand, the boundary condition was a constant temperature. A temperature profile near the top surface was used to determine the time until ignition. Figure 25 provides a diagram of how the heat transfer was modeled in this study.

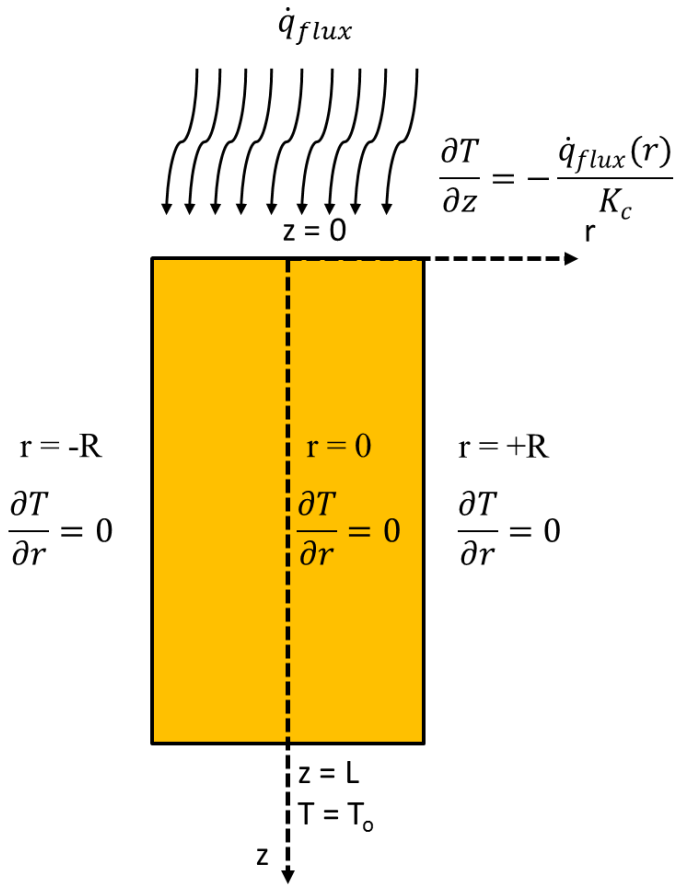

Figure 25 Radiant heat transfer diagram.

Starting with the 2D transient conduction equation in cylindrical coordinates, the temperature distribution of the strand is calculated using Eq. 13. Using a finite difference numerical scheme to solve the second-order, transient partial differential equation resulted in Eq. (14) to solve for the interior nodes [71].

$$\left.\frac{\partial T}{\partial t}\right|_{r_i,z_j} = \frac{\alpha}{r_i}\left(\frac{T(r_{i+1},z_j) - T(r_{i-1},z_j)}{2\Delta r}\right) + \alpha\left(\frac{T(r_{i-1},z_j) - 2T(r_i,z_j) + T(r_{i+1},z_j)}{\Delta r^2}\right) + \alpha\left(\frac{T(r_i,z_{j-1}) - 2T(r_i,z_j) + T(r_i,z_{j+1})}{\Delta z^2}\right) \quad (13)$$

The entire strand was assumed to be at ambient temperature (T_o = 22 ^oC) at initial time (t =0). The first boundary condition was assigned to the top surface such that the front plane subject to laser radiation was modeled as a surface subject to a Gaussian distributed heat flux. Adiabatic conditions were assumed on the outer radius and back plane of the strand such that

z = 0 $$\frac{\partial T}{\partial z} = -\frac{\dot{q}_{flux}(r)}{K_c} \quad (14a)$$

z = L $$T = constant \quad (14b)$$

r = 0, R $$\frac{\partial T}{\partial r} = 0 \quad (14c)$$

Typically, the output of a CO_2 laser follows Gaussian beam optics, and thus the model incorporated a Gaussian distribution of power with the center of the beam being the location of the greatest intensity. To accurately capture the heat flux boundary condition of the laser, a Gaussian profile was used to model the flux term given in Eq. 14.

$$\dot{q}_{flux} = \frac{I_o\,\alpha_{rad}}{\sqrt{2\pi\sigma^2}}\exp\left(-\frac{r^2}{2\sigma^2}\right) \quad (14)$$

The characteristic radius, σ, is given a value that closely resembles the values from experiments (that is, 1.0 mm). The absorption coefficient, α_{rad}, was set to a

literature value of 0.71, and a laser intensity of 60 W was used to mimic the experiments [80]

5.3 Modeling Calculations

The model uses a grid of 40-by-40 to calculate the temperature profile of a 2.54 cm long strand, but the model focuses the grid only on the portion of the strand which has an observable temperature change. Thus, the grid was placed on the top millimeter of the propellant strand, i.e. for $z = 0$ to 1 mm. Ignition was found when the temperature of the node at 20 microns was equal to 640 K based on the BDP model [73]. The temperature profiles for non-aluminized and aluminized propellants at the time of ignition are given in Figure 26 and Figure 27, respectively.

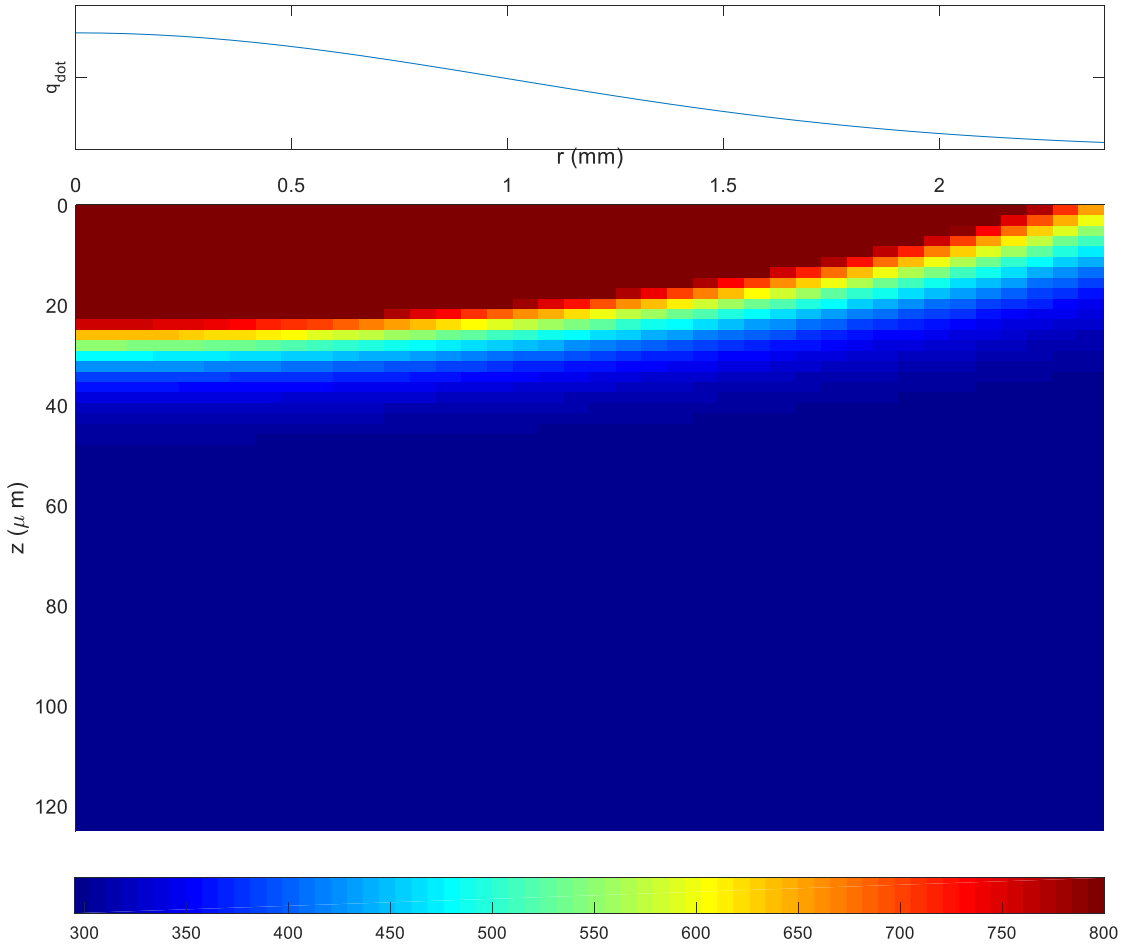

Figure 26 Temperature Profile of a non-aluminized propellant strand at approximately 667.1 ms. Thermal penetration is approximately 25 micrometers.

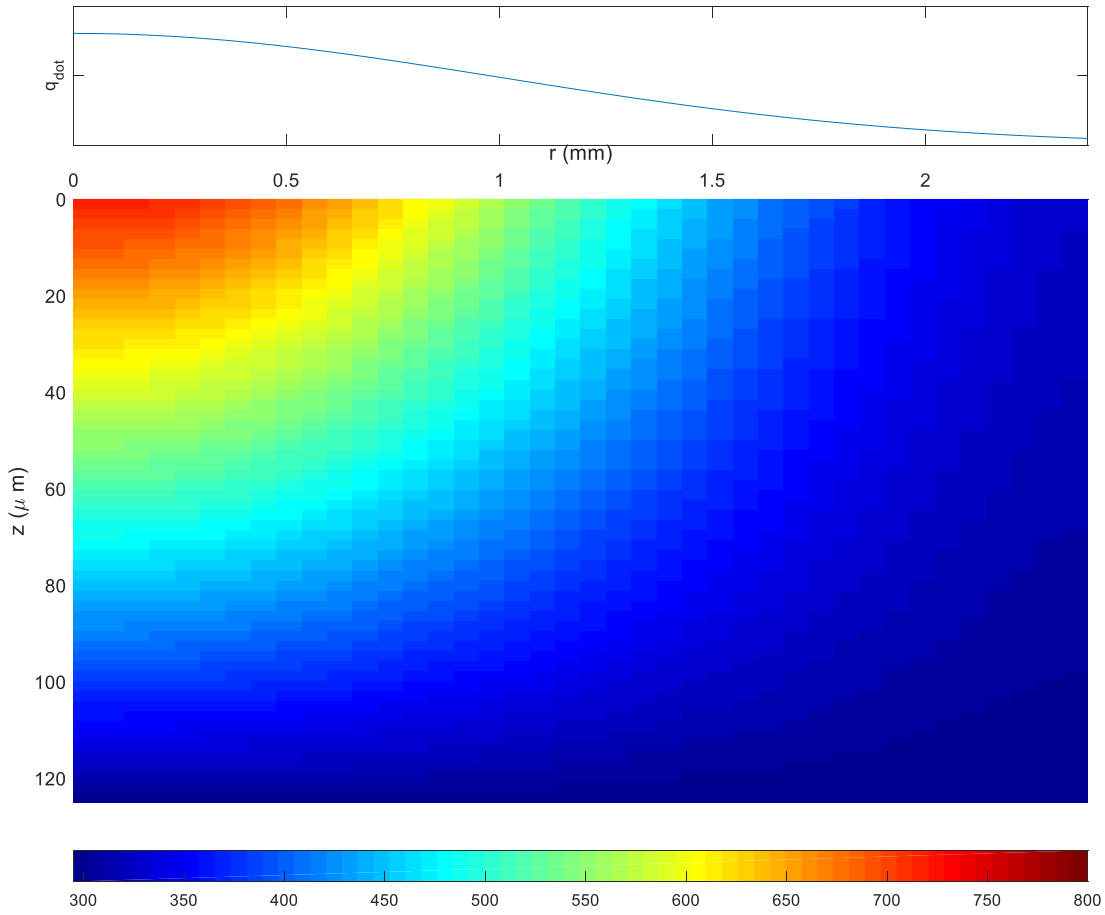

Figure 27 Temperature Profile of aluminized propellant strand at approximately 921.1 ms. Thermal penetration is approximately 25 micrometers.

The non-aluminized propellant ignited at 667 ms, and the aluminized formulation ignition occurred at 921 ms. The longer ignition time for the aluminized formulation is therefore observed to be from the loss of heat from the surface due to conduction. Aluminum has a higher thermal conductivity than the AP/HTPB composite, and the heat was then able to penetrate further into the sample. When the additives at a 0.3% by mass were added into the calculation, the thermal properties did not vary significantly as

mentioned above. The fact that the small quantity of additive does not alter the thermal conductivity would imply then that any differences in the ignition delay time between additive-containing samples and baseline ones can be attributed to the additives aiding in the ignition process by altering the AP decomposition. Results of the ignition time experiments are provided in Chapter VII.

CHAPTER VI

SOLID PROPELLANT PERFORMANCE

Composite solid propellants are commonly used for rocket boosters and missiles due to the simplicity in their design. However, modeling propellant combustion relies on experimental data. Additive synthesis techniques have altered how catalysts aid in the decomposition of the propellant. The present study focused on evaluating performance characteristics of AP/HTPB solid propellants, mainly through ignition delay times and combustion efficiency from the pressure rise. This chapter summarizes the results obtained for the performance evaluation using the measured pressure increase in burning rate tests, and a table of propellants tested to evaluate the pressure rise is given in. Most of the propellant burning rate data were taken from other studies, but the data was re-analyzed to evaluate the combustion efficiency found in Table 7.

Table 7 Combustion model propellant test matrix.

Propellant	% AP by Mass	Modality	% TiO_2 Additive by Mass	Additive Synthesis	AP Size (μm)	Aluminum Mass (%)	Source
Baseline 1	80	Monomodal	0.00	-	200	0	This study
Baseline 2	80	Monomodal	0.00	-	400	0	Morrow et al. [81]
Baseline 3	80	Monomodal	0.00	-	280	0	This Study
Baseline 4	80	Monomodal	0.00	-	45	0	Morrow et al. [82]
Baseline 5	80	Monomodal	0.00	-	20	0	Morrow et al. [81, 82]
Baseline 6	85	Bimodal (70/30)	0.00	-	200/20	0	This study
Baseline 7	85	Monomodal	0.00	-	200	0	This study
Propellant 1	84.6	Bimodal (70/30)	0.40	Dry powder	200/20	0	Allen et al. [83]
Propellant 2	84.6	Bimodal (70/30)	0.40	Pre mixed	200/20	0	Allen et al. [83]
Propellant 3	84.6	Bimodal (70/30)	0.40	In-situ	200/20	0	Allen et al. [83]
Aluminized Baseline	67	Bimodal (70/30)	0.00	-	200/20	16	Allen et al. [83]
Aluminized 1	66.7	Bimodal (70/30)	0.30	Dry powder	200/20	15.9	Allen et al. [83]
Aluminized 2	66.7	Bimodal	0.30	Pre mixed	200	15.9	Allen et al. [83]
Aluminized 3	66.7	Bimodal	0.30	In-situ	200	15.9	Allen et al. [83]

6.1 Propellant Mixing

Solid propellants are composite chemical formulations used to create a mechanical force resulting from the expulsion of pressurized combustion products at a high rate. They contain an oxidizer and a fuel (which may be one in the same for a given component in the case of a double-base propellant) and as such undergo self-sustaining combustion regardless of environment. Composite solid propellants generally consist of a fuel, an oxidizer, and a binder (which may also act as the fuel) to suspend the solid fuel

and oxidizer. In some cases, a propellant may consist of only one substance capable of self-deflagration, called a “monopropellant,” as an example AP will deflagrate as a monopropellant at elevated pressures.

In an effort to establish the procedure, propellants were manufactured in the authors’ laboratory using various AP particle size distributions. AP from Firefox Enterprises and R45-M HTPB were the propellant oxidizer and fuel used in this study. The composite propellant is cured into a solid strand sample (Figure 28) for use in testing by curatives or plasticizers such as isophorone diisocyanate (IPDI). Dioctyl adepate (DOA) and HX-752 bonding agent were also added to the formulations to improve mix viscosity and propellant strength, but they have negligible interactions in the combustion process due to their low concentration and chemical reactivity. Propellants formulated in the authors’ lab were by techniques originally developed by Stephens et al. in 2007 [84].

The study started by evaluating the burning rate and normalized pressure rise of an 80% monomodal baseline propellant using typical particle size distributions of 400, 280, 200, 45, and 23 μm. Obtaining these particle sizes was done through a thorough sieving process using several meshes and a sieve shaker. AP was sieved for 24 hours, and each sized was sieved a minimum of 3 times to ensure narrow distributions were used. Batch differences caused there to be fewer particles below 200 μm, which caused the larger diameter at 280 μm, which also had a wider AP size distribution at the same 200 μm (Figure 29). The Kerra-McGee AP was purchased from Firefox Enterprises, who state that the Kerra-McGee is a higher-quality ingredient.

After examining the performance of the AP size distributions, 85% monomodal and bimodal mixtures were then investigated. Bimodal mixtures were fabricated using two AP sizes mixed into the propellant separately. This study used the 200- and 23-μm AP particles with a mass ratio of 70 to 30%, respectively. Additives removed both fuel and oxidizer to keep the fuel-to-oxidizer ratio the same (fuel/oxidizer of 20/80 or 15/85) and keep the stoichiometry constant.

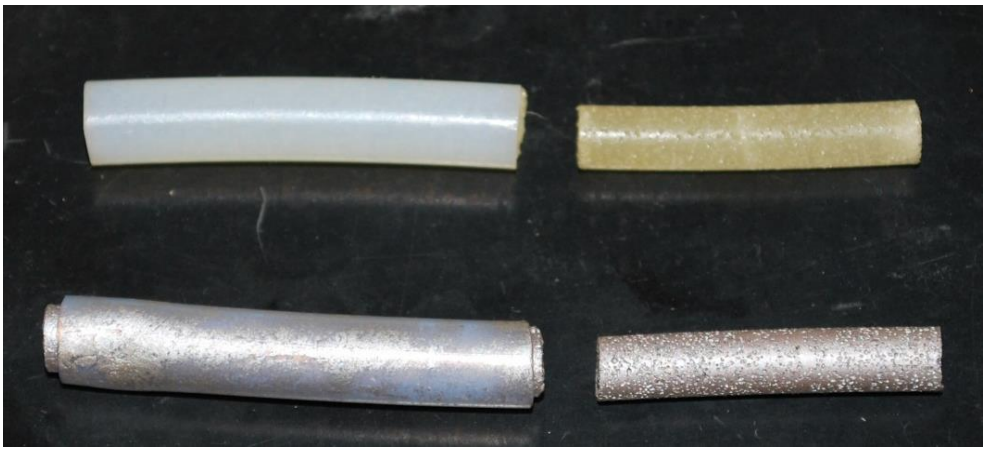

Figure 28 Typical propellant strands cast and prepped for testing.

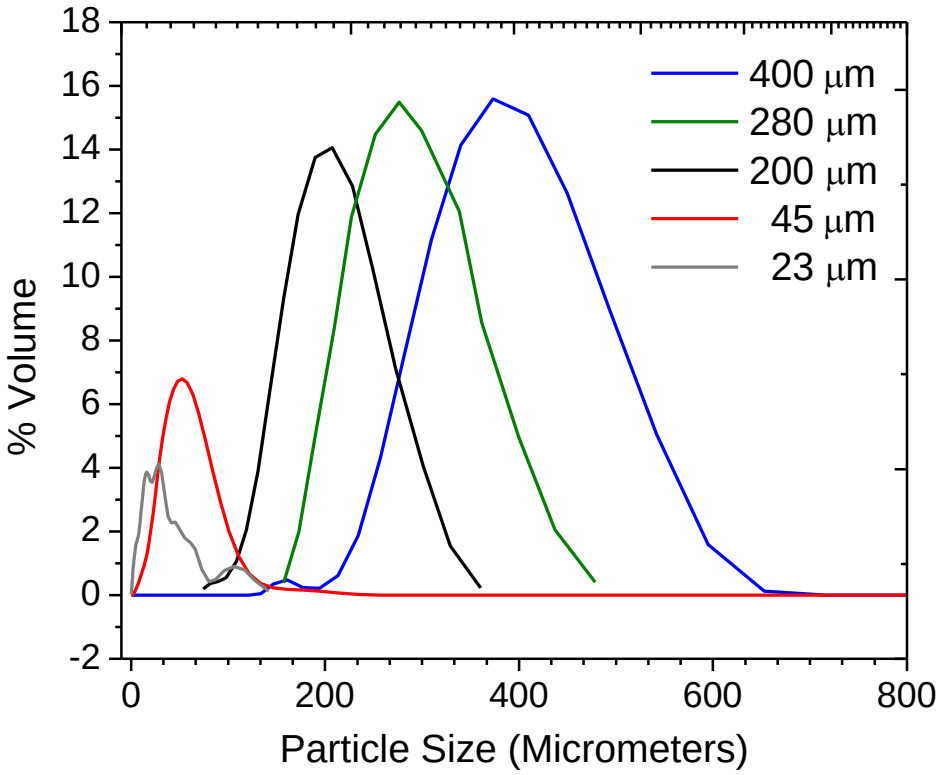

Figure 29 AP particle size distributions for the various propellant mixtures tested.

6.2 Pressure Rise Data

Typical pressure time histories from strand burner experiments are shown in Figs. 6 and 9. Following the period of near-linear pressure increase for a typical strand length (about 25 mm), there is a dramatic inflection point which signified the end of the burn. This inflection point has been shown in previous studies to be the result of a dramatic loss of heat from the chamber gas combined with possible condensation of the water from the combustion products. To test the pressure increase as a function of

propellant sample size (length and diameter), excursion tests were performed with other strand geometries.

Pressure traces from the longer propellant strands had both a linear and non-linear pressure increasing sections within their measured pressure time histories. Upon examination of the pressure traces, the burning profiles from longer strands tended to asymptotically peak at lower pressures. Such a profile indicates that heat transfer effects are starting to influence the burning rate, and this result is consistent with other studies in the literature [34]. As long as the burning time is kept low enough to satisfy the relationship of heat flux out and the change in pressure with increasing time, then heat transfer effects can be ignored [34, 85].

Tests with increased-diameter strands also indicated a drop in the normalized pressure rise even though the samples had similar total burning times to the original test sample size. Heat transfer was also thought to be a problem in such an experiment; however, the relationship indicates that the pressure rise is dependent on the mass flow rate of the propellant (i.e., the generation rate of the product gases). To minimize effects due to larger samples, all tests should be on the same order of magnitude of mass to keep the mass flux similar, particularly when using the pressure rise to assess changes in combustion efficiency.

Finally, measuring the burning rate via high-speed camera will lead to similar results as those obtained by pressure transducer; however, more information is drawn out of the pressure transducer method. Additionally, more scatter is typically found from the video measurement of burning rate due to difficulty in establishing the location of the

burning surface. Propellants in general will burn with a concave surface. A plot comparing burning rate results obtained from video and pressure methods is found in Figure 30. As discussed, the results using the video method produce a higher degree of scatter in the burning rate over the pressure range seen in Fig. 29 when compared with the results obtained from the pressure method.

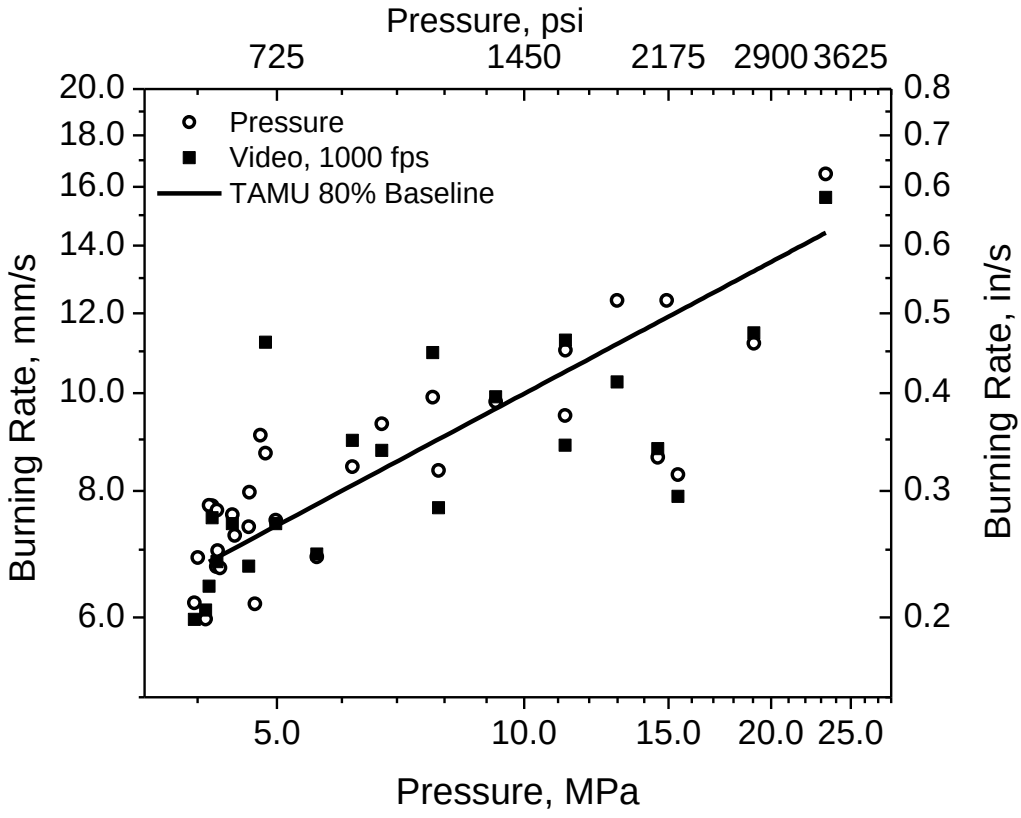

Figure 30 Comparison of burning rate analysis methods, pressure versus video methods. Propellant is an 80% AP/ 20% HTPB propellant with a monomodal AP distribution (200 microns).

The rising pressure in the constant-volume strand burner produces an average burning rate of the propellant strand. However, the pressure rise is due to two key factors: the increase in the temperature due to combustion, and the conversion of the solid to gas. Focusing on the temperature increase from the combustion products, propellants which have identical chemicals with different synthesis methods can be compared. Differences in the maximum pressure rise would indicate changes in the actual flame temperature, as discussed in Chapter 4.

First, the pressure rise of a typical 80% monomodal AP propellant was compared to the average test pressure for two different AP sizes, 198 and 278 μm. The results follow a similar trend to the burning rate, but the propellant with the 280-μm size appears to have the same pressure rise as the 198-μm AP propellant. Figure 31 plots the data compared to trend lines fitting the data. The implication from Fig. 30 is that both mixtures have similar performance since their peak pressures are similar.

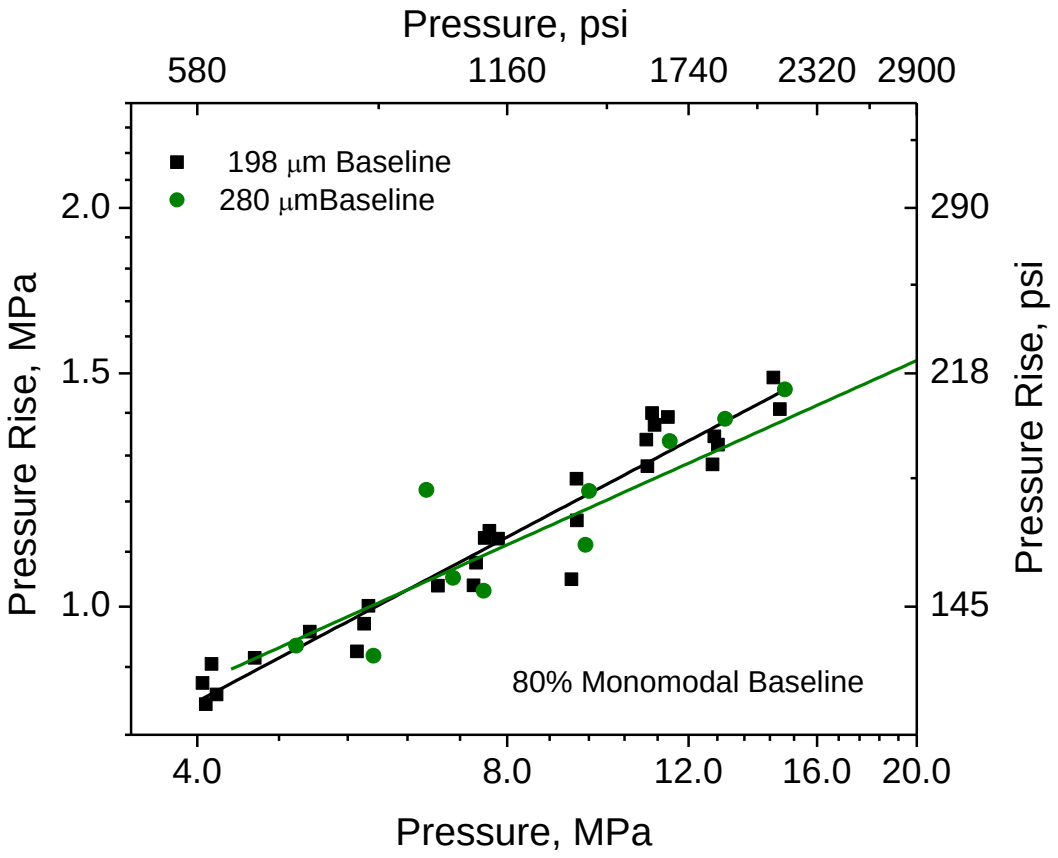

Figure 31 Absolute pressure rise of an 80% monomodal baseline using 198- and 280-μm AP particles.

There is noticeable scatter from just plotting the pressure increase for each propellant strand. This scatter stems from the small fluctuations in the length of each propellant, which then translates into different propellant masses. A larger mass of propellant should lead to a larger final pressure in the chamber. On average, the 280-μm samples were at smaller lengths and therefore had smaller pressure rises. Therefore, a normalization of the pressure rise was applied when comparing two sets of mixtures with their respective peak pressure changes. Figure 32 compares the normalization of the

pressure rise by both mass and length. Either option reduces the scatter by correcting for minor changes in propellant quantity; mass normalization was chosen as the method to use for the present study.

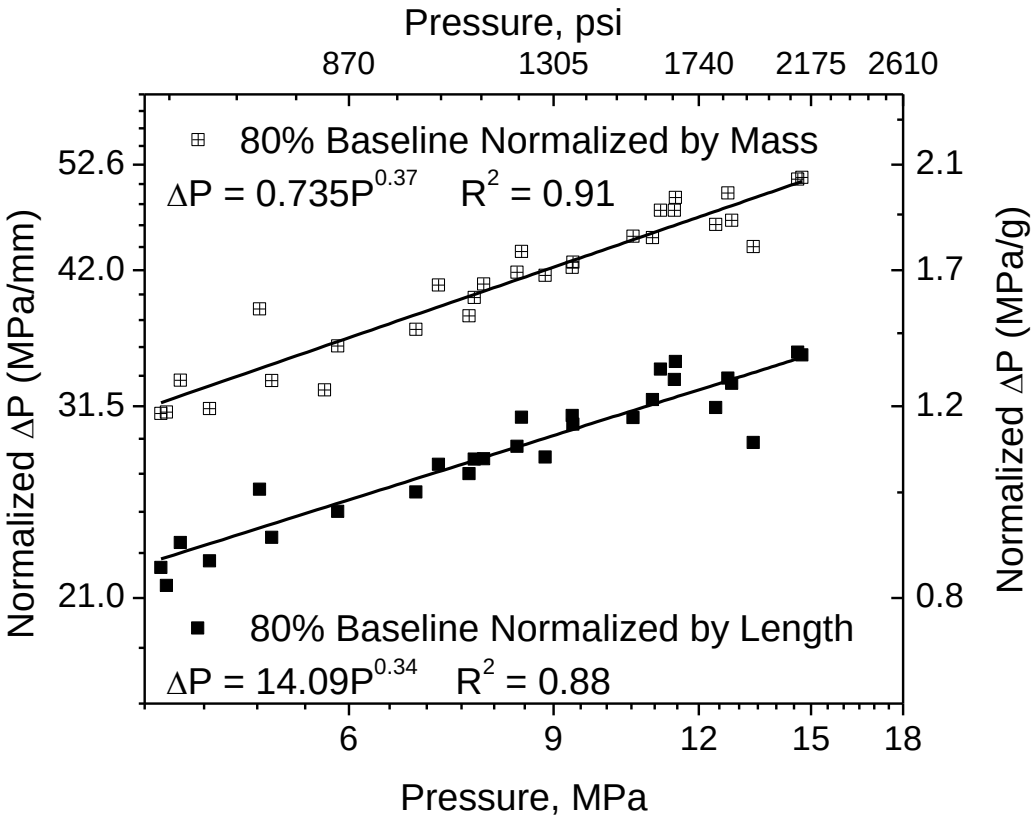

Figure 32 Normaliziation of the pressure rise for an 80% monomodal baseline using 200-µm AP particles.

A comparison of similar propellants was done by varying the size of the AP used to formulate the propellant strand. It is known that the smaller the AP size, the faster the propellant burns. Increased burning rates are brought about by reducing the diffusion limitation of the fuel and oxidizer. A series of propellants was tested containing a single average size of AP at 80% of the total propellant weight. AP sizes of 20-, 45-, 75-, 200-,

280-, and 400-µm particle diameters were tested in an argon bath gas, and the burning rates for each of the propellant batches can be found in

Figure 33. It is important to note that the AP for the 280-µm propellant was not placed in an ultra-sonic bath to break up AP agglomerates, accounting for the lower burning rate. Note that the propellant made with the AP sizes of 20-, 45-, 75-, and 400-µm were used in a study to model and predict the effect of AP size and modality [81, 82]. The data are reproduced here were used to evaluate the pressure rise information.

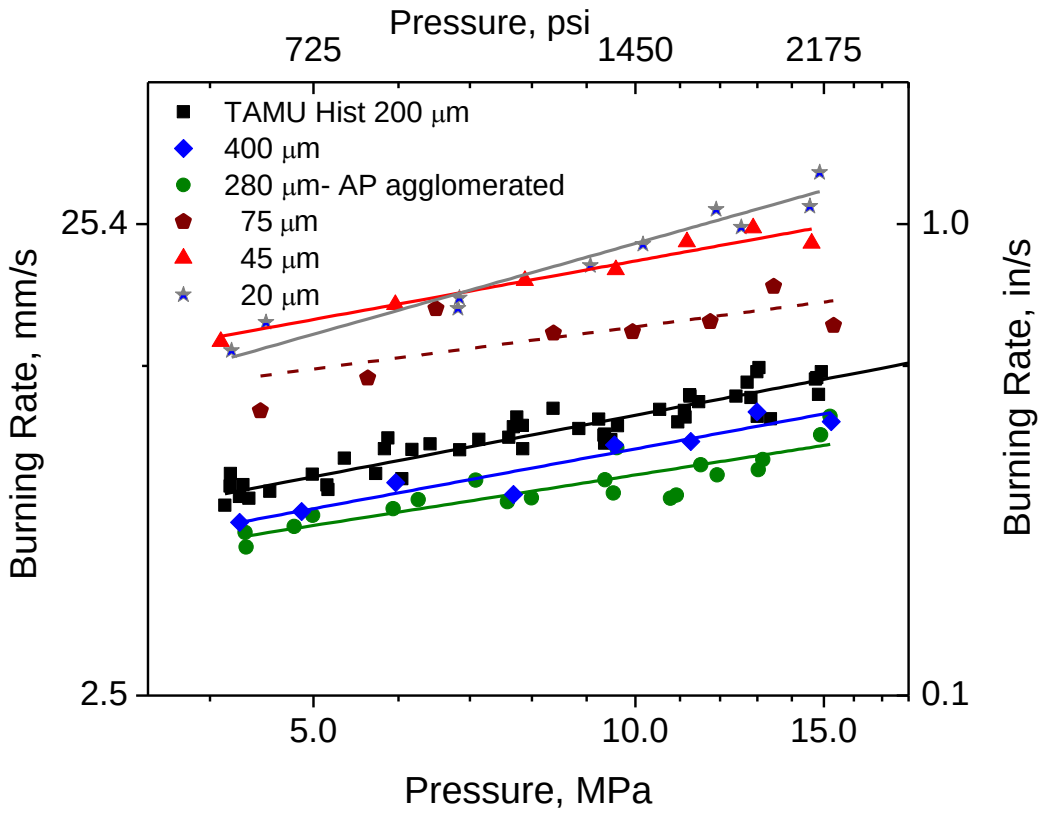

Figure 33 Burning rate comparison of several 80% monomodal baselines using various AP particles. Lines represent best fits to each mixture data set from other studies [81, 82].

Decreasing the particle size of the AP increases the burning rate of the propellant, but below 45 μm in size, the enhancement is negligible. Using the mass-normalized pressure rise from the same set of data, the relative combustion efficiency can be observed. The resulting pressure rise for the various AP particle sized can be found in Figure 34. As the data approach the model-predicted trend, the propellant mixture approaches ideal combustion. In other words, the theoretical performance in terms of flame temperature is predicted to be the same for each of the mixtures in Fig. 33 since the overall stoichiometry is the same for each. Differences in the pressure rise hence imply that the larger particles are more difficult to burn than the smaller ones, where the latter size range is closer to a premixed-combustion limit. Figure 34 is an excellent example of how the pressure rise can be used to compare the combustion efficiencies of comparable mixtures. The differences between each mixture are discernable amidst the natural scatter in the ΔP data.

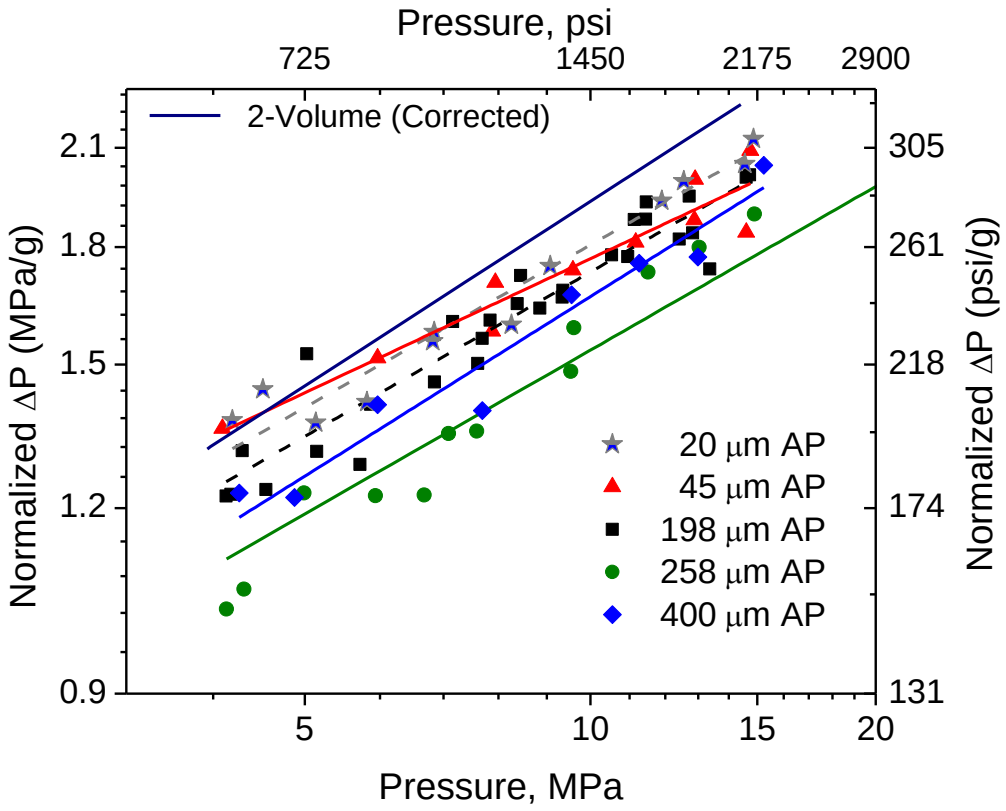

Figure 34 Normalized pressure rise comparison of several 80% monomodal baselines using various-sized AP particles. Lines represent best fits to each data set/mixture in comparison to the prediction of the model from Chapter 4.

As expected, the pressure rise for the propellants containing 20- and 45-μm sized AP were closest to the model prediction. This result indicates that AP smaller than the 20- μm would not provide any more benefit. On an initial observation, the 45-μm-based propellant appears to burn slightly faster than the 20-μm-AP mixture. After examination of the final mixture ratio, the propellants with the 45- and 75- μm AP particle sizes had 0.5% more AP. This increase in AP concentration increases the adiabatic flame temperature by 66 K. A higher adiabatic flame temperature would increase the pressure rise in the strand burner. At higher pressures, the pressure rise for all of the batches tend

to converge together. It is believed that this result is part of the propellant leaving the diffusion-limited burning regime, and the burning is more governed by the kinetic parameters in the premixed regime.

Higher loadings of AP push the propellant stoichiometry closer to stoichiometric conditions with correspondingly higher adiabatic flame temperatures, so the pressure rise is expected to increase for increased AP loadings. In addition, using bimodal mixtures of AP to increase the number of reaction sites and to increase the packing fraction of the solids in the composition propellant is thought to also increase the measured pressure rise due to more-complete combustion (due to the presence of the smaller AP sizes). The results comparing the pure AP/HTPB propellants at different AP mass loadings and AP modality are seen in Figure 35.

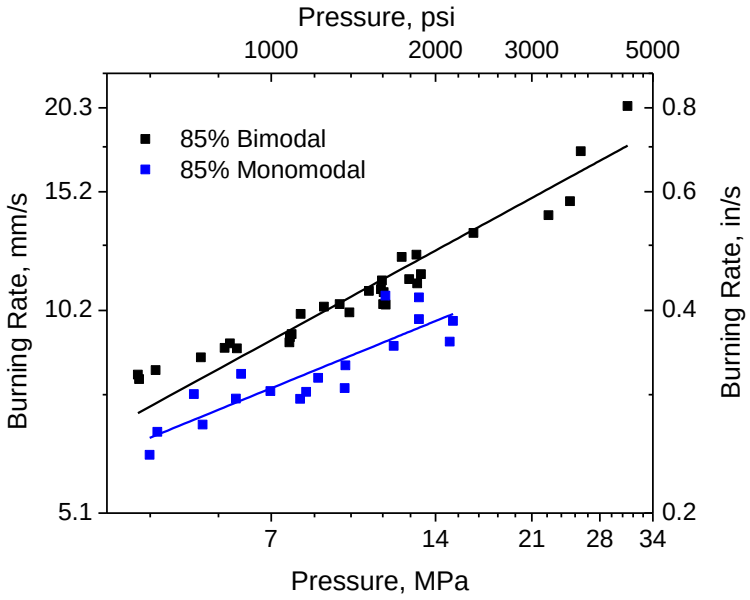

(a) Burning rate profile for the 85% monomodal and 85% bimodal baseline formulations.

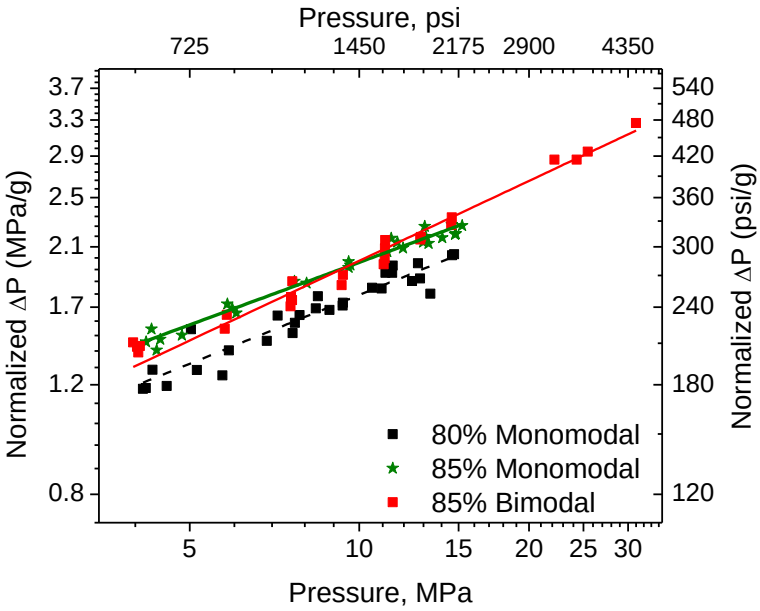

(b) Pressure rise plot comparing the AP/HTPB propellants at 80% and 85% monomodal and the 85% bimodal mixtures.

Figure 35 Comparison of AP quantity and modality for (a) burning rate measurements and (b) normalized pressure rise.

The expected trend moving to higher AP loadings held true, e.g. the ΔP for the 85% monomodal propellant is larger than that for the 80% monomodal propellant. However, the bimodal propellant is observed to have a slightly lower pressure increase at lower pressures when compared to the 85% monomodal case. Arguably, the ΔP results between the monomodal and bimodal cases at 85% AP loading are basically the same within the uncertainty of the data. The burning rate of the bimodal mixture is nonetheless higher (Fig. 33a), indicating there is an advantage to using the bimodal formulation from a burning rate point of view. In general, the efficiency of combustion is not always easily interpreted from the data, particularly when the differences are small, with some of the results in Fig. 34b as an example.

To examine the efficiency of combustion further, catalytic additives were added to the 85% bimodal AP propellant mixture. In recent years, new synthesis methods of titania have been developed to intensify the magnitude of the burning rate increases [14, 17, 20, 83]. Using the pressure-rise-detection method, the impact on the completeness of combustion can be detected. Normalized pressure rise data were collected on the mixtures with dry-powder, pre-mixed, and *in-situ* titania nano-particles and were compared to the baseline formulation. Figure 36 plots the propellants with the addition of 0.3% by weight of the different titania additives. This plot shows the impact of the *in-situ* TiO_2 method, where the pressure rise (and hence combustion efficiency) is markedly higher than the other titania additive methods, particularly at the lower pressures. The other two methods give ΔPs that are similar to those of the baseline formulation,

meaning that although they increase the burning rate of the propellant they do not appear to increase its performance.

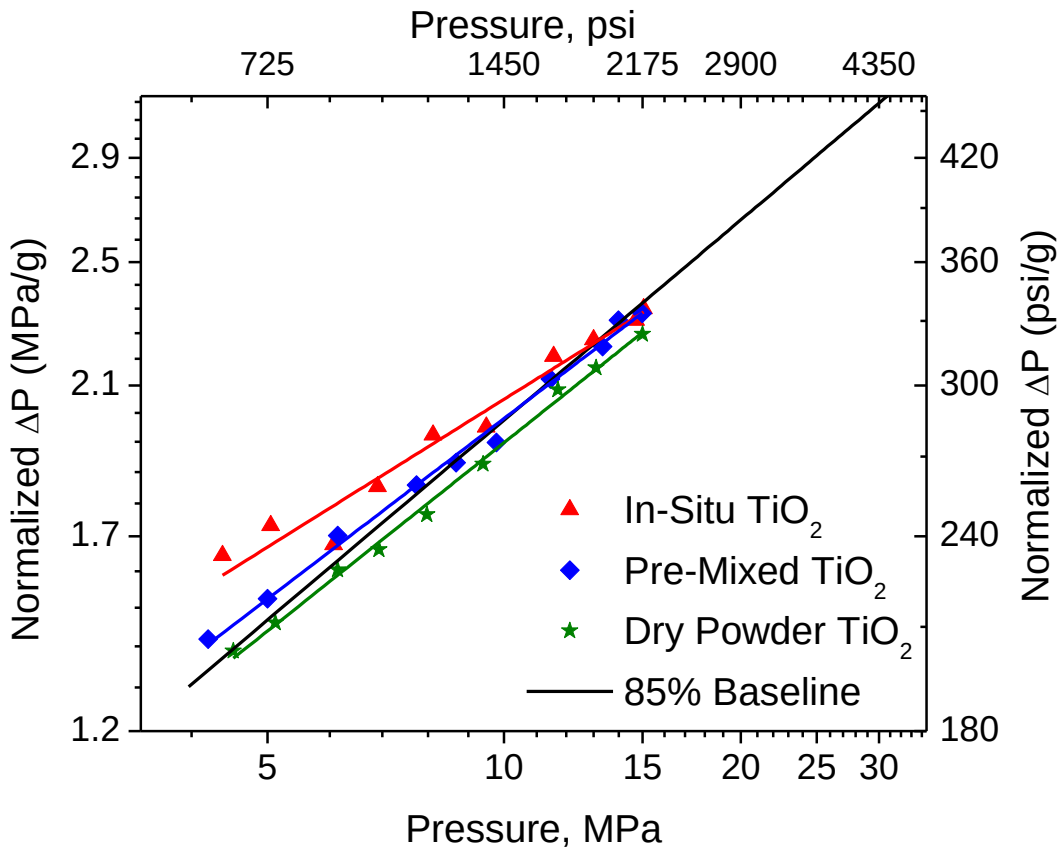

Figure 36 Normalized pressure rise for 85% bimodal propellants containing 0.3% titania via production methods of dry-powder, pre-mixed, and *in-situ*.

This *in-situ* method can also be applied to an aluminized propellant formulation to examine the combustion efficiency of aluminum in the propellant. Aluminized propellants with 16% aluminum by weight were manufactured with both titania and iron oxide at 1.0% by weight and were compared to a baseline formulation without any additive. Iron oxide was observed to increase the normalized pressure rise over the

baseline formulation. The inclusion of dry-powder titania decreased the pressure rise, but increased the burning rate as seen in previous studies. In contrast, *In-situ* titania was added at only 0.4% by weight and increased the pressure rise closer to that of the dry powder iron oxide (with a 1% loading) as observed in Figure 37.

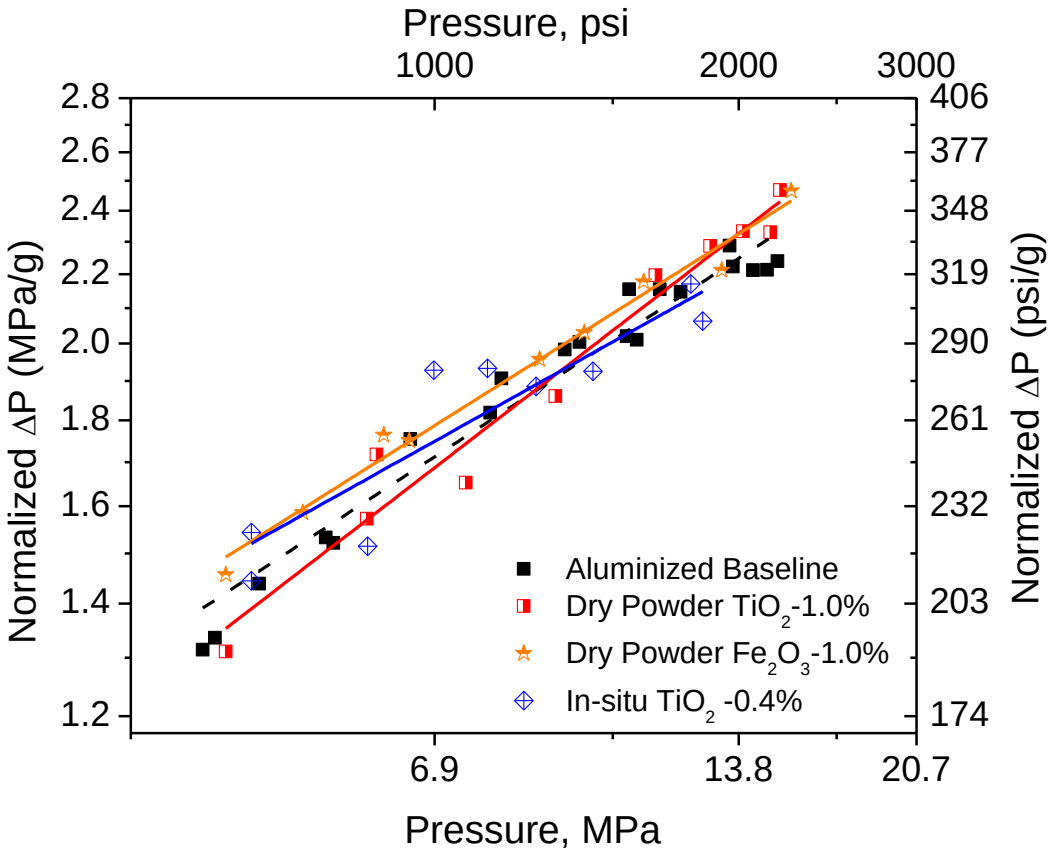

Figure 37 Combustion efficiency based on a mass-normalized pressure increase for 85% bimodal with dry power, pre-mixed, and *in-situ* titania (left) and aluminized composite propellants containing dry power iron oxide and titania (right).

The pressure rise results appear to indicate larger pressure increases as the titania synthesis method is altered. Propellants with dry-powder titania addition appear to have a decrease in the overall pressure rise, even though the burning rate has been observed to

increase in other studies. The higher burning rate is thought to be a product of better particle dispersion in the propellant matrix; by examining the pressure-rise data, the propellant with *in-situ* titania has the highest pressure rise which would indicate a higher chamber temperature and/or more complete combustion. Using the current version of the model, a temperature difference of 230 K between the dry powder- and the *in-situ* -titania-containing propellants is estimated. Thus, the *in-situ* titania is thought to increase the c* and combustion efficiencies. Figure 38 shows what a pressure rise line looks with the 230-K change in the flame temperature by using the *in-situ* titania.

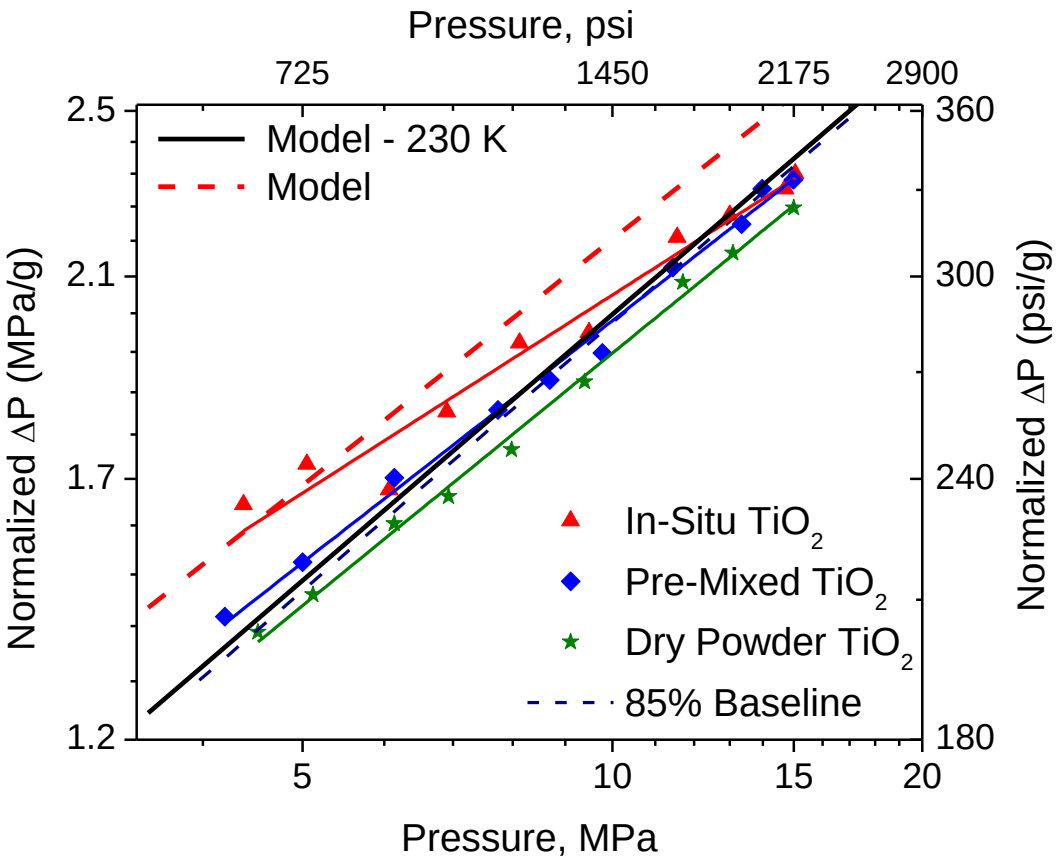

Figure 38 Indication of a 250-K change in the flame temperature from the use of *in-situ* titania.

Using the current version of the model, changes in the flame temperature can be evaluated based on the magnitude of the pressure increase. Using this temperature change, numeric estimates for the increase in chemical c* efficiency can be calculated. Table 8 shows the relative increase in the c* efficiency for the tested propellants in this chapter. Normalized pressure rise of each propellant is given for the pressure.

Table 8 Change in chemical c* efficiency based on matching the model pressure rise to pressure rise from the experiments.

Mixture	% AP by Mass	AP Size (μm)	Normalized Pressure Rise at 6.89 MPa (MPa/g)	Temperature Change (K)	C* Change (%)
Baseline 1	80	200	1.51	-	-
Baseline 2	80	400	1.43	-50	-1.18%
Baseline 3	80	280	1.34	-200	-4.80%
Baseline 4	80	45	1.58	200	4.58%
Baseline 5	80	20	1.58	200	4.58%
Baseline 6	85	200	1.73	-	-
Baseline 7	85	200/20	1.68	*	-
Propellant 1 (Dry Powder)	84.6	200/20	1.63	25	0.54%
Propellant 2 (Pre-Mixed)	84.6	200/20	1.71	100	2.14%
Propellant 3 (*In-Situ*)	84.6	200/20	1.80	230	4.85%

Baselines 6 and 7 had relatively the same temperature and c, thus no data available.

Most studies do not indicate the c* efficiency, but according to Kubota, typical composite propellants are 85 to 95% chemically efficient [74]. The relative values for c* found are consistent with literature. However, the increases in the pressure rise could be due to more solid mass being converted to gas. Converting more solid to gas would reduce the quantity of soot produced, opening more gas phase kinetic pathways for

combustion. The temperatures would then be lower, thus would lower the changes in c* values determined.

6.3 Measurement Uncertainties

With the implementation of high-speed photography, burning rate measurement error can better explained. Propellant burns can have burning surfaces which have changing geometries. When the burning area changes, it is difficult to track a point on the burning surface to calculate the burning rate. Error is then introduced to the burning rate measurement. Figure 39 is an example of a propellant burning with larger burning area due to the jagged shape formed during the burn. A larger burning surface still maintains a linear pressure versus time profile, but has a higher average burning rate. There is a higher mass flow rate which results in a larger increase of pressure in the strand burner, which is a known geometry effect [2].

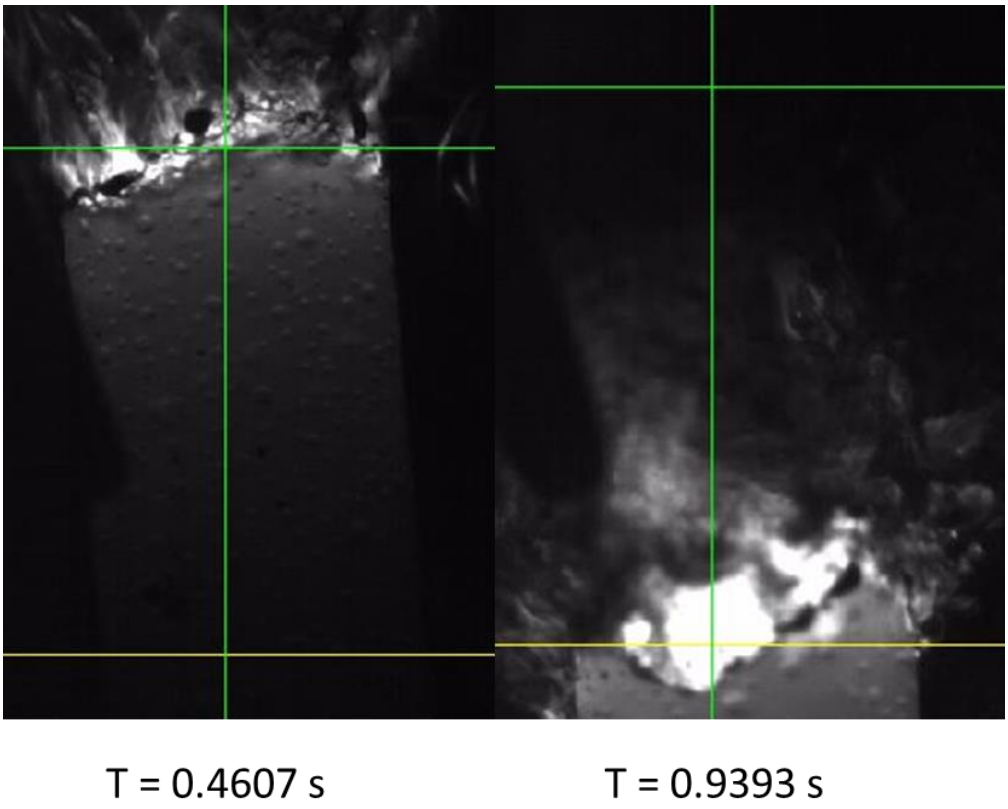

Figure 39 Example of a single propellant burning at the start and end time to determine the burning rate. The larger burning surface leading to higher burning rate measurement uncertainty.

The primary sources of variability in the burning rate constants are the natural combustion fluctuations and variability in mixture uniformity from batch to batch. A minimum of ten samples are burned for each propellant batch so as to minimize the effects of spatial variation in mixture uniformity. Each sample's density and overall uniformity are evaluated from physical measurements of the mass and length. Density variations can also account for experimental scatter; lower densities signal the presence of air voids which will inflate the burning rate. Error bars representing 10% error in the

measurements are generally plotted along with burning rate. A least-squares regression correlation is used to better represent the scatter observed in the tested propellant batches. Uncertainty stems from the measurements for both sample length and mass, adding to the additional level of ambiguity to the burning rate correlations.

Total measurement uncertainty was determined using the root-sum-square (RSS) method from the individual measurements of the pressure/light traces, sample length/mass, and time resolution. Since there is no correlation between the instrumentation errors, the RSS method serves as a sufficient method in determining the uncertainty amongst the data. Tolerances in the sample length and mass measurements as well as burn time were found to be ±0.005 in (0.125 mm), ±0.01 g, and ±0.032 s, respectively. Using a root-sum-square (RSS) approach on the minimum and maximum burning rates observed, the value for the combined uncertainty in burning rate was found to range from 3.3% to 4.3%. The uncertainty in the DAQ pressure transducer is 0.15%, as reported by the manufacturer, which amounts to less than 1 psi at the lower end of the pressure range (500 psi, 3.5 MPa) and 4.5 psi at the upper end (3000 psi, 20.8 MPa). These numbers are routinely compared to a calibration pressure transducer and have been found to agree with the variation in pressure measured with the calibration.

The overall normalized pressure rise uncertainty for this study ranged from 5.0% to 5.8%. Most of the uncertainty comes from the transient ignition portion of the pressure trace. As seen in Figure 40, the magnified time of ignition shows a gap of the transient portion of the burn. This duration of the transient portion causes the overall measurement uncertainty to increase. Although the overall measurement uncertainty is

between 5.0 and 5.8%, the actual burning rates typically fall within 10% scatter of the predicted burning rates using a best-fit trend line. This difference represents additional random error in the measurements that are due to some of the effects mentioned above.

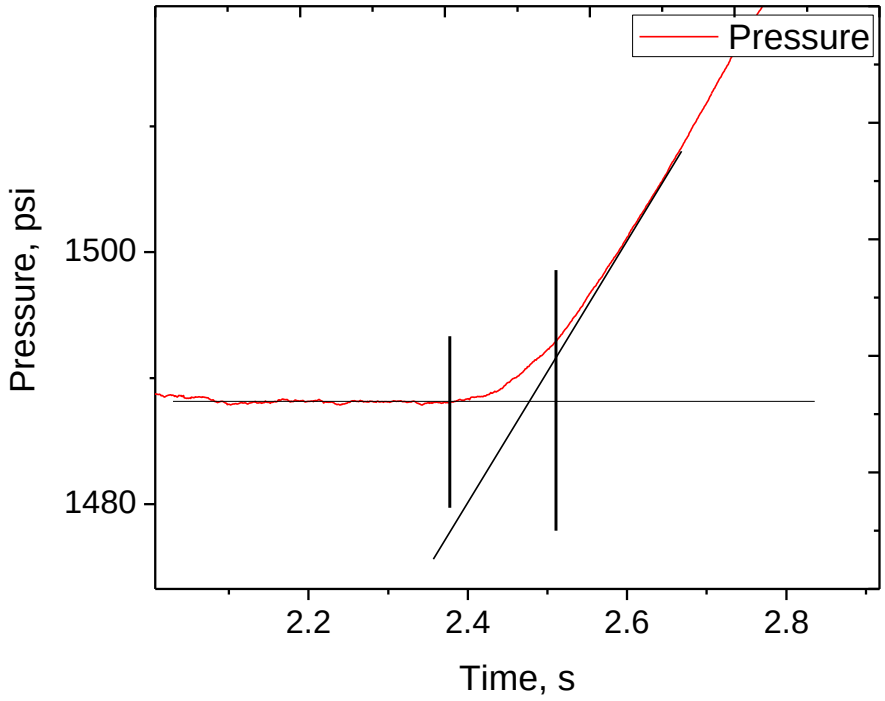

Figure 40 Example uncertainty in time measurement using the pressure trace from the test with the most error.

6.4 Discussion

The ability to obtain a relative chemical performance from a constant-volume strand burner is highly valuable data for propellant additive evaluation and modeling. Simple models for predicting the pressure rise were refined from previous work on modeling propellant ballistics. In an effort to more accurately model the experimental

pressure rise, heat transfer was added during the burning time. The impact to heat loss was negligible for short burning times, but it is important for modeling the post combustion decay in the pressure trace. Appendix D shows the improvements made to the Frazier combustion portion of the strand burner model. Post combustion pressure decay was not modeled.

Chemical c* efficiency for solid rocket propellants is not commonly found in the literature; it is nonetheless well known that solid propellant combustion has a lower efficiency than, for example, liquid propellant rockets and gas turbine burners. By employing the methods discussed in this dissertation, additive synthesis techniques can be evaluated on how well the additive increases the completeness of combustion. Relative changes in the completeness of combustion can be observed in the final pressure of the strand burner. A propellant strand being fully converted to a gas with no soot production would result in higher changes in entropy from the conversion. To validate the theory, allowing the strand burner to cool to room temperature would allow a direct comparison of gas conversion. If two propellants of the same formulation but with different additive synthesis techniques result in different final pressures, then the additive with the higher pressure likely converted more propellant to combustion products. In this study, variations in the final pressure were not measured since they are typically masked by the noise in the pressure trace and small leaking of the vessel.

6.5 Summary

Propellant testing is commonly performed in both constant-volume and constant-pressure strand-burners. Constant-pressure strand burners are able to measure the propellant burning rate directly, and constant-volume strand burners measure an average burning rate due to the inherent pressure rise in such systems. However, additional information is contained within the pressure rise data, such as the level of combustion efficiency. Pressure rise in a constant-volume strand burner was investigated in this chapter, and a method to evaluate chemical performance was found therefrom. By examining the peak pressure rise, it was found that the *in-situ* synthesis of TiO_2 catalyzed combustion more efficiently, resulting in higher combustion product (and hence chamber) temperatures. The peak pressure method was also used to show the effect of AP particle size on the combustion efficiency, where small particles not only increase the propellant burning rate but also increase its combustion efficiency.

A simple, closed-system thermodynamic model was developed to validate the pressure rise results, particularly in reproducing the effect of average chamber pressure on the peak pressure rise. The model started with a basic ideal gas mixing, but resulted ultimately in a two-volume system. To improve the accuracy in the future, both partial ideal gas mixing and heat transfer effects can be added in the future.

CHAPTER VII

IGNITION DELAY TIME

7.1 Ignition Delay Time Results

Propellant ignition delay time data were collected using the method described in Chapter II, and the results are herein plotted as a function of varying pressure and power. Testing began by burning the non-aluminized APCPs and then testing the effects of the aluminized APCPs on the ignition delay time. First, propellants at 80 and 85% AP were tested over a range of powers at a pressure of 4 MPa and compared to literature values. Then, an 80% monomodal baseline mixture was tested at input fluxes of approximately 80 W (85 W/cm^2) and 55 W (60 W/cm^2) to determine an appropriate power level for testing. A table of propellants tested for this study is found as Table 9.

Table 9 Ignition delay time propellant test matrix.

Ignition Propellants	AP Mass (%)	Modality	Additive Mass (%)	*In-Situ* Additive	Additive Size	Aluminum Mass (%)
Baseline 1	80	Monomodal	0.00	-	-	0
Baseline 2	85	Monomodal	0.00	-	-	0
Propellant 1	79.9	Monomodal	0.40	TiO_2	20 nm	0
Propellant 2	79.9	Monomodal	0.40	Fe_2O_3	20 nm	0
Aluminized Baseline	67	Bimodal	0.00	-	-	16
Aluminized w/ Additive	66.7	Bimodal	0.30	TiO_2	20 nm	15.9
Aluminized w/ Additive	66.7	Bimodal	0.30	Fe_2O_3	20 nm	15.9

Testing revealed that the ignition delay time measurement should be done at lower power levels, as mentioned above. The next test was to determine the influence of the AP content on the ignition timing, thus an 85% monomodal propellant was tested using power fluxes of approximately 55 W and 100 W (60 and 105 W/cm^2). By increasing the AP content in the propellant, the ignition delay time was decreased slightly, and the results can be found in Fig. 41. Ignition delay time was recorded over a pressure range from 4 to 20 MPa compared to the ignition model of an 80/20 AP/HTPB propellant by Smyth [86]. The results can be found in Figure 42.

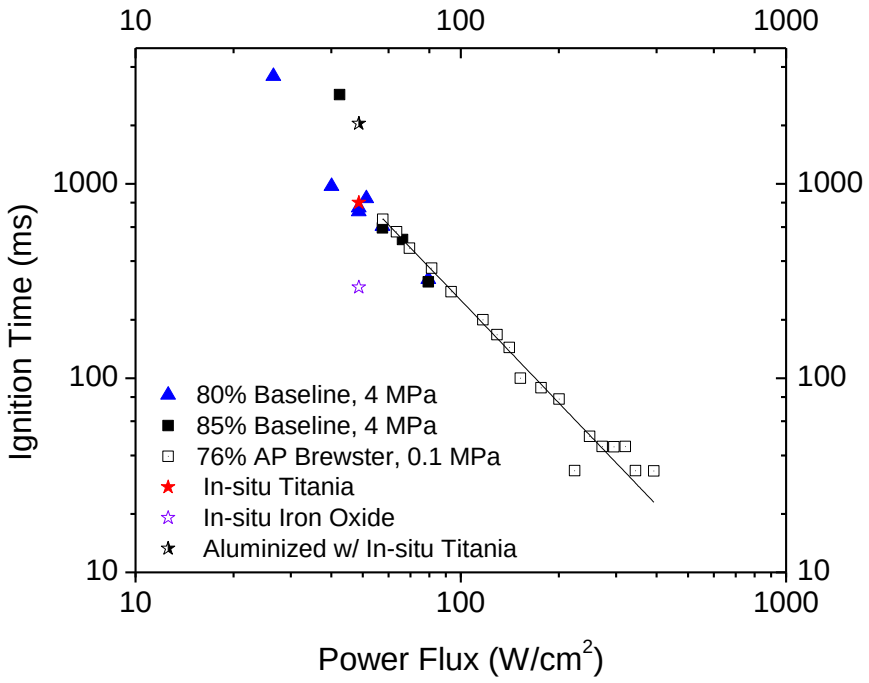

Figure 41. Ignition delay times for the baseline formulations of APCPs over a range of power flux settings. Both the 80% AP (Blue Triangles) and 85% AP (black square) propellants used 200-µm AP particles. The initial pressure was left constant at 4 MPa (600 psi). Data by Cain and Brewster [7] are for a 76% fine AP propellant, where the AP was 2 µm (open squares).

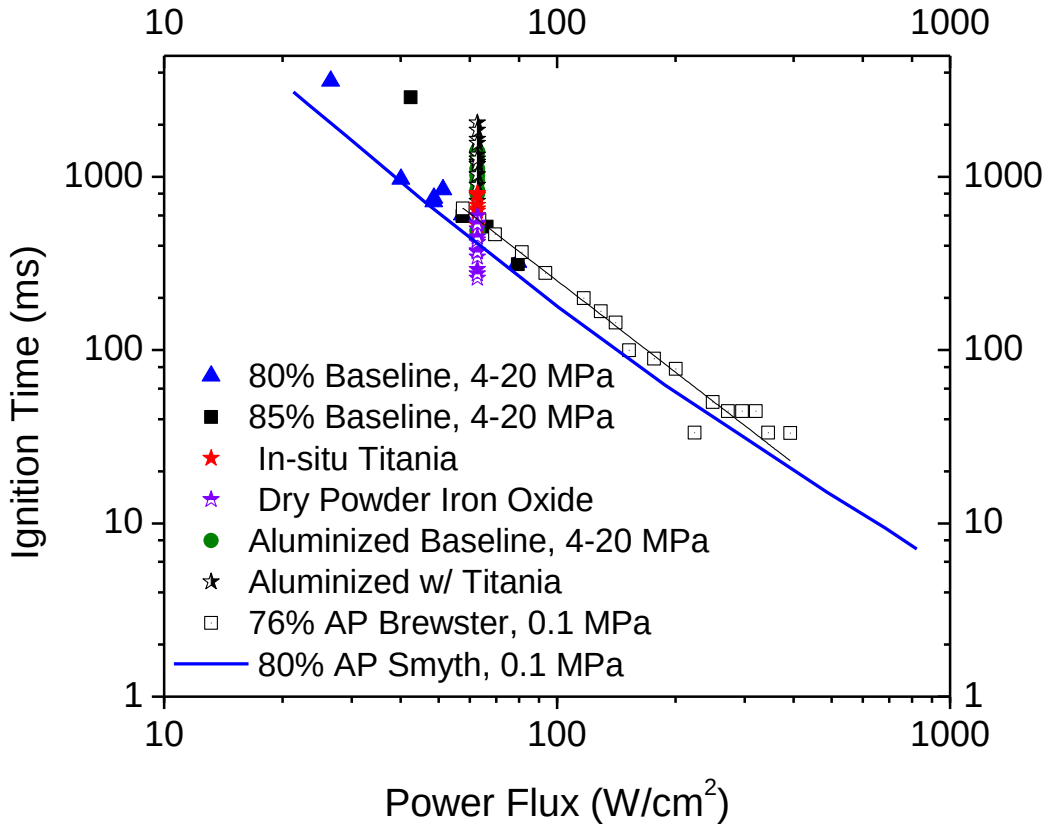

Figure 42 Ignition delay time results presented over a wide pressure range with the addition of the Smyth model [86].

The trend of the ignition delay time versus power was the same as indicated by some of the data available in the literature. Although the literature propellant formulations are different [42, 47] from those herein, they are similar enough for at least a qualitative comparison. The propellant burned by Brewster and coworkers was an APCP that used only fine AP (2 μm) at 76% by weight of the propellant. Smaller AP particles were shown to lower the ignition delay time. Using small AP in combination

with testing at a lower pressure (0.1 MPa as opposed to 4 MPa) prevents a direct comparison, but the results serve as a good indication of the expected time scales and of the effect of laser power flux. As seen in Fig. 40, the data from Cain and Brewster [42] actually line up remarkably well with the ignition delay time data from the present study when plotted as a function of power flux.

To determine the pressure dependence of the ignition delay time, the baseline formulations were tested over a pressure range of 3.5 to 15.5 MPa (500-2250 psi). The Results indicate that as the pressure increases, the ignition delay time decreases, but at a slope that depends on the propellant properties. The results are plotted in Figure 43. As expected (looking at the 55-W results), the propellant formulation with the larger AP percentage (85%) exhibited a lower ignition delay time when compared to the 80% AP propellant. In turn, the higher laser power of 100 W further decreased the ignition delay time of the 85% AP formulation, and this higher-power case led to an almost pressure-independent result, around 350 ms.

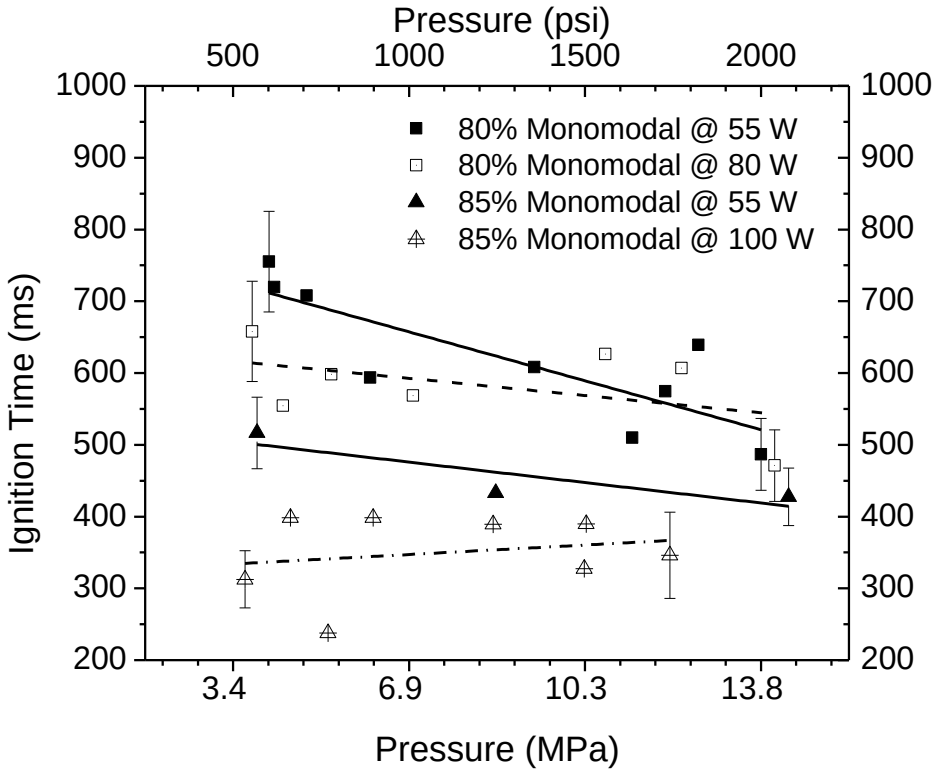

Figure 43 Ignition delay times for the non-aluminized formulations of APCPs at different power flux settings. Error bars of 10% are plotted for each mixture. The 85% monomodal baseline formulation (triangles) was tested at powers of approximately 55 and 100 W (60 and 105 W/cm^2). The power was then reduced to 85 W/cm^2 for the 80% monomodal baseline propellant (open squares) and 60 W/cm^2 for the 80% baseline propellant (solid squares).

The increased AP loading in the propellant caused a decrease in the ignition delay time, leading to the belief that the primary mechanism to alter the ignition delay time is to alter the decomposition of the AP. Although this trend with increasing AP concentration also holds with respect to corresponding increases in propellant burning rate, it is not a general correlation between burning rate and ignition delay time. That is,

increasing the burning rate does not always lead to a decrease in the ignition delay time, and vice versa.

After evaluating the baseline propellant and establishing an appropriate power level for testing, the titania-containing propellant was tested. *In-situ* titania was added to the 80% monomodal propellant and ignited using a power of 55 W (60 W/cm^2); this also resulted in a decreasing delay time as the pressure was increased. However, the actual ignition delay times with the titania did not differ from those of the baseline propellant within the repeatability of the results, as can be seen in Figure 44. Hence, the titania additives in this case do not seem to affect the propellant's ignition time.

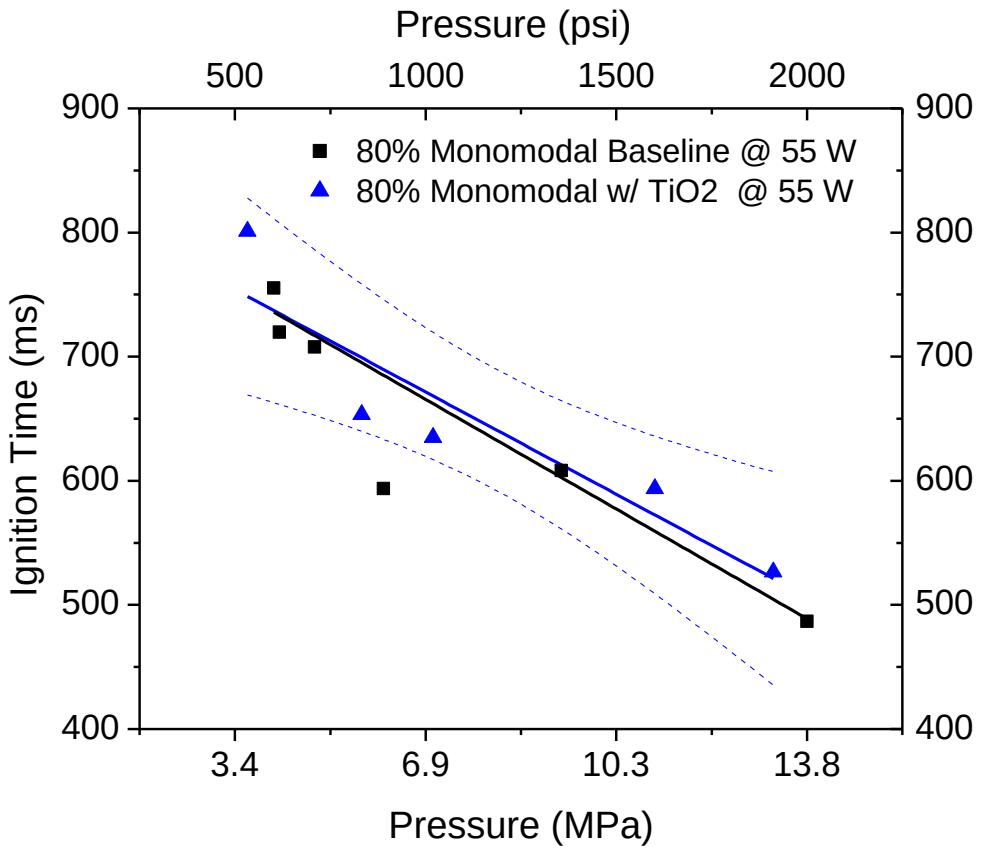

Figure 44 Ignition delay times for the non-aluminized formulations of APCPs. The dashed lines are 90% confidence bands for each mixture. Comparing the ignition delay times of the baseline propellant (black squares) and the propellant with titania (blue triangles) at 60 W/cm^2, the titania does not seem to influence the ignition delay time.

Limited data on the pressure dependence of the ignition delay time using radiative heating indicated that the ignition delay time should decrease as the pressure increases [87, 88]. It was postulated that the chemical reactions between propellant constituents, which result in runaway heating conditions, occur in the gas phase at some small but finite distance from the solid surface [88-90]. Elevated pressures push the gas phase reactions closer to the surface, keeping the hotter gases near the point of eventual

ignition. Both the baseline and the titania-containing propellants resulted in ignition delay times which varied inversely with pressure. The results indicate that the addition of the *in-situ* titania does not alter the ignition delay time for a non-aluminized APCP. This outcome was expected since current theories state that titania aids in the high-temperature decomposition (HTD) of the AP [16, 39, 91]. Titania was added to further test this theory and with the additional thought that by adding a nano-sized metal oxide that was uniformly dispersed, the overall absorption coefficient might increase in addition to increasing the burning rate.

Possibly adding a different metal oxide, such as Fe_2O_3, would alter the ignition timing of the APCPs since it is thought to catalyze the low-temperature decomposition of AP. Iron oxide and copper (II) oxide are both believed to aid in the low-temperature decomposition (LTD) of AP [12, 13]. Investigation into the morphology of an iron oxide catalyst showed that nano α-Fe_2O_3 exhibits better performance than the amorphous structure in the catalytic combustion of a composite propellant [92].

To test the lower-temperature decomposition theory, propellant samples were made using nano-Fe_2O_3. The results indicate that Fe_2O_3 does in fact lower the ignition delay time, but it alters the pressure dependency. Figure 45 plots the results as a function of pressure. At 700 psi, the ignition time was more than halved, but the reduction in ignition delay time decreases with increasing pressure, up to at least about 2000 psi for the limits of the present study. A minimum ignition energy was found by multiplying the ignition delay time by the power of the supplied laser. The results were plotted on the

same figure as the ignition delay times. Ignition energy was corrected for loss of energy from the opening of the shutter, which accounted for about 75.7 mJ lost.

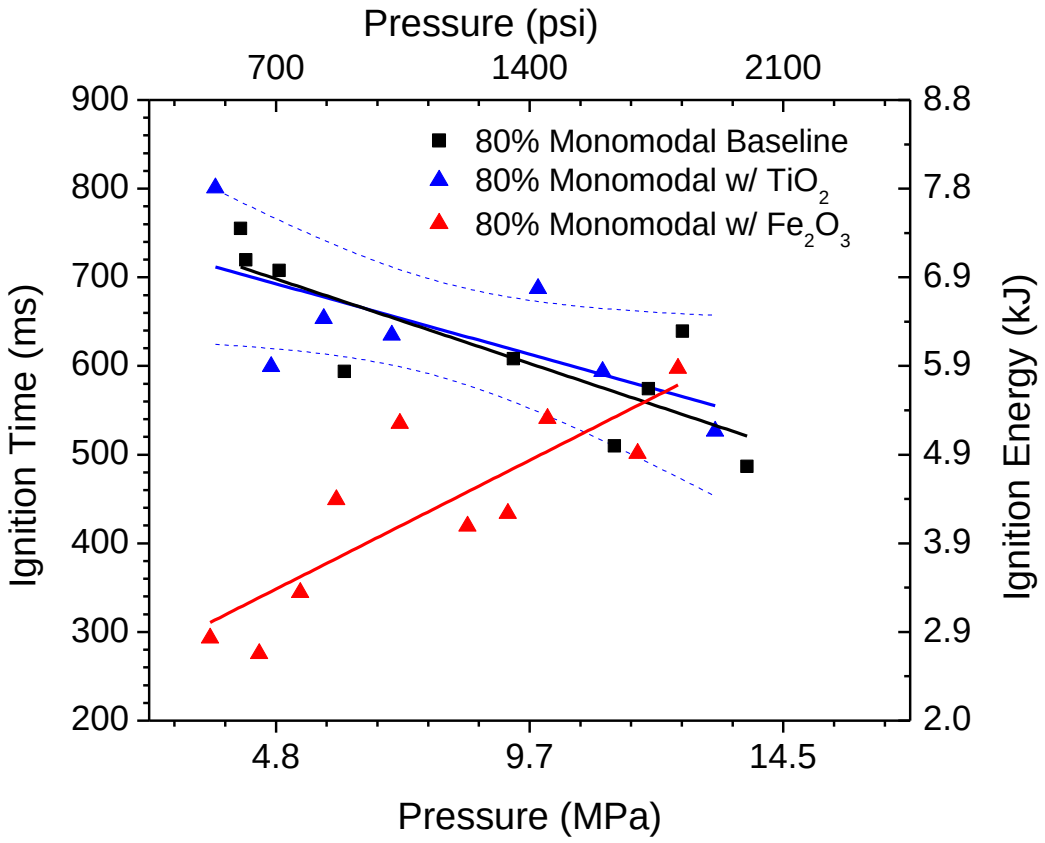

Figure 45 Ignition delay times for the non-aluminized formulations of APCPs. The dashed lines are 90% confidence bands for each mixture. Comparing the ignition delay times of the baseline propellant (black squares), the propellant with titania (blue stars), and the Fe_2O_3 (red triangles), at 60 W/cm^2, Fe_2O_3 was found to decrease the ignition delay time at low pressures.

Iron oxide resulted in the opposite dependence on pressure as the baseline and the titania-containing propellants. This phenomenon could be explained by the kinetic versus diffusion breakdown of the AP. Iron oxide aids in decomposing the AP more in the condensed phase, and by catalyzing the condensed phase, the gas phase production is accelerated. Low-pressure propellant combustion is typically diffusion limited, and the iron oxide lowers the diffusion constraint by catalytically accelerating the condensed-phase reactions. After the results indicated that there was no effect of the titania on the non-aluminized formulation, the aluminized formulations were then tested. First, a formulation containing no titania was tested to establish a baseline. The results for the aluminized formulations are found in Figure 46.

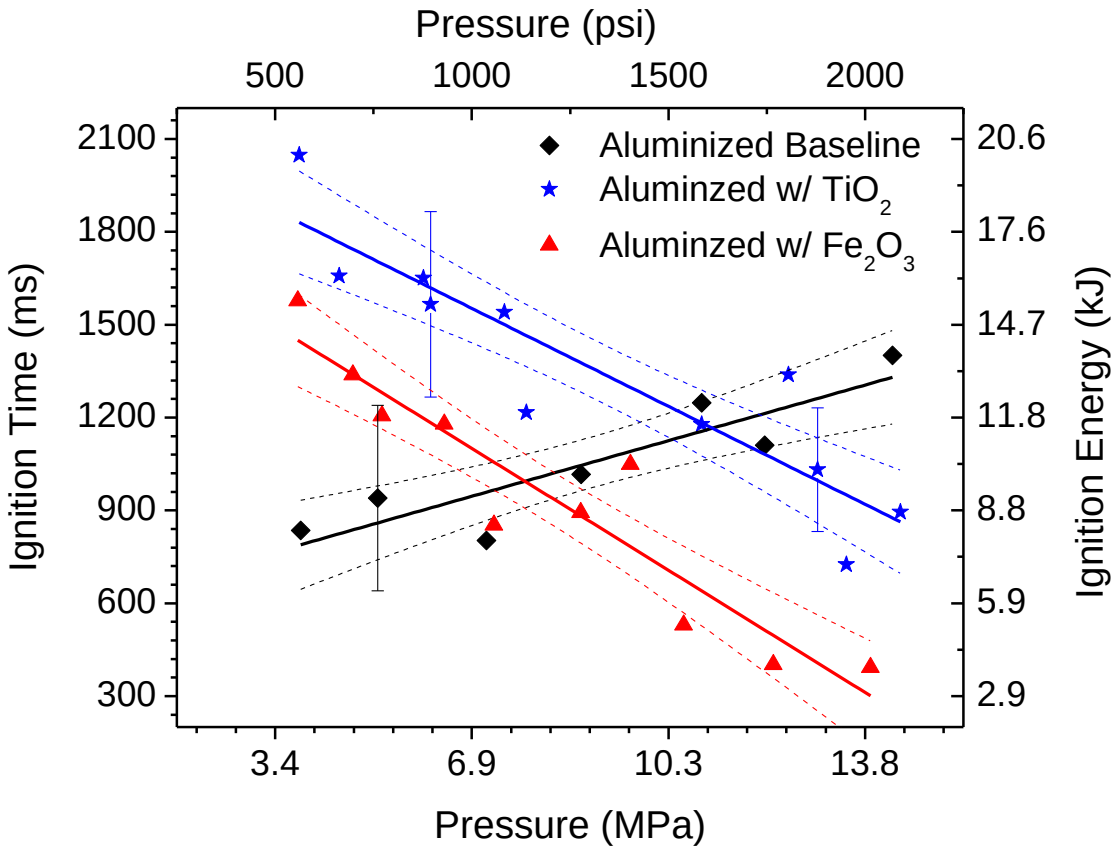

Figure 46 Ignition delay times for the aluminized formulations of APCPs at a power flux setting of 60 W/cm^2. The dashed lines are 90% confidence bands for each mixture. The baseline formulation (black diamonds) appears to have a reverse trend, but when titania (blue stars) and the Fe_2O_3 (red triangles) were added, the trend was returned to the expected behavior, similar to that observed for the non-aluminized formulations.

Interestingly, the aluminized baseline propellant were observed to have an ignition delay time which increases with pressure (Figure 46), which was the opposite of the trend for the non-aluminized mixtures seen in Figure 45. This trend could be that the aluminum requires more energy to be absorbed prior to ignition, thus leading to longer ignition times. AP crystals have been observed to have a slower burning rate in the

region of 1000 to 2000 psi as demonstrated in the literature, which may allow the aluminum to absorb and conduct the heat to other regions of the propellant [93, 94]. It was more likely that aluminum causes the heat to be conducted away from the AP, thus slowing the decomposition mechanism of the AP at the time of ignition.

However, as seen in Figure 46, the addition of titania and iron oxide completely reverses the pressure dependence of the aluminized propellant, making it more like what was seen for the non-aluminized propellants in Figure 44 and Figure 45. A previous study indicated that the critical ignition temperature for a propellant strand decreases as pressure increases as a result of the combustion gasses being closer to the surface [95]. A decreased ignition temperature would result in a decrease in the time to ignite the propellant and would lead to a decrease in the ignition delay time. Using catalysts which alter the AP decomposition temperature, such as titania and iron oxide, should reduce the time to ignite. The results herein indicate the iron oxide reduces the ignition delay time but titania did not alter the ignition delay time. It is believed that the titania did not alter the ignition delay time since titania aids in the high temperature decomposition of AP. Iron oxide lowered the ignition delay time since it aids in the low temperature decomposition of AP, thus allowing the AP to break down and ignite at a faster rate.

As mentioned above, to obtain the ignition delay time a photodiode collected the light emitted from the propellant upon ignition, thus marking the time of ignition. This light can also be observed using high-speed cinematography. Ignition of the propellant was observed using high-speed photography to compare how the flame propagation differs between the aluminized and non-aluminized APCPs as well as serving as a

quality control. The first light and flame propagation of the non-aluminized propellant is found in Figure 47, and the results for the aluminized propellant are found in Figure 48.

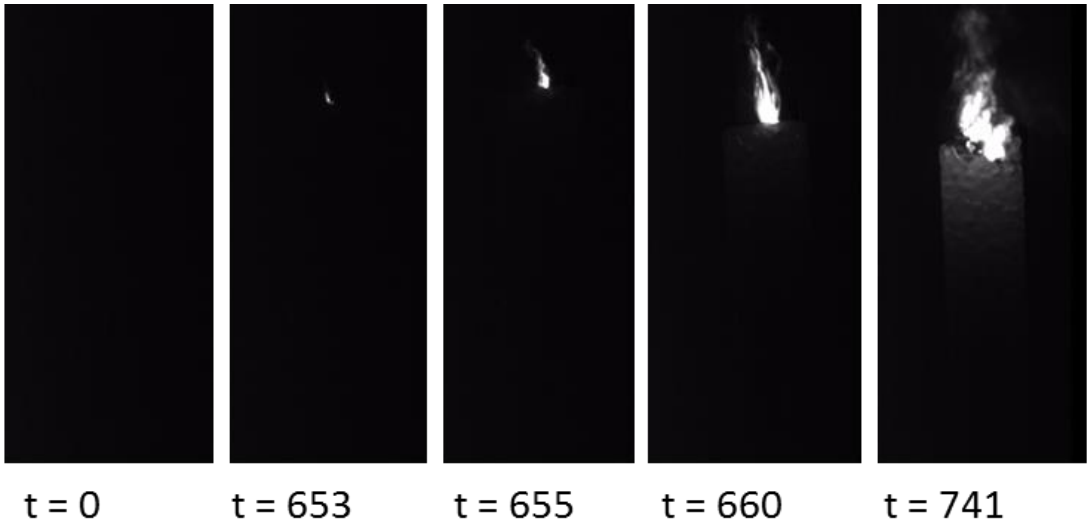

Figure 47 High-speed images of the ignition event for the reduced-smoke APCP, noting that the time spacing was not the same between each frame. A small flame was seen to propagate from the middle of the propellant, which was expected since the beam was known to have a Gaussian profile with the center being the point of highest intensity.

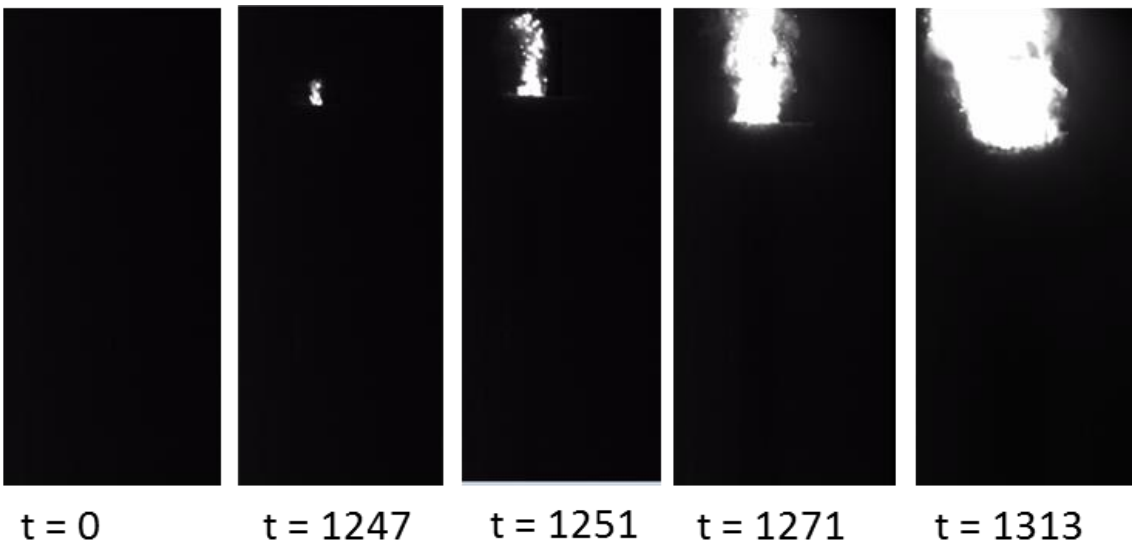

Figure 48 High-speed images of the ignition event for an aluminized APCP; note the time spacing was not the same between each frame. Aluminum can be seen leaving the surface of the propellant upon ignition, giving the flame a jagged appearance compared to Fig. 46.

The flame structure on the aluminized APCPs was observed to have aluminum particles that are burning and lifting off of the surface of the propellant strand upon ignition. A slower ignition time could also be from the aluminum having a higher ignition temperature than the AP, and since the aluminum conducts the heat away, it requires more time to reach the ignition temperature for the mixture. The flame appears to propagate at a slower rate than the non-aluminized formulation, but there was a noticeable presence of burning aluminum particles or agglomerates. Visually investigating the propellant as it burns also provides quality control with regards to the location of ignition.

7.2 Measurement Uncertainties

Ignition delay times contain error in their measurement based on several factors. The fist factor is the mechanical time to open and close the shutter. By using a mechanical shutter, the mirror used to reflect the laser beam causes the area of the beam to vary by the velocity of the shutter as it is opened or closed. In an effort to evaluate the opening and closing time of the shutter, a high-speed camera was used to record the motion of the shutter. The camera was placed in line with the mirror and recorded the opening and closing motion at 2000 frames per second. Figure 49 and Figure 50 show the motion of the shutter, providing the timing of the shutter closing and then opening using the automated control system. The opening and closing velocity of the shutter was determined from the high-speed video. Knowing the shutter velocity, the energy being blocked from the motion of the shutter could be calculated. An energy correction was calculated from the velocity of the shutter to the rate of change in the beam area. The relationship for area as given height from the bottom of a circle is given by Eq. 15.

$$A = r^2 \cos^{-1}\left(\frac{r-h}{r}\right) - (r-h)\sqrt{(2rh - h^2} \qquad (15)$$

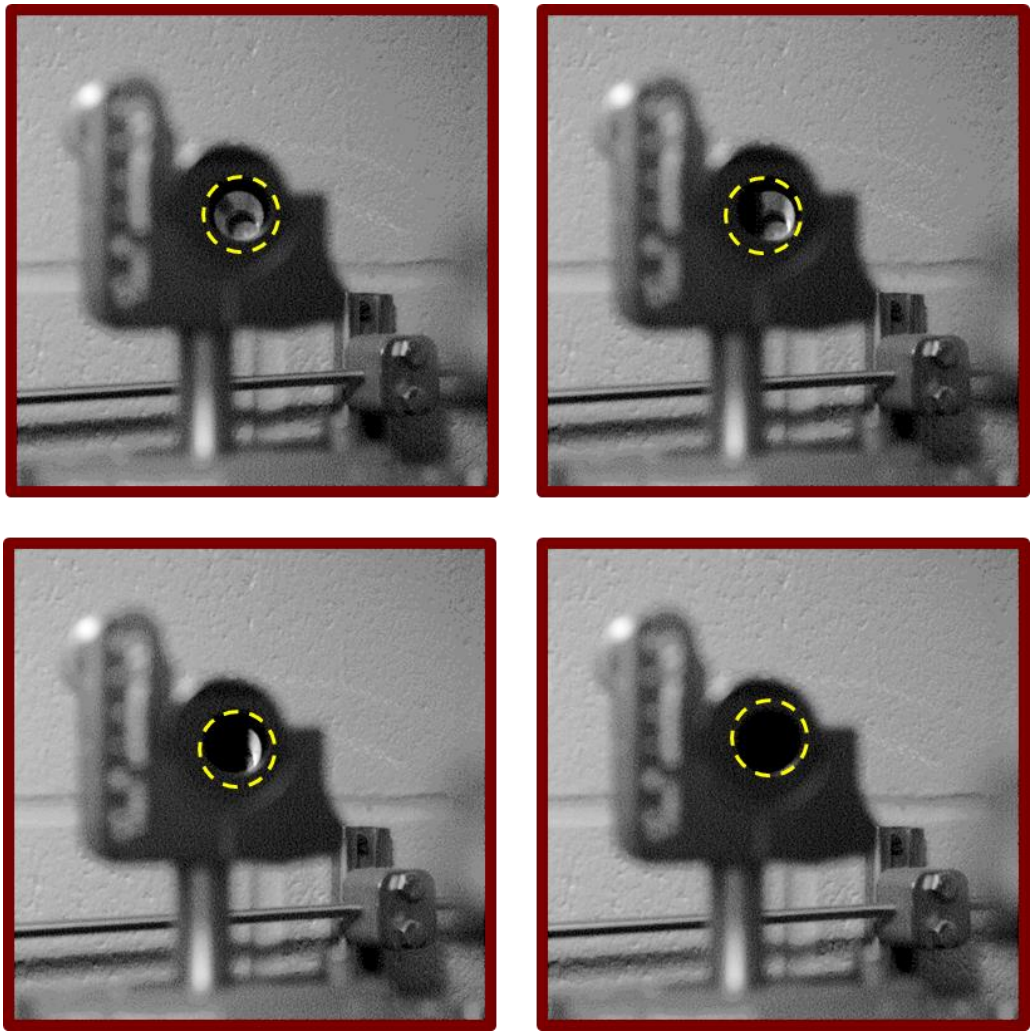

Figure 49 Shutter closing time; images taken at 0, 10, 30, and 41 ms.

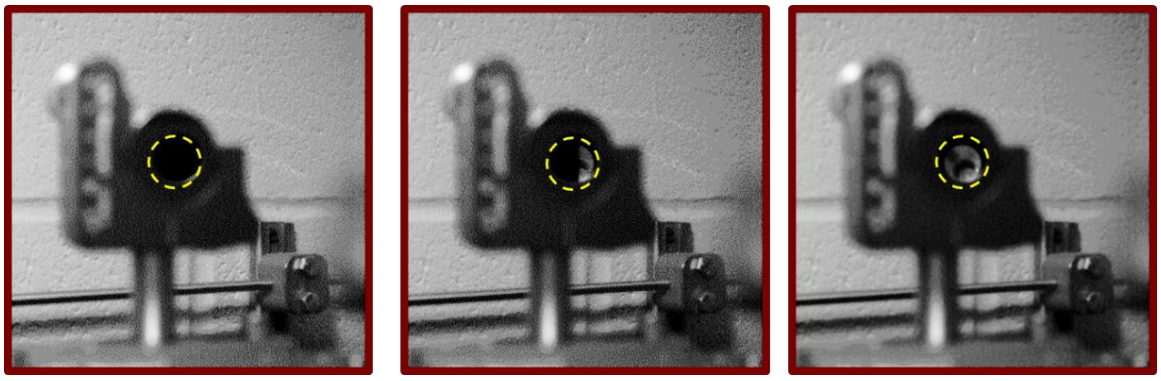

Figure 50 Shutter opening time; images taken at 0, 12, and 29 ms.

In an effort to narrow in on the exact time to ignition, at timer was set on the shutter to close based on a trend line fit of the data. This configuration proved to be difficult to test. When setting the timer, each sample tested would ignite at different times. It was thought that the oscillating ignition times is an artifact of inconstancies in testing the smaller propellant strands. Prior to testing, each sample is cut to a small size, and depending on how the sample was cut, there could be more or less AP exposed on the surface. Ignition is due to the AP absorption of the laser energy.

7.3 Discussion

A CO_2 laser ignition system was recently installed at Texas A&M University. Power calibration was performed to control the energy directed towards the propellant strand. Ignition delay time measurements were collected over a wide range of propellants, including a comparison of TiO_2 and Fe_2O_3 additives. Data collected matched well with available literature values; however, no group tested above 500 psi or at varied pressures. This study revealed a pressure dependence on the ignition delay times, not due to gas absorption, but to other suspected mechanisms.

A reliable method to evaluate the ignition delay time of solid propellant strands was created from this study. Evaluating the ignition delay time of the propellant strand provides information on the minimum ignition energy. Experimentally determining the minimum ignition energy provides data for propellant modelers to accurately predict the ballistics for a propellant formulation.

After incorporating various nano-additives, information on the catalytic properties can be derived. The titania was shown to have no effect on the ignition delay time of a non-aluminized AP/HTPB propellant sample. The amount of titania was 0.4% by weight, resulting in minimal changes in the thermal conductivity. Titania is known to aid in the HTD of AP, and the these tests confirm that titania participates in the reaction as a burning rate catalyst. By not altering the ignition delay time, it provides additional validation for titania catalyzing the high-temperature decomposition of AP. The drastic drop in the ignition delay time caused by the iron oxide was attributed to the idea that iron oxide is a strong low-temperature catalyst for AP. Ignition was initiated sooner since the iron oxide increased the decomposition rate of the AP, allowing more gaseous oxidizer radicals. However, the ignition time appeared to increase at the higher pressures. It is thought that the higher pressure is starting to leave the diffusion-limited domain to enter the kinetic-limited burning regime. In the diffusion-limited regime, increased production of the oxidizing gas provides higher quantities of oxidant to burn the fuel without the fuel needing to diffuse.

In the aluminized formulations, the baseline had a similar trend to the iron oxide. Aluminized formulations contain 16% aluminum, making the propellant strands much more conductive. The energy input by the laser had a higher thermal penetration in the propellant strand. As a result, it took longer to reach the ignition temperature, but the propellant strand had more preheating. Using catalysts altered the pressure dependence of the ignition delay time. This pressure dependence was attributed to the catalyst decomposing the AP, which followed the same pressure dependence as observed in the

non-aluminized propellants. The presence of the aluminum altered the thermal properties enough to lengthen the ignition delay time. Again, the iron oxide lowered the ignition delay time for the same reasons as in the non-aluminized propellants, but iron oxide is also used to combust the aluminum. Aluminum and iron oxide can both be used in thermite propellants, and the more drastic increase could be due to the iron oxide also burning the aluminum, which produces higher flame temperatures.

7.4 Recommendations

Improvements to the strand burner should be made to extend the life of the window. During the ignition testing, soot from the propellant is expelled from the surface and impacts the window. The soot causes pitting and other surface damage preventing the transmission of the laser. To remedy the pitting, a protective plastic, with high transmission at the 10.6 μm wavelength, was placed in front of the window. The plastic was mounted on a metal insert and placed against the window. A modification to suspend the plastic directly above the propellant strand was ultimately used to reduce the time between experiments. After running new experiments in nitrogen, not seen in this study, future testing should be done in nitrogen. The other tests performed in nitrogen produced data with lower scatter than the tests performed in argon.

The original intent was to obtain both burning rate and ignition delay time data from a single test. Both burning rate and ignition data were collected, but there is significantly more damage to the ZnS window when using a full sample. Recommendations would be to use smaller sample sizes, on the order of 0.25 g. The

smaller size provides the same ignition delay time data, but it decreases the potential for sample movement and increases the life of the laser window. To fully protect the ZnS window, a separate shutter should be assembled in the strand burner. The shutter would slide over the window, closing the optical port off from the combustion gases, once triggered. Triggering could be done off of the same light signal used to control the water-cooled laser shutter.

CHAPTER VIII

SUMMARY AND CONCLUSIONS

This thesis detailed the installation and procedure for two new propellant evaluation and experimental techniques. After performing a literature search on measurements and diagnostics of constant-volume strand burners, the need for the new analysis methods was identified. Now there is a method to compare the chemical combustion efficiency for identical propellant formulations, with the only alteration being in the particle synthesis process. Modifications were then made to the strand burner to incorporate laser ignition of any propellant strand. Using a laser to ignite a propellant strand provides accurate measurements of the ignition delay time and minimum ignition energy.

Using a constant-volume stand burner to evaluate the linear burning rate of a solid propellant strand was shown to be advantageous because of the pressure rise. Information on the chemical c* efficiency of a propellant mixture can be recorded by applying thermodynamic relationships to the pressure-rise data. This procedure was demonstrated by comparing the pressure trace generated from the propellants containing the various sizes of AP particles in the same propellant mixture ratios, by weight. The findings indicated that the propellant with the smaller AP reached a higher peak pressure. However, the difference between the 23- and 45-μm AP was negligible, indicative of transitioning from diffusion-limited to combustion-limited combustion. Losses due to AP packing effects were negligible since the propellant density remained

approximately the same over the various sizes tested. After studying the AP size effects, catalyst-manufacturing processes were tested.

It was determined that the additive synthesis technique is also a key factor in altering the combustion efficiency. All of the nano-titania particles examined were amorphous in structure, and previous studies indicate that they have the same thermodynamic and physical properties. By studying the nanoparticle synthesis techniques, it was concluded that the burning rate increase is coupled with an increased combustion efficiency from using the *in-situ* synthesis method.

A normalized pressure rise can be used to evaluate the combustion efficiency of other propellant additives. Future testing can be done by selecting a catalyst, then altering the synthesis process for the additive until the most complete combustion is found. The *in-situ* synthesis proved to be the best mixing method for nanoparticles, and titania proved to contribute to the optimal combustion efficiency for both the aluminized and non-aluminized propellant formulations. Repeating the same particle structure for iron oxide additive synthesis did not produce as complete combustion and still needs more work. Results from the model were scaled to closely approximate the combustion temperature of the product gases. Altering the iron oxide *in-situ* particle structure would likely produce results that are more desirable. Matching the predicted pressure to the pressure rise from the experiment was done by using the model and altering the flame temperature. The temperature changes calculated were determined to be reasonable approximations, and they provided an approximate quantitative increase in a chemical c* efficiency.

A repeatable method to evaluate the ignition delay time for both non-aluminized and aluminized APCPs was desired, and this goal was achieved. Ignition delay times of the propellants tested were evaluated over the pressure range of 500 psi (3.5 MPa) to 2250 psi (15.5 MPa), and the developed system can be applied to any future propellant mixes. The results comparing the laser power to the ignition delay time had similarmagnitudes to the data found in the literature, helping to validate both the developed method herein and the prior results. In general, a lower power setting produces more-reliable ignition delay times and limits the experiments to time scales on the order of hundreds of ms. Scatter was introduced from the shutter opening and closing times being on the order of 50 ms. Soot mitigation in the system was reduced because soot formation on the window was eliminated by replacing a protective film after each test. The power was set to a region where the finite shutter opening and closing speeds do not significantly affect the ignition delay time measurement. Non-aluminized APCP ignition delay times were found to be inversely dependent to the test pressure.

The addition of titania on the non-aluminized APCPs did not alter the ignition delay time of the propellant. Since the additive was only a small portion of the propellant (0.3% by mass), changes in the thermal conductivity were not noticeably altered. If the thermal conductivity were increased enough, the ignition delay time should be increased. Energy from the laser would be conducted away from the surface faster. More time would be required to ignite the sample due to the additional energy requirement. Titania did however increase the burning rate of the propellant, indicating that titania only participates as a catalyst in the high-temperature decomposition of AP.

However, the addition of the Fe_2O_3 decreased the ignition delay time of the non-aluminized propellant. The fraction of iron oxide in the propellant was the same as the titania and likewise produced negligible changes in the thermal conductivity. Since the iron oxide was added at the same loading as the titania, the results indicate that the iron oxide likely decomposes the AP with less energy than the titania. Fe_2O_3 is known to enhance the LTD of AP, which is thought to be the reason for the reduced ignition delay time. It can be concluded from the ignition studies that iron oxide aids in the LTD of AP, and titania aides in the HTD of AP.

In the baseline-aluminized propellants, the ignition delay time has a direct dependence on pressure, counter to what was observed for the non-aluminized samples. In the aluminized APCPs, the titania was found to invert the ignition delay time dependency on pressure, suggesting that the titania uses a different mechanism to catalyze the AP in an aluminized propellant. Our current theory is that the aluminum has a higher ignition temperature, which requires more energy absorption from the laser, but the aluminum conducts the heat away from the surface. By removing the heat from the surface, the propellant requires more time to ignite. A simplified heat transfer model of the system was created by solving the conduction equation for a 2-dimensional transient cylinder. The model generated a time history of the propellant strand, and ignition time was set to be the time step when the propellant reached its ignition temperature. Literature showed higher accuracy when setting the ignition point a few microns below the surface if phase change and chemical reactions were not included. This study set the ignition point to be 25-50 μm below the top surface. The model predicted similar

ignition delay times as the experimental values, giving additional validation to the experiments performed herein.

Future research should involve testing titania-containing propellants with a wider range of oxidizer mass loading and propellants manufactured in large-scale settings. Additionally, a more-thorough investigation into the effects of nano-additives with a low-temperature catalysis mechanism, as in the case with Fe_2O_3 should be performed. Catalysts which are more effective at lower temperatures are thought to decrease the ignition delay time since they speed up the initial decomposition of the solid AP. Investigating the effects of aging on the propellant ignition delay time was also of interest, since the propellant is deteriorating, thus altering the propellant properties. Additionally, there exists the potential for future research into alternative metal-oxide additives containing atomically doped titania synthesized via the nano-assembly method in an effort to tailor the ignition delay times as desired. Doping titania with iron could lead to lower ignition energies by forcing titania to participate in the LTD because of the iron.

REFERENCES

[1] Thomas, J. C., Demko, A. R., Sammet, T. E., Reid, D. L., Seal, S., and Petersen, E. L. "Mechanical Properties of Composite AP/HTPB Propellants Containing Novel Titania Nanoparticles," *Propellants, Explosives, Pyrotechnics* Vol. 41, No. 5, 2016, pp. 822-834.

[2] Sutton, G. P., and Biblarz, O. *Rocket Propulsion Elements*, 8th edition, John Wiley & Sons Inc., Hoboken, New Jersy, 2010.

[3] Jeppson, M. B., Beckstead, M., and Jing, Q. "A Kinetic Model for the Premixed Combustion of a Fine Ap/Htpb Composite Propellant," *AIAA 36th Aerospace Sciences Meeting and Exhibit*. 1998.

[4] Davenas, A. "Development of Modern Solid Propellants," *Journal of Propulsion and Power* Vol. 19, No. 6, 2003, pp. 1108-1128.

[5] Masala, O., and Seshadri, R. "Synthesis Routes for Large Volumes of Nanoparticles," *Annu. Rev. Mater. Res.* Vol. 34, 2004, pp. 41-81.

[6] Meda, L., Marra, G., Galfetti, L., Inchingalo, S., Severini, F., and De Luca, L. "Nano-Composites for Rocket Solid Propellants," *Composites Science and Technology* Vol. 65, No. 5, 2005, pp. 769-773.

[7] Blomshield, F., Nguyen, S., Matheke, H., Atwood, A., and Bui, T. "Acoustic Particle Damping of Propellants Containing Ultra-Fine Aluminum," *40th AIAA/ASME/SAE/ASEE Joint Propulsion Conference and Exhibit*. 2004, p. 372.

[8] Dokhan, A., Price, E., Seitzman, J., and Sigman, R. "Combustion Mechanisms of Bimodal and Ultra-Fine Al in Ap Solid Propellants," *38th AIAA/ASME/SAE/ASEE Joint Propulsion Conference & Exhibit*. 2002, p. 4173.

[9] Reid, D. L., Russo, A. E., Carro, R. V., Stephens, M. A., LePage, A. R., Spalding, T. C., Petersen, E. L., and Seal, S. "Nanoscale Additives Tailor Energetic Materials," *Nano Lett.* Vol. 7, 2007, p. 2157.

[10] Egdell, R. G., and Jones, F. H. "Structure and Reactivity of Oxide Surfaces: New Perspectives from Scanning Tunnelling Microscopy," *Journal of Materials Chemistry* Vol. 8, No. 3, 1998, pp. 469-484.

[11] Wang, Y., Zhu, J., Yang, X., Lu, L., and Wang, X. "Preparation of NiO Nanoparticles and Their Catalytic Activity in the Thermal Decomposition of

Ammonium Perchlorate," *Thermochimica Acta* Vol. 437, No. 1, 2005, pp. 106-109.

[12] Jacobs, P. W. M., and Whitehead, H. "Decomposition and Combustion of Ammonium Perchlorate," *Chemical Reviews* Vol. 69, No. 4, 1969, pp. 551-590.

[13] Lang, A. J., and Vyazovkin, S. "Effect of Pressure and Sample Type on Decomposition of Ammonium Perchlorate," *Combustion and Flame* Vol. 145, No. 4, 2006, pp. 779-790.

[14] Demko, Andrew R., Allen, Tyler W., Thomas, James C., Johnson, M., Morrow, Gordon R., Reid, David L., Seal, S., and Petersen, Eric L. "Comparison of Commercially Available and Synthesized Titania Nano-Additives in Composite AP/HTPB Propellant," *Propellants, Explosives, Pyrotechnics*, Vol. 42, No. 2, 2017, pp. 158-166.

[15] Kreitz, K. R., Petersen, E., Reid, D., and Sudipta, S. "Relative Dispersion of Catalytic Nanoparticle Additives and Ap Particles in Composite Solid Propellant and the Effect on Burning Rate," *49th AIAA Aerospace Sciences Meeting including the New Horizons Forum and Aerospace Exposition*. Vol. AIAA 2011-418, American Institute of Aeronautics and Astronautics, Orlando, FL, 2011.

[16] Frazier, C. "Modeling Solid Propellant Strand Burner Experiments with Catalytic Additives," Ph.D. Dissertation, *Mechanical Engineering*. Texas A&M University, College Station, TX, 2011.

[17] Reid, D. L., Draper, R., Richardson, D., Demko, A., Allen, T., Petersen, E. L., and Seal, S. "*In-Situ* Synthesis of Polyurethane-TiO_2 Nanocomposite and Performance in Solid Propellants," *Journal of Materials Chemistry A* Vol. 2, No. 7, 2014, pp. 2313-2322.

[18] Kreitz, K. R. "Catalytic Nanoparticle Additives in the Combustion of Ap/Htpb Composite Solid Propellant," MS Thesis, *Mechanical Engineering*. Texas A&M University, College Station, TX, 2010.

[19] Li, W., and Cheng, H. "Cu–Cr–O Nanocomposites: Synthesis and Characterization as Catalysts for Solid State Propellants," *Solid State Sciences* Vol. 9, No. 8, 2007, pp. 750-755.

[20] Reid, D. L., Kreitz, K. R., Stephens, M. A., King, J. E. S., Nachimuthu, P., Petersen, E. L., and Seal, S. "Development of Highly Active Titania-Based Nanoparticles for Energetic Materials," *The Journal of Physical Chemistry C* Vol. 115, No. 21, 2011, pp. 10412-10418.

[21] Demko, A. R., Dillier, C. A., Morrow, G. R., Sammet, T., Grossman, K., Seal, S., and Petersen, E. L. "Laboratory-Scale Burning of Composite Solid Propellant Using in-Situ Synthesized Iron Oxide," *52nd AIAA/SAE/ASEE Joint Propulsion Conference*. 2016, p. 5115.

[22] Crawford Jr, B. L., Huggett, C., Daniels, F., and Wilfong, R. "Direct Determination of Burning Rates of Propellant Powders," *Analytical Chemistry* Vol. 19, No. 9, 1947, pp. 630-633.

[23] Kubota, N., Ichidat, M., and Fujisawa, T. "Combustion Processes of Propellants with Embedded Metal Wires," *AIAA Journal* Vol. 20, No. 1, 1982, pp. 116-121.

[24] Son, S., Berghout, H., Bolme, C., Chavez, D., Naud, D., and Hiskey, M. "Burn Rate Measurements of Hmx, Tatb, Dht, Daaf, and Btatz," *Proceedings of the Combustion Institute* Vol. 28, No. 1, 2000, pp. 919-924.

[25] Kohga, M. "Burning Characteristics and Thermochemical Behavior of Ap/Htpb Composite Propellant Using Coarse and Fine Ap Particles," *Propellants, Explosives, Pyrotechnics* Vol. 36, No. 1, 2011, pp. 57-64.

[26] Luman, J., Wehrman, B., Kuo, K., Yetter, R., Masoud, N., Manning, T., Harris, L., and Bruck, H. "Development and Characterization of High Performance Solid Propellants Containing Nano-Sized Energetic Ingredients," *Proceedings of the Combustion Institute* Vol. 31, No. 2, 2007, pp. 2089-2096.

[27] Juhasz, A., and Price, C. F. "The Closed Bomb Technique for Burning Rate Measurement at High Pressure," *AIAA Journal*, 1977, pp. 129-151.

[28] Atwood, A., Ford, K., and Wheeler, C. "High-Pressure Burning Rate Studies of Solid Rocket Propellants." DTIC Document, 2013.

[29] Atwood, A., Curran, P., Price, C., Boggs, T., and Booth, D. "High Pressure Burning Rate Studies of Ammonium Perchlorate (AP) Based Propellants," *The Applied Vehicle Technology Panel, AGARD Spring Meeting on Aging Systems: Small Rocket Motor and Gas Generators. Corfu*, Greece. 1999.

[30] Celminš, A. "Solid Propellant Burning Rate Measurement in a Closed Bomb," *Combustion and Flame* Vol. 23, No. 3, 1974, pp. 381-397, doi.

[31] Celmins, A. "Solid Propellant Burning Rate Measurement in a Closed Bomb." DTIC Document, 1975.

[32] Price, C., and Juhasz, A. "A Versatile User-Oriented Closed Bomb Data Reduction Program (CBRED)." Army Ballistic Research Lab Aberdeen Proving Ground Md, Army Ballistic Research Lab Aberdeen Proving Ground MD, 1977.

[33] Glick, R., and Hepler, S. "On the Reduction of High Pressure Ballistic Data," *22nd Joint Propulsion Conference*. American Institute of Aeronautics and Astronautics, Huntsville, AL, 1986.

[34] Robert, G., and Daniel, H. "An Improved Closed Burner Method," *26th Joint Propulsion Conference*. American Institute of Aeronautics and Astronautics, 1990.

[35] Gordon, S., and McBride, B. J. *Computer Program for Calculation of Complex Chemical Equilibrium Compositions and Applications*: Citeseer, 1996.

[36] McBride, B. J., and Gordon, S. "Computer Program for Calculation of Complex Chemical Equilibrium Compositions and Applications Ii. Users Manual and Program Description. 2; Users Manual and Program Description," 1996.

[37] Gordon, S., and McBride, B. J. "Computer Program for Calculation of Complex Chemical Equilibrium Compositions and Applications. Part 1: Analysis," 1994.

[38] Yilmaz, N., Donaldson, B., Gill, W., and Erikson, W. "Solid Propellant Burning Rate from Strand Burner Pressure Measurement," *Propellants, Explosives, Pyrotechnics* Vol. 33, No. 2, 2008, pp. 109-117.

[39] Frazier, C., Demko, A., and Petersen, E. "Modeling Composite Solid Propellant with Catalytic Additives," *51st AIAA Aerospace Sciences Meeting including the New Horizons Forum and Aerospace Exposition*. Vol. AIAA 2013-0820, Grapevine, TX, 2013.

[40] Granier, J. J., Mullen, T., and Pantoya, M. L. "Nonuniform Laser Ignition in Energetic Materials," *Combustion Science and Technology* Vol. 175, No. 11, 2003, pp. 1929-1951.

[41] Meredith, K. V., Gross, M. L., and Beckstead, M. W. "Laser-Induced Ignition Modeling of Hmx," *Combustion and Flame* Vol. 162, No. 2, 2015, pp. 506-515.

[42] Cain, J., and Brewster, M. Q. "Radiative Ignition of Fine-Ammonium Perchlorate Composite Propellants," *Propellants, Explosives, Pyrotechnics* Vol. 31, No. 4, 2006, pp. 278-284.

[43] Zanotti, C., and Giuliani, P. "Composite Propellant Ignition and Extinction by Co2 Laser at Subatmospheric Pressure," *Propellants, Explosives, Pyrotechnics* Vol. 23, No. 5, 1998, pp. 254-259.

[44] Boggs, T., Price, C., Atwood, A., Zurn, D., Eisel, J., and Derr, R. "The Role of Gas Phase Reactions in the Deflagration-to-Detonation Transition of High Energy Propellants," 1980.

[45] Arkhipov, V. A., and Korotkikh, A. G. "The Influence of Aluminum Powder Dispersity on Composite Solid Propellants Ignitability by Laser Radiation," *Combustion and Flame* Vol. 159, No. 1, 2012, pp. 409-415.

[46] Ali, A., Son, S., Asay, B., Decroix, M., and Brewster, M. "High-Irradiance Laser Ignition of Explosives," *Combustion Science and Technology* Vol. 175, No. 8, 2003, pp. 1551-1571.

[47] Atwood, A., Ford, K., Bui, D., Curran, P., and Lyle, T. "Radiant Ignition Studies of Ammonium Perchlorate Based Propellants," *Progress in Propulsion Physics*. Vol. 1, EDP Sciences, 2009, pp. 121-140.

[48] Kim, J. H., Ahn, J. Y., Park, H. S., and Kim, S. H. "Optical Ignition of Nanoenergetic Materials: The Role of Single-Walled Carbon Nanotubes as Potential Optical Igniters," *Combustion and Flame* Vol. 160, No. 4, 2013, pp. 830-834.

[49] Stephens, M., Petersen, E., Carro, R., Reid, D., and Seal, S. "Multi-Parameter Study of Nanoscale TiO_2 and CeO_2 Additives in Composite AP/HTPB Solid Propellants," *Propellants, Explos., Pyrotech.* Vol. 35, 2010, p. 143, doi.

[50] DeLuca, L., Ohlemiller, T., Caveny, L., and Summerfield, M. "Radiative Ignition of Double Base Propellants. Ii-Pre-Ignition Events and Source Effects," *AIAA Journal* Vol. 14, No. 8, 1976, pp. 1111-1117.

[51] Fujimura, K., and Miyake, A. "Effect of the Particle Size and Specific Surface Area of Ferric Oxide Catalyst on the Burning Rate of AP/HTPB Solid Propellant," *Science and Technology of Energetic Materials* Vol. 71, No. 3-4, 2010, pp. 65-69.

[52] Kokobeinichev, O. P., Anisiforov, G. I., and Tereschenko, A. G. "High-Temperature Decomposition of Ammonium Perchlorate-Polystyr Ene-Catalyst Mixtures," *AIAA Journal* Vol. 13, No. 5, 1975, pp. 628-633.

[53] Carro, R. V. "High Pressure Testing of Composite Solid Rocket Propellant Mixtures: Burner Facility Characterization," MS Thesis, *Mechanical Engineering*. University of Central Florida, Orlando, Florida, 2007.

[54] Demko, A. R., Dillier, C., Petersen, E. L., Reid, D., and Seal, S. "Ignition Delay Times of Composite Solid Propellants Using Novel Nano-Additive Catalysts," *51st AIAA/SAE/ASEE Joint Propulsion Conference*. Vol. AIAA 2015-4106, Orlando, FL, 2015.

[55] Stacy, S. C., and Pantoya, M. L. "Laser Ignition of Nano-Composite Energetic Loose Powders," *Propellants, Explosives, Pyrotechnics* Vol. 38, No. 3, 2013, pp. 441-447.

[56] Cohen, A., and Beyer, R. A. "Laser Ignition of Solid Propellents: Ignition Delays." Vol. ARL-TR-162, Army Research Laboratory Aberdeen, MD, 1993.

[57] Demko, A. R., and Petersen, E. L. "Development of a Co2 Laser Ignition System to Test Solid Propellant Strands," *Central States Combustion Institute Meeting,*, Tulsa, OK, Month, 2014.

[58] Harris, D. C. *Materials for Infrared Windows and Domes: Properties and Performance*: SPIE press, 1999.

[59] Villars, D. "A Method of Successive Approximations for Computing Combustion Equilibria on a High Speed Digital Computer," *The Journal of Physical Chemistry* Vol. 63, No. 4, 1959, pp. 521-525.

[60] Browne, H. N., Jr.,, Williams, M. W., and Cruise, D. R. *The Theoretical Computation of Equilibrium Compositions, Thermodynamic Properties and Performance Characteristics of Propellant Systems*. 1960.

[61] Cruise, D. "Theoretical Computations of Equilibrium Compositions, Thermodynamic Properties, and Performance Characteristics of Propellant Systems." DTIC Document, 1979.

[62] Glassman, I., Yetter, R. A., and Glumac, N. G. *Combustion*: Academic press, 2014.

[63] Turns, S. R. *An Introduction to Combustion*: McGraw-hill New York, 1996.

[64] Korobeinichev, O., Ermolin, N., Chernov, A., and Emel'yanov, I. "Flame Structure, Kinetics and Mechanism of Chemical Reactions in Flames of Mixed Composition Based on Ammonium Perchlorate and Polybutadiene Rubber," *Combustion, Explosion and Shock Waves* Vol. 28, No. 4, 1992, pp. 366-371.

[65] Kee, R. J., Rupley, F. M., and Miller, J. A. "The Chemkin Thermodynamic Data Base," *Unknown* Vol. 1, 1990.

[66] McBride, B. J., Zehe, M. J., and Gordon, S. "Nasa Glenn Coefficients for Calculating Thermodynamic Properties of Individual Species," 2002.

[67] Moran, M. J., Shapiro, H. N., Boettner, D. D., and Bailey, M. B. *Fundamentals of Engineering Thermodynamics*: John Wiley & Sons, 2010.

[68] Bradley, D., and Mitcheson, A. "Mathematical Solutions for Explosions in Spherical Vessels," *Combustion and Flame* Vol. 26, 1976, pp. 201-217.

[69] Bradley, D., and Mitcheson, A. "The Venting of Gaseous Explosions in Spherical Vessels. Ii—Theory and Experiment," *Combustion and Flame* Vol. 32, 1978, pp. 237-255.

[70] Bradley, D., and Mitcheson, A. "The Venting of Gaseous Explosions in Spherical Vessels. I—Theory," *Combustion and Flame* Vol. 32, 1978, pp. 221-236, doi.

[71] Bergman, T. L., and Incropera, F. P. *Introduction to Heat Transfer*: John Wiley & Sons, 2011.

[72] Atwood, A., Boggs, T., Curran, P., Parr, T., Hanson-Parr, D., Price, C., and Wiknich, J. "Burning Rate of Solid Propellant Ingredients, Part 1: Pressure and Initial Temperature Effects," *Journal of Propulsion and Power* Vol. 15, No. 6, 1999, pp. 740-747.

[73] Beckstead, M. W., Derr, R. L., and Price, C. F. "A Model of Composite Solid-Propellant Combustion Based on Multiple Flames," *AIAA Journal* Vol. 8, No. 12, 1970, pp. 2200-2207.

[74] Kubota, N. *Propellants and Explosives: Thermochemical Aspects of Combustion*: John Wiley & Sons, 2015.

[75] Jing, Q., Beckstead, M., and Jeppson, M. "Influence of Ap Solid Phase Decomposition on Temperature Profile and Sensitivity," *AIAA paper* Vol. 448, 1998, p. 1998.

[76] Meyer, R. *Explosives*. New York: VCH Publishers, , 1986.

[77] Arisawa, H., and Brill, T. "Flash Pyrolysis of Hydroxyl-Terminated Polybutadiene (Htpb) I: Analysis and Implications of the Gaseous Products," *Combustion and Flame* Vol. 106, No. 1, 1996, pp. 131-143.

[78] Parr, T., and Hanson-Parr, D. "Solid Propellant Diffusion Flame Structure," *Symposium (International) on Combustion*. Vol. 26, Elsevier, 1996, pp. 1981-1987.

[79] Stephens, H., Brandrup, J., and Immergut, E. "'Physical Constants of Poly (Butadiene)," *Polymer Handbook, 3rd edition, J. Brandup, EH Immergut, Eds., J. Wiley & Sons, New York*, 1989, p. V1.

[80] Tanner, M. W. *Multidimensional Modeling of Solid Propellant Burning Rates and Aluminum Agglomeration and One-Dimensional Modeling of Rdx/Gap and Ap/Htpb*: ProQuest, 2008.

[81] Morrow, G. "The Effects of Ap Particle Size and Concentration on AP/HTPB Composite Propellant Burning Rates," Masters, *Mechanical Engineering*. Texas A&M Univeristy, College Station, TX, 2017.

[82] Morrow, G. R., and Petersen, E. L. "The Effects of Ap Particle Size and Concentration on AP/HTPB Composite Propellant Burning Rates," *55th AIAA Aerospace Sciences Meeting*. 2017, p. 0831.

[83] Allen, T., Demko, A., Johnson, M., Sammet, T., Petersen, E., Reid, D., Draper, R., and Seal, S. "Laboratory-Scale Burning of Composite Solid Propellant for Studying Novel Nanoparticle Synthesis Methods," *51st AIAA Aerospace Sciences Meeting including the New Horizons Forum and Aerospace Exposition*. Vol. AIAA 2013-0821, Grapevine, TX, 2013.

[84] Stephens, M., Sammet, T., Carro, R., LePage, A., and Petersen, E. "Comparison of Hand and Mechanically Mixed AP/HTPB Solid Composite Propellants," *43rd AIAA/ASME/SAE/ASEE Joint Propulsion Conference & Exhibit*. Cincinnati, OH., 2007.

[85] Hu, S., Chen, J., Wu, G., Xu, Q., Liu, H., and Hua, Y. "Burning Behavior of Solid Propellants at High Pressure," *Combustion Science and Technology* Vol. 186, No. 12, 2014, pp. 1858-1888, doi.

[86] Smyth, D. A. "Modeling Solid Propellant Ignition Events," 2011.

[87] Qin, Z., Tang, Y., Paravan, C., Colombo, G., Shen, R., and DeLuca, L. T. "Ignition of Htpb-Based Fuels Loaded with and without Micron-Sized Metals," 2015.

[88] Shannon, L. J. "Composite Solid-Propellant Ignition by Radiant Energy," *AIAA Journal* Vol. 8, No. 2, 1970, pp. 346-353.

[89] Hermance, C. E., Shinnar, R., and Summerfield, M. "Ignition of an Evaporating Fuel in a Hot, Stagnant Gas Containing an Oxidizer," *AIAA Journal* Vol. 3, No. 9, 1965, pp. 1584-1592.

[90] McAlevy III, R. F. "The Ignition Mechanism of Composite Solid Propellants." DTIC Document, 1961.

[91] Fujimura, K., and Miyake, A. *J. Therm. Anal. Calorim.* Vol. 99, No. null, 2009, p. 27.

[92] Nandi, A., Pant, A., Tripathi, A., Newale, S., Gajbhiye, V., Jadhav, A., Khopade, R., Prasanth, H., Pandey, R. K., and Bhattacharya, B. "Large Scale Synthesis and Characterization of A-Fe_2O_3 Nanoparticles for Propellant Applications," *Advanced Nanomaterials and Emerging Engineering Technologies (ICANMEET), 2013 International Conference on*. IEEE, 2013, pp. 475-480.

[93] Beckstead, M. W., Boggs, T. L., and Derr, R. L. "Surface Structure of Ammonium Perchlorate Composite Propellants," *AIAA Journal* Vol. 8, No. 2, 1970, pp. 370-372.

[94] Derr, R. L., and Boggs, T. L. "Role of Scanning Electron Microscopy in the Study of Solid Propellant Combustion:* Part III. The Surface Structure and Profile Characteristics of Burning Composite Solid Propellants," *Combustion Science and Technology* Vol. 1, No. 5, 1970, pp. 369-384.

[95] Sofue, T., and Iwama, A. "Ignition of Composite Propellant at Subatmospheric Pressures by Means of Carbon Dioxide Laser," *Propellants, Explosives, Pyrotechnics* Vol. 4, No. 5, 1979, pp. 98-106.

APPENDIX A-ZNSE WINDOW MOUNT

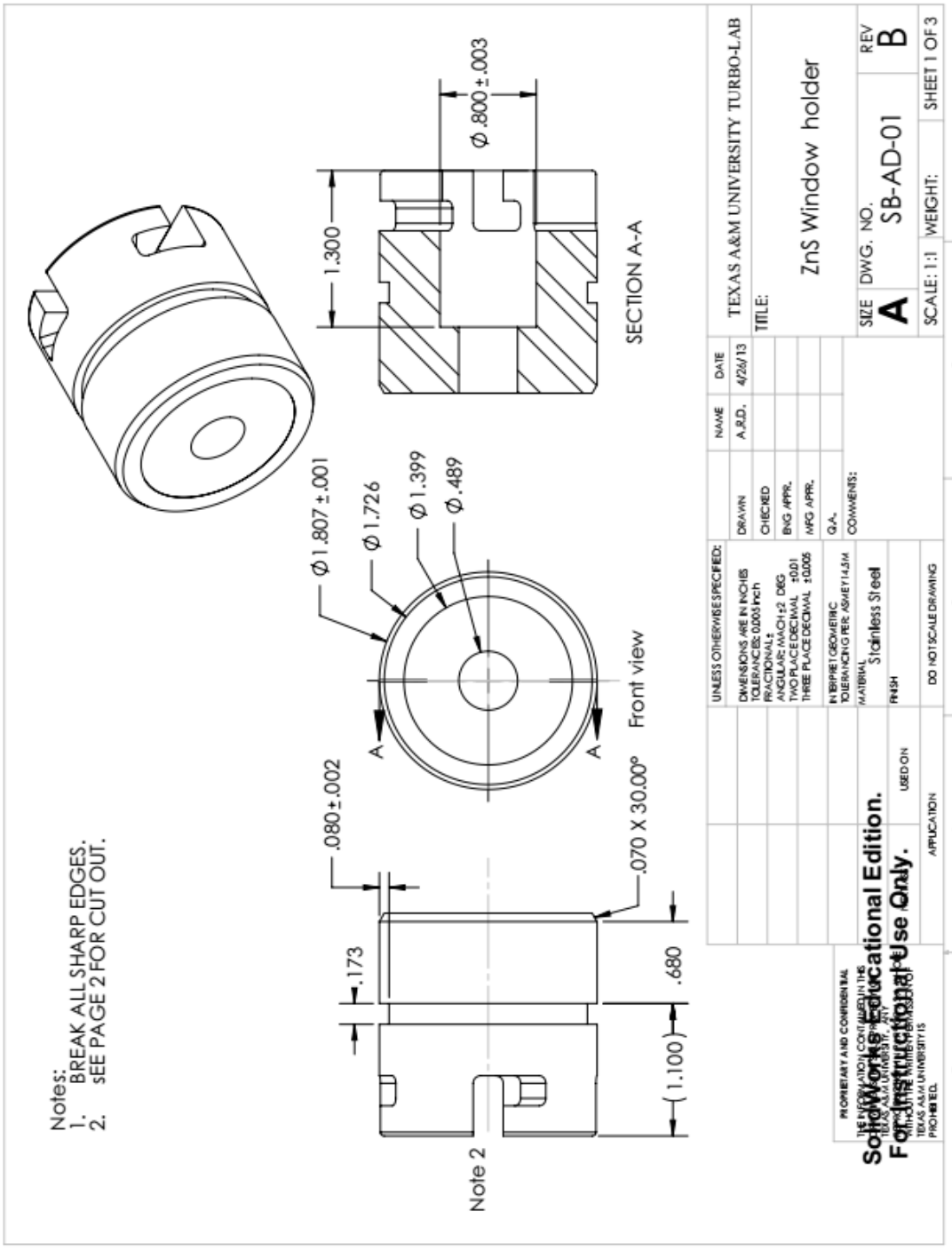

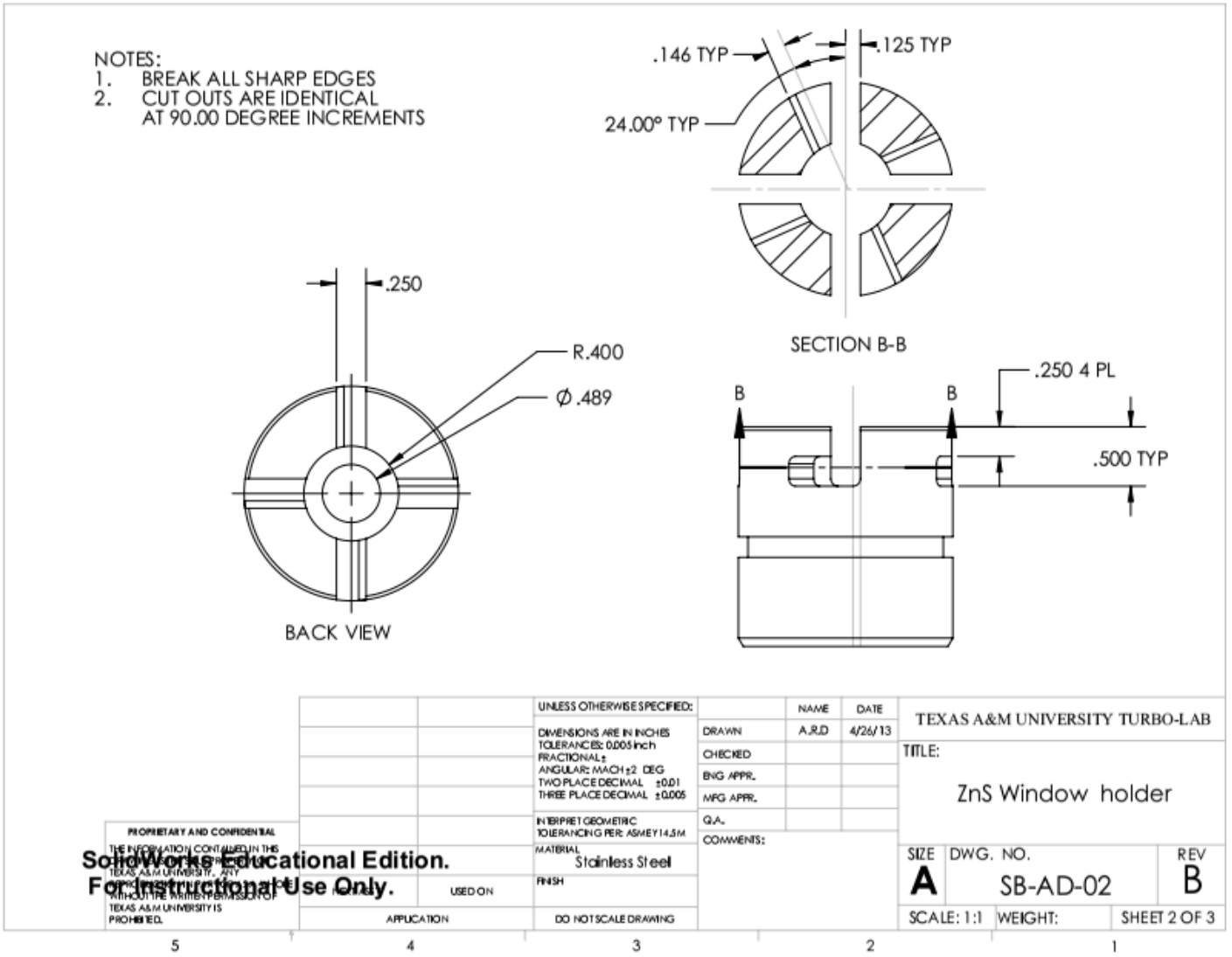

NOTES:
1. BREAK ALL SHARP EDGES
2. CUT OUTS ARE IDENTICAL AT 90.00 DEGREE INCREMENTS

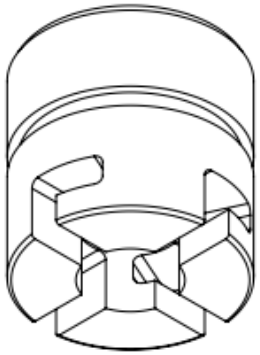

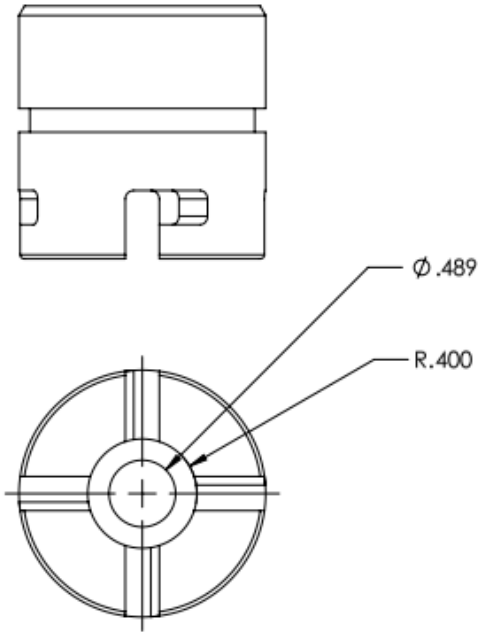

BACK VEW

UNLESS OTHERWISE SPECIFIED:		NAME	DATE	TEXAS A&M UNIVERSITY TURBO-LAB	
DIMENSIONS ARE IN INCHES TOLERANCES: 0.005 inch FRACTIONAL ± ANGULAR: MACH ±2 DEG TWO PLACE DECIMAL ±0.01 THREE PLACE DECIMAL ±0.005	DRAWN	A.R.D	4/26/13	TITLE: ZnS Window holder	
	CHECKED				
	ENG APPR.				
	MFG APPR.				
INTERPRET GEOMETRIC TOLERANCING PER: ASME Y14.5M	Q.A.				
MATERIAL: Stainless Steel	COMMENTS:			SIZE: A	DWG. NO.: SB-AD-02
FINISH				SCALE: 1:1	WEIGHT:
DO NOT SCALE DRAWING				REV: B	SHEET 3 OF 3

5 4 3 2 1

APPENDIX B-PRESSURE RISE MODEL

```
%Pressure rise model to predict the change in pressure of a propellant
%strand burned in a constant-volume strand burner. Model used to
validate
%the theory of higher combustion efficiency of various synthesis
techniques
%of catalytic additive. The model fist confirms the results from the
ideal
%mixing. Then the model compares the new 2-volume system followed by
the
%inclusion of heat transfer. The final modification is to incorporate
mass
%transfer.
%Author: Andrew R. Demko

timestep = 100;
R_u = 8314; %J/K-kmol
%% Inputs- Take values from burn log and ProPEP and input into the
matrix
mass =
leng =
burn =
intP =
finP =
molwe =
GAM =
nummol =
Tafp =
%% Propellant Test Characteristics
m_p = mass/1000;  % Mass of propellant, converted to kg
L_p = leng * 0.0254; % Propellant length, Converted to m
r_b = burn * 0.0254;  %Burning rate, converted form in/s to m/s
m_dot_r = m_p.* r_b./L_p; %Mass flow rate
t_b = L_p./r_b;          %Burn time
delt = t_b./timestep;    %Time step vector
V_pr = (0.1875/2*0.0254)^2*pi*(L_p*0.0254);  %Propellant Volume

%% Strand Burner Parameters
V_cv = 1.145/1000;    %Volume of strand burner m^3
P_ci = intP*6894.76; %Initial Volume converted from psi to MPa
P_cf = finP *6894.76; %Final  Volume converted from psi to MPa
TestP = (finP+intP)/2; %Average test Pressure psi
dP = (P_cf-P_ci)/6894.76;  %Pressure rise
T_cvi = 298;      %Argon Initial Temperature K

%% Argon Parameters
M_ar = 39.948;   %Molecular Weigth kg/kmol
R_ar = R_u / M_ar;  %J/kg-K
m_ar = P_ci.*V_cv./(R_ar.*T_cvi);  %kg
N_ar = m_ar./M_ar;  %moles
Cp_ar = 523; %J/kg-K
```

```
Cv_ar = Cp_ar- R_ar;

%% ProPEP Values
M_p = molwe;   %Molecular Weigth kg/kmol
R_p = R_u./ M_p;  %J/kg-K
gamma_p = GAM;
N_p = nummol;  %moles
Cp_p = R_p.*(gamma_p./(gamma_p-1)); %J/kg-K
Cv_p = Cp_p- R_p;   %J/kg-K
T_af = Tafp; %Adiabatic Flame Temperature (K)
h_p = Cp_p.*T_af;

%% Steady State Mixture Caluculations (1 Volume)
M_cv = (N_ar.*M_ar + N_p.*M_p)./(N_ar + N_p);
N = N_p + N_ar;
R_cvf = R_u./M_cv;
Cp_cv = (m_ar.*Cp_ar + m_p.*Cp_p)./(m_ar + m_p);
% Cp_cv = (N_ar.*Cp_ar + N_p.*Cp_p)./(N_ar + N_p);
Cv_cv = Cp_cv - R_cvf;
T_cvf = (m_p.*Cp_p.*T_af + m_ar.*Cv_ar.*T_cvi)./((m_ar+m_p).*Cv_cv);
P_cvf = ((m_ar+m_p).*R_cvf.*T_cvf)./V_cv;
P_cvfpsi = P_cvf /6894.76;
P_cvm = (P_cvfpsi-intP)./(m_p*1000);

%% Steady Stated Calculation 2-Volume Piston\
%Slope factor
mag = 1.1;
slo = 1.0;
% Argon
P_a1 = P_ci;
V_a1 = V_cv/mag;
T_a1 = T_cvi;
m_a1 = m_ar;

% Propellant
V_p1 = V_pr;
% V_p1 = V_pr*0.0254^3;%-(V_cv-V_a1/slo);
% V_p1 = (V_cv-V_a1);
T_p1 = T_af;
m_p1 = m_p;
P_p1 = m_p1.*R_p.*T_p1./V_p1;

% Equilibrating pressure in the Piston system
mu = 1*(m_p1.*R_p.*T_p1)./(m_a1.*R_ar.*T_a1);
dV = (V_a1.*mu-V_p1)./(mu+1);
P_p2 = m_p1.*R_p.*T_p1./(V_p1+dV);
P_p2psi = P_p2/6894.76;
dP_2v = (P_p2-P_ci)/6894.76;
dP_m = dP_2v./(m_p*1000);   %Model prediction of Pressure rise per mass
DP_m = dP./(m_p*1000);      %Experimental data of Pressure rise per
mass
```

```
%% Work Done on the Argon
W = Pavg.*dV*1;          %Work done by thr propellant on the argon
T_p2 = T_p1 - W./Cv_p;
T_aw2 = T_a1 + W./Cv_ar;
% Re equilibrate for the dV and final Pressure
muh = 1*(m_p1.*R_p.*T_p2)./(m_a1.*R_ar.*T_aw2);
dVh = (V_a1.*muh-V_p1)./(muh+1);
% dVh = (V_a1.*m_p1.*R_p.*T_p2-
V_p1.*m_a1.*R_ar.*T_aw2)./(m_p1.*R_p.*T_p2+m_a1.*R_ar.*T_aw2);
P_p2h = m_p1.*R_p.*T_p2./(V_p1+dVh);
P_p2psih = P_p2h/6894.76;  % units in psi
dP_2vh = (P_p2h-P_ci)/6894.76;
dP_mh = dP_2vh./(m_p*1000); %Model prediction of Pressure rise per mass
w/HT

pressure=dP_mh-dP_m
argon = T_aw2-T_a1
Propellant = T_p2-T_p1
ddVV = dVh-dV
% Update the 2-volume value
dP_2v = dP_2vh;
dP_m = dP_mh;   %Model prediction of Pressure rise per mass
Vtot  = V_p1 +V_a1;
Vprop = (V_p1+ dVh)./Vtot;
Varg  = (V_a1- dVh)./Vtot;
b = sort(intP,'ascend');
[Vo1,agoVo1] = fit(intP',Vprop','power1');   %Propelant fit
[Vo2,agoVo2] = fit(intP',Varg','power1');   % Argon Fit
% figure(7)
% semilogx(b, Vo1(b), b, Vo2(b))
% xlim([500 2500])
% legend('Propellant', 'Argon','location', 'best')
% xlabel('Test pressure (psig)')
% ylabel('Volume Change (%)')

%% Heat Transfer
% dT_ar = 3.4;              %Temperature change based on experimental
values
% T_a2 = T_a1+dT_ar;
% Q = Cv_ar.*dT_ar;          %Heat transfer from Propellant gas to Ar
% T_p2 = T_p1-1*Q./Cv_p;
%
% muh = 1*(m_p1.*R_p.*T_p2)./(m_a1.*R_ar.*T_a2);
% dVh = (V_a1.*muh-V_p1)./(muh+1);
% P_p2h = m_p1.*R_p.*T_p2./(V_p1+dVh);
% P_p2psih = P_p2h/6894.76;  % units in psi
% dP_2vh = (P_p2h-P_ci)/6894.76;
% dP_mh = dP_2vh./(m_p*1000); %Model prediction of Pressure rise per
mass w/HT


%% Mass Transfer
mix = 360./intP;
```

```
dP_mm = P_cvm.*mix + dP_m.*(1-mix);

%% Mass Transfer ( Mixing + 2-Volume)
% Mixture Calculation
rat = .30;     %Ratio of the argon volume mixed with Propellant
M_cvmt = (N_ar.*M_ar*rat+ N_p.*M_p)./(N_ar*rat + N_p);
Nmt = N_p + N_ar*rat;
R_cvfmt = R_u./M_cvmt;
Cp_cvmt = (m_ar.*Cp_ar*rat + m_p.*Cp_p)./(m_ar*rat + m_p);
Cv_cvmt = Cp_cvmt - R_cvfmt;
T_cvfmt = (m_p.*Cp_p.*T_af +
m_ar.*rat*Cv_ar.*T_cvi)./(m_ar.*Cv_cvmt.*rat+m_p.*(Cp_p*(1-rat) +
Cv_cvmt*rat));
% final Volume from after 2-Volume analysis

% Argon
m_a1mt = m_ar*(1-rat);
T_a1mt = T_cvi+ W./Cv_ar;
% T_a1mt = T_cvi*(m_ar.*Cv_ar-m_ar.*Cp_ar.*rat)./(m_a1mt.*Cv_ar);
P_a1mt = P_ci;
% V_a1mt = (V_cv-V_p1)/mag*(1-rat);
V_a1mt = (m_a1mt.*T_a1mt.*R_ar)./(P_a1mt)

% Propellant+ Argon mixture
V_p1mt = (V_cv-V_a1mt);
T_p1mt = T_cvfmt;
m_p1mt = m_p + m_ar*rat;
P_p1mt = m_p1mt.*R_cvfmt.*T_cvfmt./V_p1mt;

% Equilibrating pressure in the Piston system
mumt = 1*(m_p1mt.*R_cvfmt.*T_p1mt)./(m_a1mt.*R_ar.*T_a1mt);
dVmt = (V_a1mt.*mumt-V_p1mt)./(mumt+1);
P_p2mt = m_p1mt.*R_cvfmt.*T_p1mt./(V_p1mt+dVmt);
P_p2psimt = P_p2mt/6894.76;
dP_2vmt = (P_p2mt-P_ci)/6894.76;
dP_mmt = dP_2vmt./(m_p*1000);   %Model prediction of Pressure rise per
mass

%% Mass Transfer ( Mixing + 2-Volume + decrease in Taf
% Mixture Calculation
Tinc = T_af +200;
T_cvfmti = (m_p.*Cp_p.*Tinc +
m_ar.*rat*Cv_ar.*T_cvi)./(m_ar.*Cv_cvmt.*rat+m_p.*(Cp_p*(1-rat) +
Cv_cvmt*rat));
% P_cvfmt =
((m_ar*rat+m_p).*R_cvfmt.*T_cvfmt)./(V_pr*0.0254^3+V_cv*rat);
% final Volume from after 2-Volume analysis

% Argon
T_a1mti = T_cvi+ W./Cv_ar;
m_a1mti = m_ar*(1-rat);
P_a1mti = P_ci;
V_a1mti = T_a1mti;
```

```
% Propellant+ Argon mixture
V_p1mti = (V_cv-V_a1mti);
T_p1mti = T_cvfmti;
m_p1mti = m_p + m_ar*rat;
P_p1mti = m_p1mti.*R_cvfmt.*T_cvfmti./V_p1mti;

% Equilibrating pressure in the Piston system
mumti = 1*(m_p1mti.*R_cvfmt.*T_p1mti)./(m_a1mti.*R_ar.*T_a1mti);
dVmti = (V_a1mti.*mumti-V_p1mti)./(mumti+1);
P_p2mti = m_p1mti.*R_cvfmt.*T_p1mti./(V_p1mti+dVmti);
P_p2psimti = P_p2mti/6894.76;
dP_2vmti = (P_p2mti-P_ci)/6894.76;
dP_mmti = dP_2vmti./(m_p*1000);   %Model prediction of Pressure rise
per mass
%% Heat and Mass Transfer ( Mixing + 2-Volume)
dT_ar = 2;              %Temperature change based on experimental
values
T_a2 = T_a1+dT_ar;
Q = Cv_ar.*dT_ar;          %Heat transfer from Propellant gas to Ar
T_p2hm = T_p1mt-1*Q./Cv_cvmt;

muhm = 1*(m_p1mt.*R_cvfmt.*T_p2hm)./(m_a1mt.*R_ar.*T_a1mt);
dVhm = (V_a1mt.*muhm-V_p1mt)./(muhm+1);
P_p2hm = m_p1mt.*R_cvfmt.*T_p2hm./(V_p1mt+dVhm);
P_p2psihm = P_p2hm/6894.76;
dP_2vhm = (P_p2hm-P_ci)/6894.76;
dP_mhm = dP_2vhm./(m_p*1000); %Model prediction of Pressure rise per
mass w/HT

%With Mass normalization
[f1,agof1] = fit(intP',DP_m','power1');     %Data Fit
[f2,agof2] = fit(intP',P_cvm','power1');    %Mixture by Fraizer Fit
[f3,agof3] = fit(intP',dP_m','power1');     %2-Volume Fit
[f4,agof4] = fit(intP',dP_mh','power1');    %2-Volume Heat Transfer Fit
[f5,agof5] = fit(intP',dP_mmt','power1');   %2-Volume Mixture Fit
[f6,agofb] = fit(intP',dP_mmti','power1');  %2-Volume Mixture+Decrease1
b = sort(intP,'ascend');
figure(1)
loglog(intP,DP_m,'kp')

figure(1)
loglog(TestP,DP_m,'kp')
hold on
loglog(b,f1(b),'k',b,f2(b),'m',b,f3(b),'b',b,f4(b),'r',b,f6(b))
hold on
loglog(b,f5(b),'color',[0 0.5 0])
xlabel('Test Pressure (psi)')
xlim([500 2500])
ylabel('DeltaP per mass (psi/g)')
legend('Experimental Data','Data Fit','Mixture Model','2-Volume
Model','Model w/ Heat Transfer','Model w/ Mass Transfer','location',
'best')
x = b';     %Pressure Vector
```

```
y = f3(b);  %2-Volume Fit
z = f4(b);  %2-Volume HT Fit
z1 = f5(b); %2-Volume Mixture Fit

%% Post Decay
As = 0.15298573;     %Surface Area of strand burner
thick = 1.15/39.37;   %Thickness of burner
h = 14;              %Convection coefficient from Frazier
To = T_cvf-T_cvi;
m_sb = m_ar + m_p;
k_mix = .0163*(T_cvf./273).^(3/2)*(273-170)./(T_cvf+170);
k_s = 15.1;
Cp_s = 473;
rho_s = 7.7*10^3;
rho_mix = P_cf./((Cp_cv-Cv_cv).*T_cvf);
a_mix = k_mix./(rho_mix.*Cp_cv);
a_s  = k_s/(rho_s*Cp_s);

Tinterface = To.*(k_mix.*a_mix.^.5)./(k_s*a_mix.^.5+k_mix.*a_s^.5);
T_surf = T_cvi;
% Connduction
T_con = k_mix.*As./(thick*Cv_cv.*m_sb).*(T_surf - T_cvf) + T_cvf;
P_con = (m_sb.*R_cvf.*T_con)./(M_cv.*V_cv);

% Convection
NCv = N.*Cv_cv;
Tconv = (T_surf - T_cvf).*exp(-(h*As)\NCv) +  T_cvf;
dt = zeros(timestep,length(mass));

%% Time Stepping
for i = 1:timestep
    m_prop(i,:) = m_dot_r.*dt(i,:);
    m_cvt(i,:)= m_ar + m_prop(i,:);
    N_prop(i,:) = N_p.*dt(i)./t_b;
    N_cvt(i,:)= N_ar + N_prop(i,:);

    X_a(i,:) = N_ar./N_cvt(i,:);
    X_p(i,:) = 1 - X_a(i,:);
    Y_a(i,:) = m_ar./m_cvt(i,:);
    Y_b(i,:) = 1 - Y_a(i,:);

    M_CVt(i,:) = M_ar.*X_a(i,:) + M_p.*X_p(i,:);
    R_sys(i,:) = R_u./M_CVt(i,:);
    Cp_CVt(i,:) = Cp_ar.*X_a(i,:) + Cp_p.*X_p(i,:);
    Cv_CVt(i,:) = Cp_CVt(i,:) - R_sys(i,:);

    T_time(i,:) = (m_prop(i,:).*Cp_p.*T_af +
m_ar.*Cv_ar.*T_cvi)./(m_cvt(i,:).*Cv_CVt(i,:));
    P_time(i,:) = m_cvt(i,:).*R_sys(i,:).*T_time(i,:)./V_cv/6894.76;
    P_2vtime(i,:) = intP + (dP_mm/1.5).*((i-1)*delt./t_b);
    P_data(i,:) = intP+ (finP - intP).*((i-1)*delt./t_b);
    if i == 100
```

```
        break
    else
        dt(i+1,:) = delt+dt(i,:);
    end
end
figure(2)
for j = 1:length(mass)
    subplot (4,3,j)
%     figure(j+3)
    plot(dt(:,j),P_time(:,j),dt(:,j),P_data(:,j),dt(:,j),P_2vtime(:,j))
    xlabel('Time (s)')
    ylabel('Test Pressure (psi)')
end
  legend('Ideal Mixing Model','Experiments','2-Volume
Model','location', 'bestoutside')
  %% Compressability
Z = P_cvf*V_cv./((m_ar + m_p).*R_cvf.*T_cvf); % Mixture model with mix
temp
temp
Zf = P_cf*V_cv./((m_ar).*R_cvf.*T_cvf);
Zi = P_ci*V_cv./((m_ar).*R_cvf.*T_cvi);
Zv2 = P_ci*V_cv./((m_ar).*R_cvf.*(T_cvi+10));
Zv2R = P_ci*V_cv./((m_ar).*R_cvf.*T_cvi);
un = TestP*0 +1;
[Z1,agZ1] = fit(TestP',Z','cubicinterp');   %Mixture
[Z2,agZ2] = fit(TestP',Zf','poly2');   %Post Combustion Data
[Z3,agZ3] = fit(TestP',Zi','cubicinterp');   %Pre Combustion Data
[Z4,agZ4] = fit(TestP',Zv2','cubicinterp');   %2-Volume
[Z5,agZ5] = fit(TestP',Zv2R','cubicinterp');   %2-Volume

figure()
hold all
plot(TestP,un,'k',b,Z3(b),'-*')
xlabel('Test Pressure (psi)')
ylabel('Compressibility Factor')
title('Compressibility Factor Compared to Experiments')
legend('Ideal Gas','Pre-Combustion Data','best')
```

APPENDIX C-PRESSURE RISE DATA

The red color comes from the individual propellant strand, and the blue values are collected from the ProPEP simulation.

80% monomodal baseline 200 μm AP										
	NBT09-01	NBT09-02	NBT09-03	NBT09-04	NBT09-05	NBT09-06	NBT09-07	NBT09-08	NBT09-09	NBT09-10
m_p	0.71	0.69	0.67	0.67	0.69	0.71	0.68	0.71	0.67	0.69
L_p	1.041	1.000	0.979	1.001	0.979	1.059	0.965	1.013	0.964	1.004
r_b	0.25	0.30	0.36	0.80	0.42	0.41	0.47	0.35	0.35	0.29
Pi	515	757	989	1249	1488	1730	1981	1472	987	509
Pf	638	898	1146	1401	1691	1915	2197	1666	1137	635
MW	21.926	22.108	21.945	21.946	22.262	21.934	21.945	21.933	21.945	22.104
Gamma	1.2510	1.2487	1.2508	1.2507	1.2486	1.2509	1.2507	1.2509	1.2508	1.2488
N_p	3.24E-05	3.10E-05	3.05E-05	3.05E-05	3.09E-05	3.24E-05	3.10E-05	3.24E-05	3.05E-05	3.11E-05
Taf	2341	2381	2346	2347	2383	2345	2347	2344	2346	2379

	80% monomodal baseline 20 μm AP				
	FAO01-01	FAO01-02	FAO01-03	FAO01-04	FAO01-05
m_p	0.69	0.68	0.67	0.69	0.68
L_p	1.047	1.031	1.009	1.035	1.029
r_b	1.09	0.99	0.82	0.66	0.62
Pi	1993	1707	1216	897	569
Pf	2198	1904	1386	1053	711
MW	22.299	22.747	22.61	22.292	22.733
Gamma	1.2464	1.2411	1.2427	1.2466	1.2414
N_p	3.30E-05	3.10E-05	3.10E-05	3.30E-05	3.10E-05
Taf	2413	2506	2477	2410	2500

85%bimiodal modal baseline											
	NBT51-01	NBT51-02	NBT51-03	NBT51-04	NBT51-05	NBT51-06	NBT51-07	NBT51-08	NBT51-09	NBT51-10	NBT61-03
m_p	0.80	0.76	0.71	0.73	0.79	0.71	0.75	0.70	0.71	0.72	0.76
L_p	1.130	1.047	1.065	1.080	1.111	1.036	1.107	1.041	1.039	1.056	1.088
r_b	0.50	0.36	0.59	0.51	0.45	0.44	0.42	0.57	0.42	0.33	0.80
Pi	2063	1770	1527	1281	1050	763	513	1912	1613	610	4300
Pf	2322	2007	1747	1486	1257	933	671	2129	1825	766	4661
MW	24.545	22.379	22.425	24.504	22.723	22.419	24.665	22.427	22.425	22.541	24.895
Gamma	1.2225	1.2454	1.2449	1.2220	1.2414	1.2450	1.2230	1.2449	1.2449	1.2436	1.2191
N_p	3.30E-05	3.50E-05	3.30E-05	3.00E-05	3.60E-05	3.30E-05	3.00E-05	3.30E-05	3.30E-05	3.30E-05	3.10E-05
Taf	2848	2431	2440	2834	2502	2437	2844	2440	2440	2462	2915

	Aluminized baseline									
	ABT01-01	ABT01-02	ABT01-03	ABT01-04	ABT01-05	ABT02-01	ABT02-02	ABT02-03	ABT02-04	ABT02-05
m_p	0.71	0.71	0.77	0.74	0.72	0.74	0.76	0.75	0.74	0.71
L_p	1.033	1.037	1.132	1.084	1.048	1.082	1.115	1.085	1.076	1.035
r_b	0.24	0.29	0.33	0.36	0.37	0.37	0.39	0.31	0.26	0.33
Pi	582	841	1265	1622	2004	1840	1425	1046	683	1431
Pf	730	1022	1489	1852	2235	2078	1662	1253	848	1639
MW	23.905	24.119	23.978	24.397	24.021	24.409	23.886	23.756	24.303	23.993
Gamma	1.1914	1.1881	1.1901	1.1858	1.1897	1.1856	1.1906	1.1917	1.1871	1.1901
N_p	2.80E-05	2.80E-05	3.00E-05	2.80E-05	2.40E-05	2.80E-05	3.00E-05	2.90E-05	2.80E-05	2.80E-05
Taf	3090	3143	3123	3208	3141	3213	3113	3082	3167	3129

APPENDIX D-PRESSURE RISE MODEL COMPARISON

Linear burning rate data comparing the mixture model to the 2-volume model. Note the closer match of the 2-volume model to the collected data for 80% monomodal baseline.

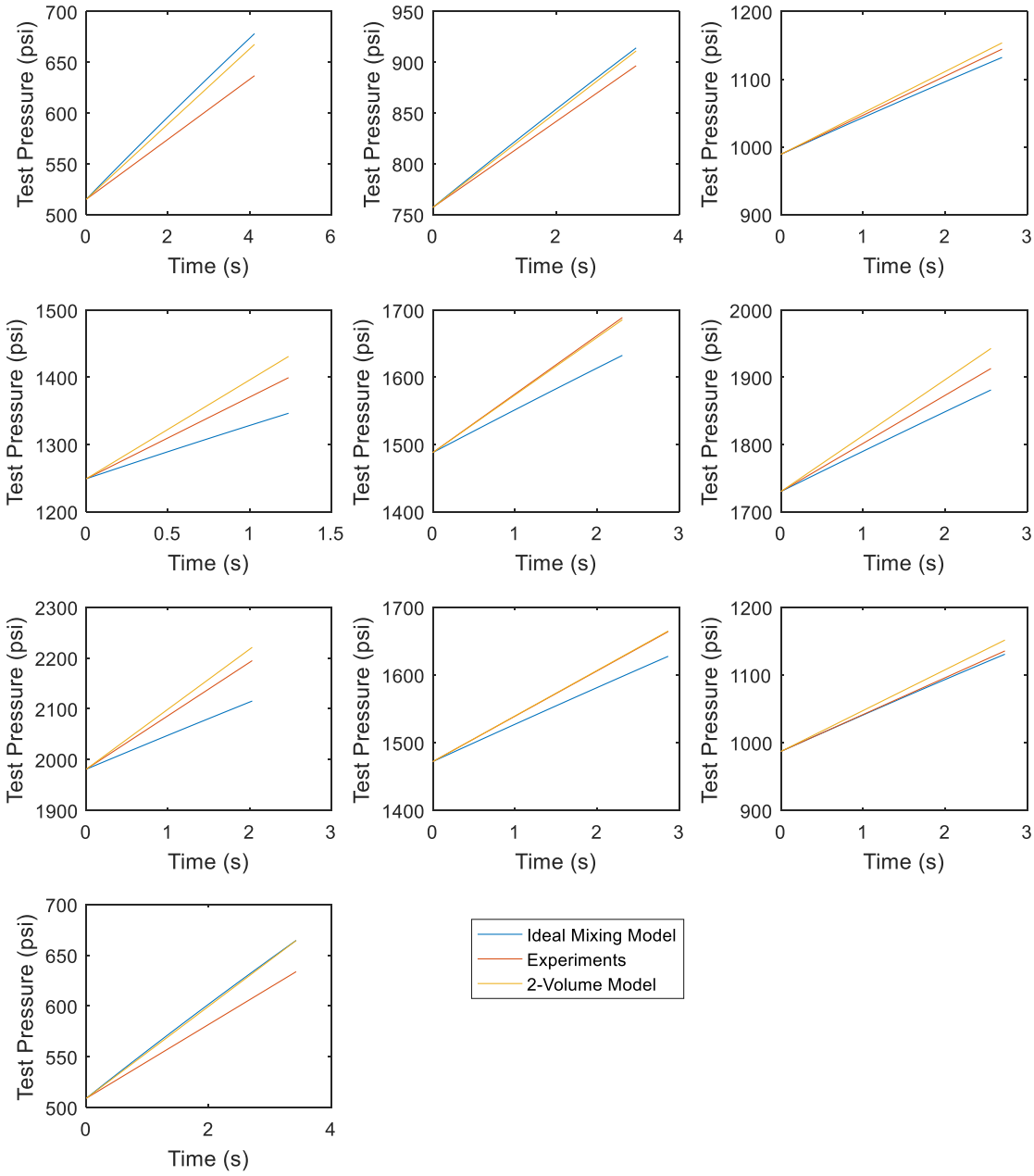

Linear burning rate data comparing the mixture model to the 2-volume model. Note the closer match of the 2-volume model to the collected data for 85% bimodal baseline.

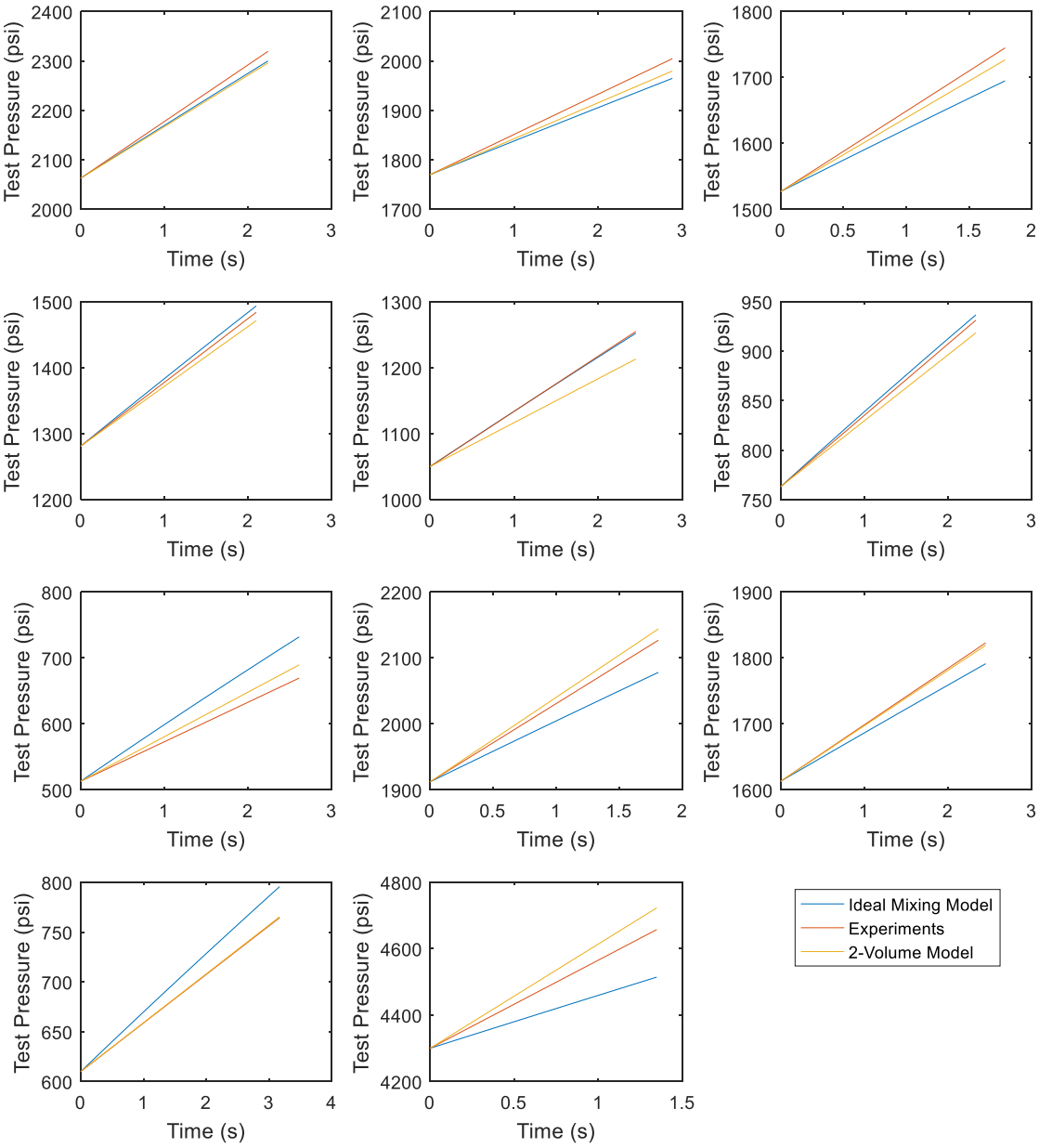

APPENDIX E- IGNITION DELAY TIME MODEL

```
function Main
% Ignition model for solid propellants using a variable power CO2 laser
% as the source for ignition. Propellant modeled as a cylinder with
% constant thermal properties dependent on temperature.
% By Andrew Demko derived from literature.

%Grid size
N = 40;

% Laser Constants
I_o     = 500000;                % W/m^2
abs_rad = 0.81;                  % 1/m
sigma   = 1;                     % Lazor Std Dev          || mm

% Geometric Dimensions
r_max = 0.1875*0.0254/2;           % m
% Pick thermal penetration depth to refine grid size.
% z_max = 0.125E-3;                 % m  (Non-Aluminized)
z_max = 1*0.125E-3;                 % m   (Aluminized)
% Initial Temperature
T_o = 22 + 273.15;               % K

% Ignition Search for how deep to define ignition temperature
z_loc = 0.025;                    % mm     Order of 10 micron
r_loc = 0.0;                     % mm
T_ign = 640;                     % K

%% Define Material Properties
%TiO2Properties
Kti = 4.80;    % Thermal conductivity   || W/m K
Cpti = 0.683;        % Specific heat          || J/g K

%Fe2O3 Properties
Kfe = 6.00;    % Thermal conductivity   || W/m K
Cpfe = 104.51/159.69;        % Specific heat          || J/g K

%AP properties
Kap = (9.95E-4 + T_o*3.75E-7);    % Thermal conductivity   ||
(cal/s)/cm K
Cpap = (0.16+T_o*0.41E-3);        % Specific heat          || cal/g K

%Al properties
Kal = (.651 + T_o*1.62E-4);    % Thermal conductivity   || (cal/s)/cm K
Cpal = (0.144+T_o*1.58E-4);        % Specific heat          || cal/g K

%HTPB properties
Khtpb = (4.4E-4 + T_o*1.3E-7);    % Thermal conductivity   ||
(cal/s)/cm K
Cphtpb = (0.25+T_o*0.85E-3);        % Specific heat          || cal/g K
```

```
% Cp > 523 = (0.19+T_o*0.62E-3)*4.184E6;

% non-aluminized
K = (Kap*.80 + Khtpb*.20)*418.4  % Thermal conductivity   || W/m K
Cp    = (Cpap*.80 + Cphtpb*.20)*4.184E6 % Specific heat        || J/kg
K
rho = 1630;                          % Density               || kg/m^3
alpha = K/(rho*Cp)                  % Thermal diffusivity    || m^2/s

 Kt = (Kap*.797 + Khtpb*.199)*418.4+ .004*Kti  % Thermal conductivity
|| W/m K
Cpt    = (Cpap*.80 + Cphtpb*.20)*4.184E6+ .004*Cpti % Specific heat
|| J/kg K
 Kf = (Kap*.797 + Khtpb*.199)*418.4+ .004*Kfe  % Thermal conductivity
|| W/m K
Cpf    = (Cpap*.80 + Cphtpb*.20)*4.184E6+ .004*Cpfe % Specific heat
|| J/kg K
% % % Aluminized
% K = (Kap*.67+Kal*.16 + Khtpb*.17)*418.4  % Thermal conductivity ||
W/m K
% Cp    = (Cpap*.67+Cpal*.16 + Cphtpb*.17)*4.184E6 % Specific hea ||
J/kg K
% rho   = 1670;                   % Density               || kg/m^3
% alpha = K/(rho*Cp)              % Thermal diffusivity    || m^2/s
Kt = (Kap*.668+Kal*.16 + Khtpb*.169)*418.4 + .003*Kti  % Thermal
conductivity || W/m K
Cpt    = (Cpap*.668+Cpal*.16 + Cphtpb*.169)*4.184E6+ .003*Cpti %
Specific hea || J/kg K
Kf = (Kap*.668+Kal*.16 + Khtpb*.169)*418.4 + .003*Kfe  % Thermal
conductivity || W/m K
Cpf    = (Cpap*.668+Cpal*.16 + Cphtpb*.169)*4.184E6+ .003*Cpfe %
Specific hea || J/kg K

% Code Begins
Nr = N+1;
Nz = N+21;
r = linspace(0,r_max,Nr);
z = linspace(0,z_max,Nz);
delta_r = mean(diff(r));
delta_z = mean(diff(z));
sigma = sigma*1E-3;

% 1000 in here because otherwise it blows up
qdot = I_o*abs_rad/sqrt(2*pi*sigma^2)*exp(-r.^2./(2*sigma^2));

A = spalloc(Nr,Nz,5*Nr*Nz);
b = zeros(Nr*Nz,1);
M = speye(Nr*Nz,Nr*Nz);
for i = 1:Nr
    for j = 1:Nz
        n = (j-1)*Nr + i;
        if r(i) == 0 || r(i) == r_max || z(j) == 0 || z(j) == z_max
```

```
            if r(i) == 0            % Left BC,   r = 0
                A(n,n)     = -1/delta_r;
                A(n,n+1)   =  1/delta_r;
            elseif r(i) == r_max    % Right BC,  r = r_max
                A(n,n-1)   = -1/delta_r;
                A(n,n)     =  1/delta_r;
            elseif z(j) == 0        % Top BC,    z = 0
                A(n,n)     = -1/delta_z;
                A(n,n+Nr)  =  1/delta_z;
                b(n,1)     = -qdot(i)/K;
%             elseif z(j) == z_max    % Bottom BC, z = z_max
% Standard BC's (adiabatic)
%                 A(n,n-Nr)  = -1/delta_z;
%                 A(n,n)     =  1/delta_z;
            elseif z(j) == z_max    % Bottom BC, z = z_max            %
For steady state (constant temp)
                A(n,n)     = 1;
                b(n,1)     = T_o;
            end
            M(n,n)         = 0;     % Set mass matrix to zero at BC's
        else
            A(n,n-1)  = alpha*(1/delta_r^2 - 1/(r(i)*2*delta_r));
            A(n,n)    = -2*alpha*(delta_r^-2 + delta_z^-2);
            A(n,n+1)  = alpha*(1/delta_r^2 + 1/(r(i)*2*delta_r));
            A(n,n-Nr) = alpha/delta_z^2;
            A(n,n+Nr) = alpha/delta_z^2;
        end
    end
end

% Standard
T0 = ones(Nr*Nz,1)*T_o;
tspan = [0 1000];
[value ind_z] = min(abs(z - z_loc/1000));        % Finds nearest value
to z_loc
[value ind_r] = min(abs(r - r_loc/1000));
n = (ind_z-1)*Nr + ind_r;
options = odeset('Mass',M,'Events',@(t,T) EventFcn(t,T,n,T_ign));
[t,T] = ode15s(@(t,T) A*T-b,tspan,T0,options);

PlotFigs(t,r,z,qdot,T,0)
PlotFigs(t,r,z,qdot,T,1)

z = z*1000000;
for k = 1:length(t)
    for i = 1:length(r)
        for j = 1:length(z)
            n = (j-1)*length(r)+i;
            T_2dt(i,j,k) = T(k,n);
        end
    end
    figure(3)
    subplot(5,1,1)
```

```
plot(r,qdot)
set(gca,'XTickLabel','')
set(gca,'YTickLabel','')
xlim([0 r(end)])
ylabel('q_dot')

subplot(5,1,2:5)
switch nargin
    case 6
        T_plot = Convert_to_2d(r,z,T(end,:));
    case 7
        T_plot = Convert_to_2d(r,z,T_ss' - T(end,:)); % difference
between SS and final transient
end
surf(r,z,T_2dt(:,:,k)','LineStyle','none')
xlim([0 r(end)])
ylim([0 z(end)])
xlabel('r (mm)')
ylabel('z (\mu m)')
set(gca,'XAxisLocation','top')
set(gca,'XTickMode','auto')
zlabel('T')
view(0,-90)
colorbar('southoutside')
caxis([295 800])
% F(k) = getframe(gcf)
end
 figure(4)
 subplot(5,1,1)
plot(r,qdot)
set(gca,'XTickLabel','')
set(gca,'YTickLabel','')
xlim([0 r(end)])
ylabel('q_dot')

subplot(5,1,2:5)
switch nargin
    case 6
        T_plot = Convert_to_2d(r,z,T(end,:));
    case 7
        T_plot = Convert_to_2d(r,z,T_ss' - T(end,:)); % difference
between SS and final transient
end
surf(r,z,T_2dt(:,:,33)','LineStyle','none')   %Non-aluminized
% surf(r,z,T_2dt(:,:,48)','LineStyle','none')     %Aluminized
xlim([0 r(end)])
ylim([0 z(end)])
xlabel('r (mm)')
ylabel('z (\mu m)')
set(gca,'XAxisLocation','top')
set(gca,'XTickMode','auto')
zlabel('T')
view(0,-90)
```

```
colorbar('southoutside')
caxis([295 800])
assignin('base', 'T_2dt', T_2dt);

function [value,isterminal,direction] = EventFcn(t,T,n,T_ign)
% mean(T
value      = T(n) - T_ign; % The value that we want to be zero
isterminal = 1;          % Halt integration
direction  = 0;          % The zero can be approached from either
direction

function T_2d = Convert_to_2d(r,z,T)
for i = 1:length(r)
    for j = 1:length(z)
        n = (j-1)*length(r)+i;
        T_2d(i,j) = T(end,n);
    end
end

function PlotFigs(t,r,z,qdot,T,interp_choice,T_ss)
% Plot
% Convert from m
r = r*1000;
z = z*1000;

figure
subplot(5,1,1)
plot(r,qdot)
set(gca,'XTickLabel','')
set(gca,'YTickLabel','')
xlim([0 r(end)])
ylabel('q_dot')

subplot(5,1,2:5)
switch nargin
    case 6
        T_plot = Convert_to_2d(r,z,T(end,:));
    case 7
        T_plot = Convert_to_2d(r,z,T_ss' - T(end,:)); % difference
between SS and final transient
end
if interp_choice == 0
    surf(r,z,T_plot','LineStyle','none')
elseif interp_choice == 1
    surf(r,z,T_plot','LineStyle','none','FaceColor','interp')
end
xlim([0 r(end)])
ylim([0 z(end)])
xlabel('r (mm)')
ylabel('z (mm)')
set(gca,'XAxisLocation','top')
set(gca,'XTickMode','auto')
```

```
zlabel('T')
view(0,-90)
colorbar('southoutside')
if nargin == 6
    caxis([295 800])
end
% Save variables to workspace
assignin('base', 't', t);
assignin('base', 'r', r);
assignin('base', 'z', z);
assignin('base', 'T', T);
assignin('base', 'T_plot', T_plot);
```

APPENDIX F- ENERGY CORRECTION FOR SHUTTER CODE

```
%Program to calculate the power correction value for the opening and
closing
%of the mechanical shutter.

to = 29/1000;      % Opening time in ms
tc = 41/1000;      % Closing time in ms
r = 0.1875*.0254; % Radius of sample convert inches to m
Eo = 60;           % Power supplied (W)
Ar = pi*r^2        % Area of propellant surface

%Opening Velocity
h = 2*r/to;
%Variable area function
fun = @(t) r^2*acos((r-h*t)./r)-(r-h*t).*(2*r*h*t-(h*t).^2).^.5;
aro = integral(fun,0,to)
rat_o = aro/Ar

%Closing Velocity
h = 2*r/tc;

%Variable area function
fun = @(t) r^2*acos((r-h*t)./r)-(r-h*t).*(2*r*h*t-(h*t).^2).^.5;
arc = integral(fun,0,tc)
rat_c = arc/Ar

%Energy lost to the shutter opening and closing times
Elost = Eo*(rat_o*to + rat_c*tc)    % (J)
```